The effect of Kondo correlations on the absorption spectrum of semiconductor quantum dots

by

Rolf W. Helmes

Diploma Thesis

Technische Universität München

May 2004

For my parents, for their love, trust and support during all these years.
-
Für meine Eltern, für ihre Liebe, ihr Vertrauen und ihre Unterstützung in den letzten Jahren.

Abstract

In recent experiments, it has been shown that it is feasible to measure the absorption and emission spectrum of a single InAs quantum dot (QD) embedded in a GaAs semiconductor. In absorption measurements, excitons are generated inside the QD, whereas the emission spectrum originates from the recombination of excitons inside the QD. The emission spectrum measurements reveal that the QD has an atom-like electronic level structure. Motivated by these experiments, we study an extended Anderson model, which describes a local conduction band level coupled to a lead, but also takes account of a local valence band level. We study the extented model both qualitatively, using Anderson's Poor Man Scaling method, and quantitatively, using Wilson's Numerical Renormalization Group (NRG). The latter is used to calculate the zero-temperature absorption spectrum of a QD that is initially in the strongly correlated Kondo ground state.

In the unphysical limiting case of a vanishing exciton binding energy, $U_{\mathrm{exc}} = 0$, the absorption spectrum is determined by the local density of states of the QD. We use this well-understood limiting case as a consistency check for our numerical calculations of the absorption spectrum. For finite values of U_{exc}, we predict two rather dramatic new features. Firstly, the threshold energy below which no photons are absorbed, say ω_0, shows a marked, non-monotonic shift as a function of U_{exc}; a qualitative explanation of this behavior can be given by considering the energy scales. Secondly, as U_{exc} is increased, the absorption spectrum shows a tremendous increase in peak height. In fact, the absorption spectrum diverges at the threshold energy ω_0, in close analogy to the well-known X-ray edge absorption spectrum. Exploiting analogies to the latter, we propose and numerically verify an analytical expression for the exponent that governs this divergence, in terms of the absorption-induced change in the average occupation of the local conduction band level.

Contents

Chapter 1

Introduction

In the 1930s measurements of the electrical resistance of certain metals revealed an effect that went on to puzzle physicists for three decades: as the temperature is lowered, the resistance reaches a minimum. Rather than decreasing or saturating, the resistance increases as the temperature is lowered further, see Fig. 1.1. Later it was found that the effect only occurs if the metal contains magnetic impurities, such as cobalt atoms.

The first explanation of this phenomenon was given by J. Kondo in 1964, see [2], whereupon the effect was named after him: the 'Kondo effect'. Kondo's explanation is based on a model where the local moment of the magnetic impurities with spin S is coupled via an exchange interaction with a coupling constant J to the spin of the conduction band electrons of the metal. Kondo's calculations show that a $\ln(T_K/T)$ contribution to the resistance emerges in third order perturbation theory in the coupling J, where T_K is a constant called 'Kondo temperature'. If the temperature decreases below T_K, this term becomes large and finally dominates the other contributions to the resistance, as e. g. phonon scattering, thus explaining the phenomenon of increasing resistance. However, as the $\ln(T_K/T)$ term diverges as $T \to 0$, it is clear that Kondo's calculation can not be valid at low temperatures and that a more comprehensive theory is needed to explain the low temperature behaviour. This problem of finding a solution valid in the low temperature regime $T \to 0$ is known as the 'Kondo problem'.

One of the first questions to explore in looking for a more satisfactory theory in the low temperature regime is whether the divergence arising from the logarithmic term can be removed by summing the higher order terms in the perturbation expansion. Approaches in this direction were made by Abrikosov, see [2], and several others, but they encountered severe difficulties, which could not be solved satisfactorily. 1970 P. W. Anderson attacked the problem with a scaling method which he termed 'Poor Man's Scaling' [3]. This approach leads to a qualitative understanding of systems undergoing the Kondo effect and will be explained in Chapter 4. In 1974 and 1975 K. G. Wilson developed a theory producing quantative results, the 'numerical renormalization group' method, called NRG [4]. It is based on scaling and renormalization group ideas. NRG is the central method of this thesis and will be introduced in Chapter 5.

The Kondo effect has experienced a revival in the 1990s when it became possible to

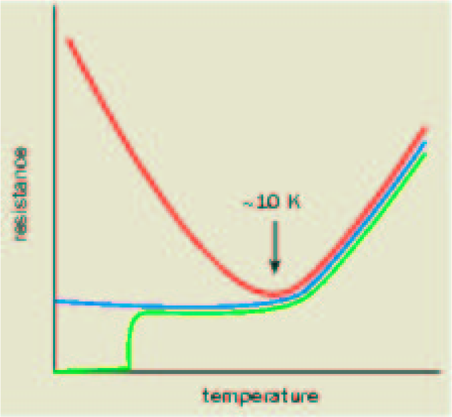

Figure 1.1: Three different behaviours of metals as the temperature is lowered. Some metals become super conducting at a critical temperature (green). For most metals, the resistance decreases until it saturates at some residual value (blue). If the metal contains a small fraction of magnetic impurities, for instance cobalt in copper, the resistance increases at low temperature due to the Kondo effect (red). Picture taken from [1]

fabricate quantum dots with atom-like electronic structures, opening new possibilities to study the Kondo effect experimentally, see [5]. Using these artificial atoms as magnetic impurities, today it is possible to control important parameters in experiments. E.g., the number and energy of electrons within the dot can be controlled by applying gate voltages or the Coulomb repulsion energy of the electrons can be varied by changing the size of the dot.

So far, most evidence about the Kondo effect was gained by indirect observation like current-voltage or magnetic susceptibility measurements. The idea behind this thesis is to investigate if there is any signature of the Kondo effect in optical absorption measurements conducted with quantum dots in a semi-conductor. In particular, we will study the light induced excitation of excitons in a quantum dot. The initial state of the quantum dot is supposed to be the 'Kondo ground-state', a many-body state involving strong correlations between the electrons in the dot and the electrons in the conduction band. By light absorption, an exciton can be excited inside the dot, thereby destroying the Kondo-state. The central aim of this thesis is to calculate the absorption spectrum of a quantum dot in the Kondo ground-state.

In Chapter 2 the experimental background, optical experiments with quantum dots [6], will be introduced. In these experiments, excitons, i. e. electron-hole pairs, are trapped in quantum dots, together with an experimentally controlled number of additional electrons. After a certain time the hole recombines with an electron, whereby a photon is emitted. Recently experimentalists have succeeded in measuring the photoluminescence of a single quantum dot. These measurements can be compared with atomic spectroscopy measurements. It turns out, that as in atomic spectroscopy the quantum dot emits characteristic light depending on the number of additional electrons trapped with the exciton, which reveals a atom-like shell structure of the electronic energy levels of the dot. So far no experiments were conducted in the Kondo regime, but in principle they are feasible. If such experiments are made, it will be exciting if the results agree with the predictions made in this thesis.

In Chapter 3 the model describing the quantum dot in a semiconductor will be put up. It will be an extension of the Anderson Model, a model put forward by P. W. Anderson in 1961 [7], which describes physical systems where a local level interacts with lead electrons, e. g. a magnetic impurity embedded in a metal. The Anderson Model can be reduced to the Kondo model in the appropriate parameter regime by the Schrieffer-Wolf transformation. Thus the physics of the Kondo effect can be described by the Anderson Model. Furthermore, in the last section of the chapter, alternative theoretical approaches to solve the model will be treated.

In Chapter 4, Anderson's Poor Man Scaling approach will be explained and applied to the extended Anderson Model.

In Chapter 5, Wilson's NRG method will be introduced. In the second section of the chapter, it will be shown how the method has been modified to solve the Hamiltonian corresponding to the physical system studied in this thesis.

The results will be presented and discussed in Chapter 6 and finally, in Chapter 7, there will be a conclusion.

Chapter 2

Experimental Background

Photoluminescence measurements on semiconductor quantum dots, conducted by Karrai et al., [6], are the experimental background of this thesis. The set-up consists primarily of a GaAs substrate, which contains InAs quantum dots. In the experiment, excitons are produced in the GaAs by laser excitation. The excitons migrate in the GaAs and finally become trapped in the InAs quantum dots. Finally the excitons recombine, whereby a photon is emitted. This photoluminescence is measured. The emitted photons have a certain wavelength, characteristic for the level structure of the InAs quantum dots. The experiment is described in this chapter.

2.1 Experimental set-up

The set-up of the experiment is shown in Fig. 2.1a. A substrate made of the semi-conductor GaAs is covered with one and a half mono-layers of InAs, likewise a semi-conductor. Due to the different lattice constants of GaAs and InAs, the InAs starts to migrate and there is a strain-driven growth of rings. Thus the experiment strictly speaking deals with quantum rings and not dots, but since the word ‘quantum dot’ is commonly used for a nano sized object small enough to make quantum mechanical characteristics detectable and since for present purposes rings and dots behave very similarly, I will use the words dot and ring as synonyms. The quantum dots are covered with GaAs. They are separated by tunnel barriers from a back contact on the one side and a gate contact on the other side. Due to the barriers, no current will flow if a potential is applied between the contacts.

A band diagram for two different gate voltages ${V_g}^a$ and ${V_g}^b$ applied between the gate and the back contact is shown in Fig. 2.1b. The energy of the lowest point of the conduction band is plotted along the y-axis. Space is plotted along the x-axis, note that Fig. 2.1b is aligned with Fig. 2.1a. Since the bandgap of InAs is smaller than the bandgap of GaAs, the bottom of the InAs conduction band lies below the bottom of the GaAs conduction band. Thus there is a dip at the location of the InAs quantum dots which leads to the formation of local levels inside the quantum dots that lie below the GaAs conduction band. Therefore electrons can be captured in the dots. By varying the applied voltage, the local

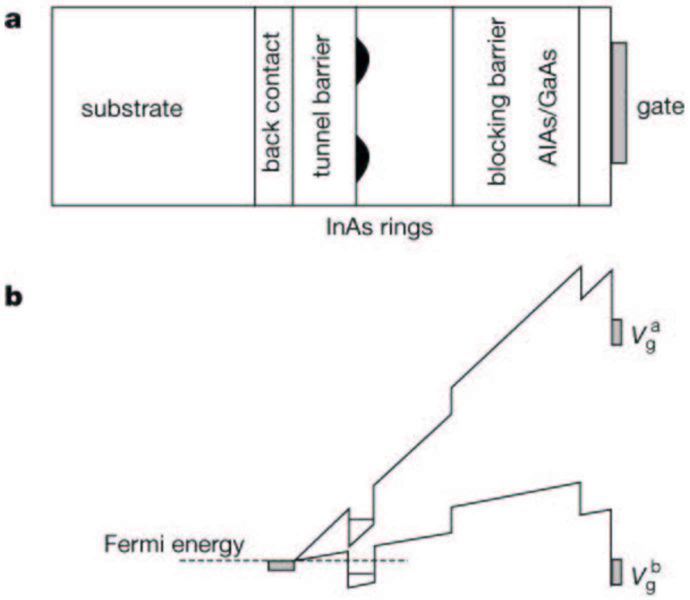

Figure 2.1: a) Layer structure of experimental set-up. b) Band diagram at two different gate voltages ${V_g}^a$ and ${V_g}^b$, where the energy of the lowest point of the conduction band is plotted along the y-axis and the position is plotted along the x-axis. Note that b) is aligned with a). Picture from [6].

levels of the dots can be shifted with respect to the Fermi energy of the back contact, as shown in Fig. 2.1b. Therefore, by regulating the voltage, the number of electrons in the dot can be set to a desired number, thus the name 'charge-tunable quantum dots'. Due to the Coulomb repulsion of the electrons on the dot, there is a Coulomb blockade which impedes other electrons to tunnel into the dots. As the dots are very small, the Coulomb blockade of the considered InAs dots is high, typically about 20 meV $\approx k_B$ 230 K, see [8], thus the charge on the dot changes in discrete units of e as one electron after the other enters. The situation in the valence band is analogous to the conduction band. This time the top of the InAs valence band lies above the top of the GaAs band, building a trap for holes.

The quantum dots form a two-dimensional structure, as they are about 6 nm thick yet approximately 20 nm in diameter, see [8]. This results in vertical confinement energies almost an order of magnitude larger than the lateral confinement energies, thus excitations in the vertical dimension can be neglected. The dots feature radial symmetry, which leads to an atom-like energy level structure for electrons trapped in the dot [6], shown in Fig. 2.2. Just like the Hydrogen atom, the dot possesses one s-level, but it has only two p-levels, since it is two-dimensional. There are three d-levels, but they will not be considered in the following. For understanding the underlying principles of the experiment it is enough to consider just the s- and the p-levels, the d-levels do not yield any new physics. There is also a level structure for holes, but we will consider at most one hole trapped in a dot, see

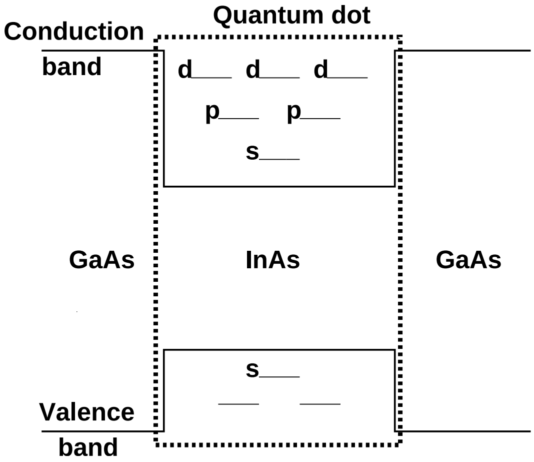

Figure 2.2: Diagram of atom-like level structure of quantum dots due to radial symmetry. Explanations see text.

below, so just the highest lying level, the s-level, is important here.

2.2 Photoluminescence measurements

The goal of the experiment is to measure the photoluminescence of exciton recombination inside the quantum dots. In the experiment, excitons are produced inside the GaAs by laser excitation with frequency resonant to the GaAs bandgap. The excitons migrate and finally become trapped in the InAs dots. The number of excited excitons is proportional to the intensity of the laser excitation which is always kept small enough to justify the assumption that there is at most one exciton trapped in one dot. After a certain time, the trapped excitons will recombine, thereby emitting photons which are detected. The atom-like level structure of the dots described in the previous section will be visible in the absorption spectrum. In fact, we will be able to explain the experimental results very well by describing the states before and after recombination in terms of occupation of the s- and the p-levels.

The shape of the emission spectrum depends on the applied gate voltage V_g. Before the recombination of the exciton, there is at least one electron in the dot, belonging to the electron-hole pair constituting the exciton. Depending on V_g, there can be additional electrons in the dot. We distinguish between X^0, X^{1-}, X^{2-}, etc., excitons, where the superscript denotes the total charge, i. e. the figure in the superscript denotes the number of additional electrons. E. g., X^{2-} identifies the state where one hole and three electrons are captured in the dot. Due to selection rules, the hole recombines always with an electron in the s-level. Still the energy of the emitted photon depends on the number of electrons in the dot because of Coulomb interactions between the electrons. Before interpreting the experimental results, however, it is helpful to take a closer look at the time scales involved.

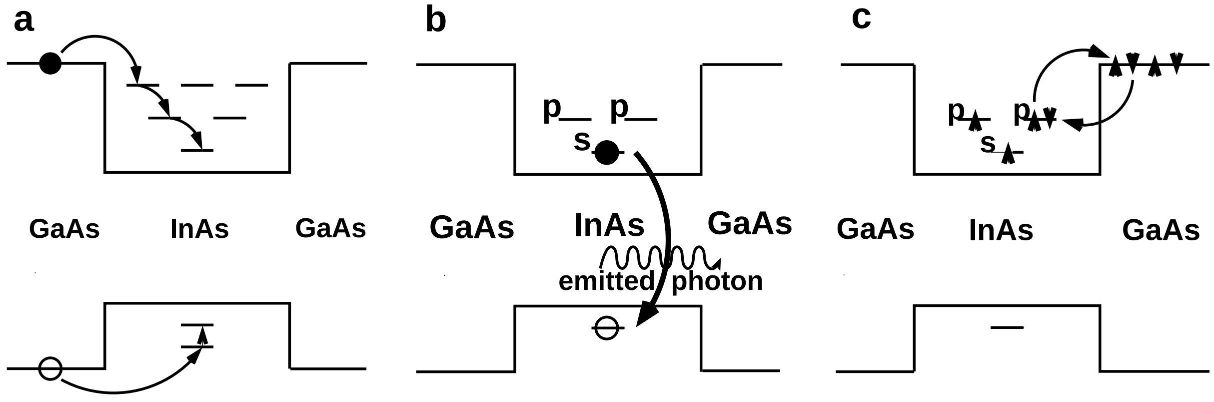

Figure 2.3: Crucial processes of the exciton recombination. a) The figure shows an excitons, which consists of an electron (filled circle) and a hole (empty circle). The excitons are created by laser excitation inside the GaAs, where they wander around and finally become trapped inside the InAs quantum dots. After the electron-hole pair is trapped, the electron and the hole relax into the lowest lying states. b) In the recombination process, an electron recombines with a hole, whereby a photon is emitted. c) The figure shows a spin-flip process, where an electron hops from the dot into the conduction band and is replaced by an electron with anti-parallel spin which tunnels from the conduction band into the hole.

The crucial processes of the exciton recombination are depicted in Fig. 2.3. After an exciton migrating in the GaAs becomes trapped in an InAs dot, the electron and the hole interact with phonon modes and relax to the lowest lying levels, Fig. 2.3a. The time scale of the relaxation process is about $\tau_{\text{relax}} \sim 1\text{ps}$. This is three orders of magnitude smaller than the typical lifetime of an exciton trapped in the dot, the time scale of the exciton recombination, Fig. 2.3b, which is approximately $\tau_{\text{recomb}} \sim 1\text{ns}$. Finally there is the possibility of a spin-flip process, where an electron hops from the dot into the lead and is replaced by another electron in the lead with opposite spin. Thus altogether the spin of the dot electron is flipped, Fig. 2.3c, which takes about $\tau_{\text{spinflip}} \sim 1\text{ns}$ or longer. For details about the time scales see [9], [10], [11], [12] and [13]. As the relaxation process is the fastest process involved, it can be assumed that an exciton is in the lowest possible state before recombining.

The experimental results of the optical emission measurements are shown in Fig. 2.4. They are collected from measurements on one single quantum dot. This can be assured in the following way. As mentioned in the previous section, the InAs quantum dots are self-organized, they are formed by strain-driven growth. This gives rise to the fact that the quantum dots are not all exactly alike, but there are minor differences in size and form. Therefore, each quantum dot emits characteristic light. In the experiment, a quantum dot was chosen whose emitted spectrum was unusual and a little aside the broad spectrum caused by the majority of dots. Of course, the spectrum of the single dot is still considered to be representative of that of a 'typical' dot.

The four emission spectra in Fig. 2.4 correspond to four different gate voltages. The spectrum at the bottom was recorded with the gate voltage tuned such that X^0 excitons were trapped in the dots. In the spectrum above the recombination of X^{-1} excitons was measured. The initial and the final state of the recombination process are shown on the right hand side. Before recombination, two electrons and one hole are trapped in the dot. After recombination, there are two different final states, the s-level is occupied by either one spin-up or one spin-down electron. As no magnetic field was applied during the experiment, these two final states are degenerate and just one of them is illustrated. The difference in energy between the X and the X^{-1} emission peak is caused by the exchange energy of the two electrons in the double occupied s-level of the X^{-1} exciton. The recombination of the X^{-2} excitons results in two peaks, as shown in the second spectrum from top. The two different peaks originate from two different final states illustrated on the right hand side. Again, final states with different spin configurations that are degenerate to the states in the picture are not illustrated. The two final states in the picture have different energies as the exchange energy is different for parallel and anti-parallel spins. Furthermore, they have a different lifetime, because the right final state can decay into a double occupied s-level by spin relaxation. This is not possible for the left state, here a spin-flip is needed before relaxation. As mentioned above, the time scale for spin-flips is about three orders of magnitude larger than the time-scale for relaxation. Hence, the lifetime of the left final state is much longer. If one applies the Heisenberg uncertainty principle $\Delta E \cdot \Delta t \sim \hbar$, one sees that its energy is defined much sharper, resulting in a narrow peak. In contrast to the left final state or the final states of the X and X^{-1} recombination, the right final state has a comparably short lifetime, giving rise to the broad peak shown in the spectrum. The same argument applies to the case of the X^{-3} recombination. The peaks on the right hand side in the X^{-2} and X^{-3} recombination spectra stem from a second dot and can be disregarded.

These experimental results confirm the assumption of an atom-like level structure of the quantum dots. With the knowledge that the used level-structure describes the quantum dots in a appropriate way and that the number of captured electrons can be controlled in experiment, a theoretical model together with its Hamiltonian can be proposed. In the next chapter this Model-Hamiltonian will be introduced by suitably generalizing the Anderson Model.

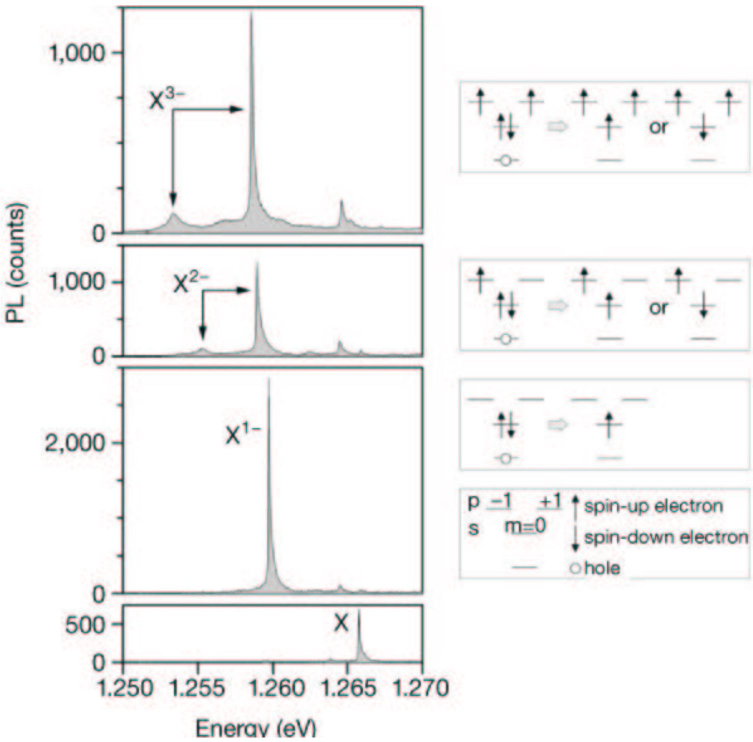

Figure 2.4: Photoluminescence from a single quantum dot for excitons with different charge. The number of counts is plotted versus the energy of the detected photons. Spectra are shown at gate voltages $V_g = -0.76, -0.16, -0.10$ and $0.40V$, corresponding to emission from the X, X^{1-}, X^{2-} and X^{3-} excitons, respectively. On the right hand side the initial states and the final states of the recombination processes are illustrated. In the emission process of the X^{2-} and X^{3-} there are two different kinds of final states. In contrast to the left final states, no spin-flip process is needed for the right final states in order for the dot to relax to the ground state. Therefore the lifetime of the right final states is shorter, leading to a broader emission peak. Picture from [6].

Chapter 3

Model

In the first section of this chapter the Anderson model will be introduced. It will be shown that in a certain parameter regime it can be reduced to the Kondo model by the Schrieffer-Wolff tranformation. Furthermore a short introduction to the Kondo effect will be given.

In the second section a model will be proposed that describes the system of an InAs quantum dot embedded in GaAs which was introduced in Chapter 2. This model will be an extension of the Anderson model.

With the help of the model we will be able to attack the main subject studied in this thesis, the absorption of light by the InAs quantum dots. This is the time inverse process of emission studied in the experiment which was presented in Chapter 2. In the absorption process, a photon is absorbed in the InAs dot, whereby an exciton is created. Before absorption, the state of the quantum dot is assumed to be the Kondo-state, a many-body state involving strong correlations between the electrons in the dot and the electrons in the conduction band. The Kondo-state will be introduced in Section 3.1. The light absorption excites an exciton in the dot which destroys the Kondo-state. The central prediction of this thesis is that this transition from a Kondo- to a non-Kondo-state causes a distinct feature in the absorption spectrum.

An ansatz for the calculation of the absorption spectra using Fermi's Golden Rule will be put forward in Section 3.3. The section will be concluded with a limiting case of the absorption spectra which can be calculated by a short analytical calculation.

In the last section, I will shortly present other theoretical approaches to the issue.

3.1 Anderson model and Kondo effect

In this section the Anderson model will be introduced and a short introduction to the Kondo effect will be given. The notation used in this section is unconventional, but it will prove to be useful in the next section, where the Anderson model is extended to describe the physical system studied in this thesis. The Anderson model describes physical systems where a local level of an impurity is coupled to a band of conduction electrons, see [2]. It

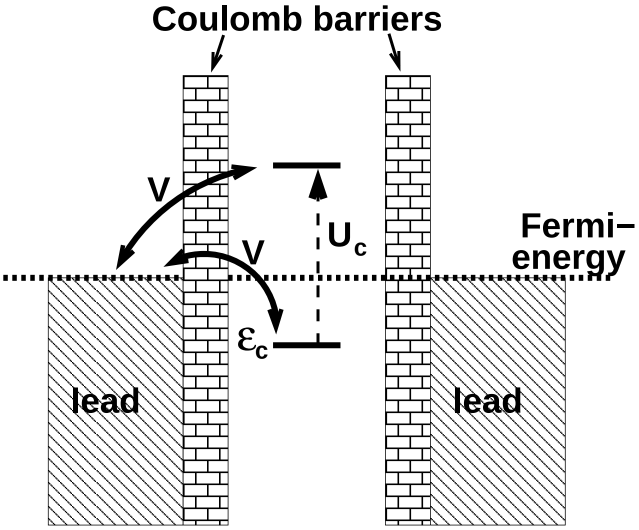

Figure 3.1: System described by Anderson model: local level coupled to lead. Explanations see text.

is given by

$$\mathcal{H}_{\text{Anderson}} \equiv \mathcal{H}_{\text{dot}} + \mathcal{H}_{\text{lead}} + \mathcal{H}_{\text{coupling}}, \tag{3.1}$$

with

$$\mathcal{H}_{\text{dot}} = \sum_{\sigma=\uparrow,\downarrow} \epsilon_c c^\dagger_\sigma c_\sigma + U_c \hat{n}_{c,\uparrow}\hat{n}_{c,\downarrow} \tag{3.2a}$$

$$\mathcal{H}_{\text{lead}} = \sum_{\vec{k},\sigma} \epsilon_{\vec{k}} l^\dagger_{\vec{k}\sigma} l_{\vec{k}\sigma} \tag{3.2b}$$

$$\mathcal{H}_{\text{coupling}} = \sum_{\vec{k},\sigma} \left(V_{\vec{k}c} l^\dagger_{\vec{k}\sigma} c_\sigma + V^*_{\vec{k}c} c^\dagger_\sigma l_{\vec{k}\sigma} \right), \tag{3.2c}$$

see Fig. 3.1. The physics of the local level is contained in $\mathcal{H}_{\text{dot}}$, where ϵ_c is the energy of the level, to be measured from the Fermi level, and $c^\dagger_\sigma (c_\sigma)$ creates (annihilates) an electron in the level with spin σ. The subscript 'c' stands for 'conduction band', in the next section, we will also need an index 'v' for 'valence band'. If the level is doubly occupied, there is a Coulomb repulsion of the two electrons, described by $U_c \hat{n}_{c,\uparrow}\hat{n}_{c,\downarrow}$, where $\hat{n}_{c,\sigma} = c^\dagger_\sigma c_\sigma$ is the number operator and U_c is the energy cost for the double occupancy.

The local level is coupled to a lead, which is described by quasi-particles in the Anderson model. The Hamiltonian of the lead is $\mathcal{H}_{\text{lead}}$, where $l^\dagger_{\vec{k}\sigma}(l_{\vec{k}\sigma})$ is the creation (annihilation) operator of a particle with wavevector $\vec{k}$, spin σ and energy $\epsilon_{\vec{k}}$, again to be measured from the Fermi level. Here 'l' stands for 'lead'.

The part $\mathcal{H}_{\text{coupling}}$ of the Anderson Hamiltonian couples the local level to the lead. The strength of the coupling is given by the hybridization matrix element $V_{\vec{k}c} = \langle \phi_{dot}(\vec{r}) | \mathcal{H}_{\text{Anderson}} | \psi_{\vec{k}} \rangle$, where $\phi_{dot}(\vec{r})$ is the wavefunction describing the dot and $\psi_{\vec{k}}$ is the wavefunction of a lead electron with wavevector $\vec{k}$. It is common to neglect all $\vec{k}$-dependence of these matrix elements, and to use $V_{\vec{k}c} = V_c$.

Due to the coupling, the local level is broadened, it has a level width $\Gamma \propto |V|^2$. The average occupation $n_{c,\sigma} = \langle \hat{n}_{c,\sigma} \rangle$ of the dot depends on U_c, Γ and the position of ϵ_c with respect to the Fermi energy, which will be set to zero in the following. Roughly speaking the occupation will be two for $\epsilon_c + U_c < -\Gamma$, around one for $\epsilon_c < -\Gamma, \epsilon_c + U_c > \Gamma$, or zero for $\epsilon_c > \Gamma$.

With the help of NRG, it is possible to solve the Anderson Hamiltonian numerically, see Chapter 5. Yet it might be helpful to know, for a reader unfamiliar with the subject, how the Anderson model is connected to the Kondo model and the Kondo effect. The Kondo model was put forward by Kondo in 1964; it is treated in [2] under the name 's-d model'. It was the first explanation of an effect named after Kondo, the Kondo effect. Many interesting experimental manifestations of the Kondo effect are described in [2] and [1]. Like the Anderson model, the Kondo model describes the interaction between a impurity and a lead. In contrast to the Anderson model, the impurity in the Kondo model consists just of a local moment with spin S and thus only the spin-spin exchange interaction between the impurity and the lead are considered. The Anderson model and the Kondo model are related by the Schrieffer-Wolff transformation, see section 1.7 of [2] for details.

The argument below is only intuitive. It is intended to visualize the physics behind the Kondo effect. For a rigorous discussion see [2]. Considering the Anderson model, let us study the following situation. If $\epsilon_c < 0 < \epsilon_c + U_c$ and if the temperature T is sufficiently low for neglecting thermal excitations, $k_B T << |\epsilon_c|, \epsilon_c + U_c$, the local level will be single occupied. Yet the spin of the electron can be flipped by two different virtual processes described by second order perturbation theory in the coupling between dot and lead. In the first process, see Fig. 3.2a, the electron tunnels from the local level to the lead where due to the low temperature only states near the Fermi surface are available. Thereby energy conservation is violated, which is allowable for a time $\Delta t \sim \hbar/|\epsilon_c|$ given by the Heisenberg uncertainty principle. On this time scale an electron must tunnel back from the lead to the local level. If this second electron has the opposite spin direction of the first, the spin of the electron on the local level will be effectively flipped. Applying the same argument, it is possible for the time $\Delta t \sim \hbar/(\epsilon_c + U_c)$ to doubly occupy the local level which is the second virtual process, see Fig. 3.2b. If the electron which was originally on the level tunnels out and the electron with anti-parallel spin is left on the local level, the spin of the localized electron is flipped. We have argued that at low temperatures and in the regime $\epsilon_c < 0 < \epsilon_c + U_c$ the Anderson model can be transformed to an effective model which considers only one electron on a local level which has the freedom of spin due to virtual processes. This is the essence behind the Schrieffer-Wolff transformation.

In this case of single occupancy the local level can be described by its spin $\vec{S}$. The coupling between the local level and the lead is a spin-spin interaction proportional to $J\vec{S} \cdot \vec{s}$, where J is the coupling strength and $\vec{s}$ is the spin of the lead electrons proportional to $\vec{s} \sim \sum_{\vec{k},\vec{k'},\sigma,\sigma'} (l^\dagger_{\vec{k}\sigma} \vec{\sigma}_{\sigma\sigma'} l'_{\vec{k'}\sigma})$. This is essentially the Kondo model.

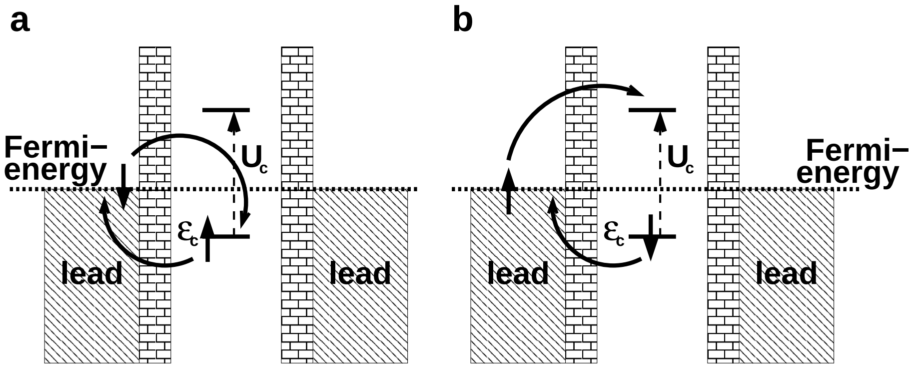

Figure 3.2: Important virtual processes of the Schieffer-Wolff transformation which flip the spin of the localized electron. The localized level is singly occupied, since $\epsilon_c < \epsilon_F = 0 < \epsilon_c + U_c$. a) The electron tunnels out of the localized level, thereby violating energy conservation. An electron with opposite spin tunnels on the localized level on a time scale $\Delta t \sim \hbar/|\epsilon_c|$ given by the uncertainty principle. b) An electron tunnels onto the single occupied localized level. On a time scale $\Delta t \sim \hbar/(\epsilon_c + U_c)$ the original electron tunnels out.

By Poor Man's Scaling, see Chapter 4, it can be shown that the coupling constant J increases with decreasing temperature. Below a characteristic temperature T_K, called Kondo temperature, which can be determined by scaling, the coupling becomes so strong that the localized electron builds a singlet with a cloud of lead electrons called the Kondo cloud. This state of a single occupied localized level strongly coupled to the cloud of lead electrons is called the Kondo-state. In this effect a new state, called the Kondo resonance, is generated at the Fermi-energy in the local density of states of the local level, see Fig. 3.3. One can visualize that in this strong coupling limit in the low temperature regime lead electrons at the Fermi-energy constantly tunnel in and out of the local level by virtual processes, thus creating a quasi-particle state at the Fermi-energy. The Kondo resonance is a many-body phenomenon, since strong correlations between the local electron and many lead electrons develop.

The presence of a Kondo resonance explains the Kondo effect, i.e. the increase of resistance at low temperature. In the low temperature regime, electrons close to the Fermi-energy contribute decisively to the conductance. Yet these electrons are scattered very effectively by the Kondo resonance, which leads to the increase in resistance.

3.2 Extension of Anderson model

In this section a model will be introduced that describes the InAs quantum dots discussed in Chapter 2. This model will be constructed by generalizing the Anderson model. First it will be explained which part of the Anderson Hamiltonian corresponds to which part of

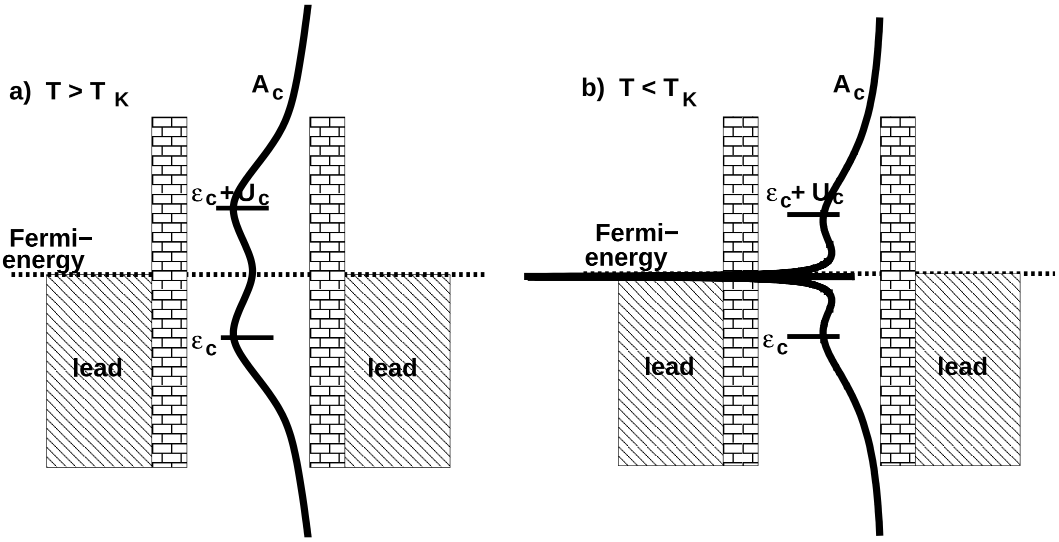

Figure 3.3: Development of the Kondo resonance. a) For temperatures T above the Kondo temperature T_K there is no Kondo effect. The local density of states $A_c(\omega)$ has two peaks at ϵ_c and $\epsilon_c + U_c$, respectively, where the width of the peaks is determined by $|V|^2$, i. e. by the strength of the coupling. b) For $T < T_K$ there is the Kondo resonance in the local density of states at the Fermi energy. It can be interpreted as a quasi-particle state which is created by lead electrons constantly tunnelling in and out the dot by virtual processes.

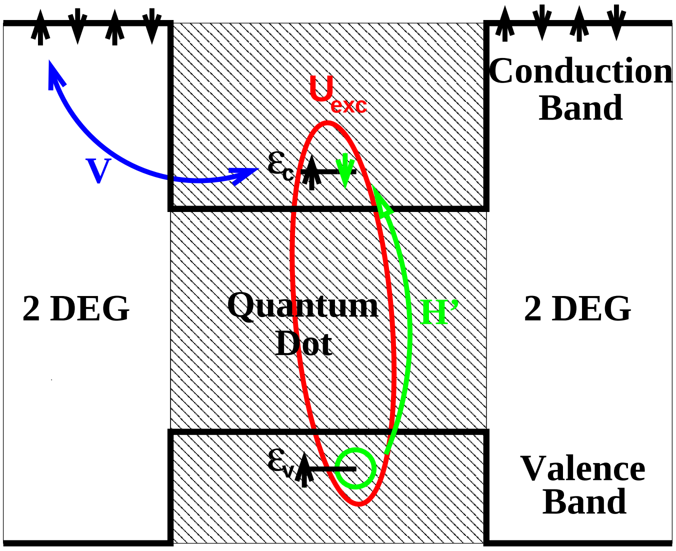

Figure 3.4: Model of quantum dot. Two localized levels are considered, the local conduction band level at energy ϵ_c and the local valence band level at ϵ_v. The local conduction band level is coupled to the lead (blue). The lead consists of a two dimensional electron gas in a mono-layer of InAs. The exciton binding energy between holes and electrons has strength U_{exc} (red). The excitation of excitons by laser light (green) is viewed as a perturbation of the system.

the InAs quantum dot. Then new terms will be added to the Hamiltonian to achieve a full description of the dot and the absorption process. The Hamiltonian is depicted in Fig. 3.4.

The local level of the Anderson model will correspond to the s-level of the local conduction band levels of the dot. All other conduction band levels of the quantum dot will be disregarded. The inclusion of other levels would be an interesting topic to study, but a model containing only the s-level is sufficient to produce the effects desired to be studied within the scope of this thesis. From now on the s-level will be referred to as the 'local conduction band level' to distinguish it from the 'local valence band level' which will be introduced below. All operators and parameters corresponding to the local conduction band will carry the subscript 'c' where 'c' stands for 'conduction band'. In this context 'charge-tunable quantum dot' means that the energy ϵ_c of the local conduction band level can be controlled experimentally, by changing an applied gate voltage.

To understand which part of the semiconductor quantum dot system will act as lead, it is necessary to go into one more detail about the experimental setup. As mentioned in Chapter 2, the InAs quantum dots are self-organized structures that form out of one and a half layer of InAs on top of GaAs by strain driven growth. In fact, after the InAs has migrated to form the quantum dots, there is still a mono-layer of InAs left. The InAs dots are surrounded by this mono-layer, like islands in an ocean. Moreover, in the conduction band of the InAs mono-layer a two dimensional electron gas can be formed, provided that the gate voltage is suitably tuned. This 2DEG will function as a lead and will be described by $\mathcal{H}_{\text{lead}}$ of Eq. (3.2b).

So far, no signature of the Kondo effect has been detected in the experiments, wherefore two presumption can be put forward. Firstly, if the local conduction band level of the dot is single occupied, which is necessary for the Kondo effect, the 2DEG is not filled sufficiently for the Kondo-state to build up. Just like the quantum dots are filled with electrons as the gate voltage is increased, the 2DEG is filled up with electrons, too. To occupy the local conduction band level with one electron, the gate voltage must be adjusted to a certain value V_1. The value of V_1 can vary from dot to dot, depending on its size. Therefore the amount of electrons in the 2DEG varies as one studies various different single occupied dots because the Fermi-energy of the 2DEG varies with V_1. However, in the experiments it has been found that on average the dots are occupied with four electrons before the 2DEG starts to be filled with electrons. Therefore the 2DEG will not be filled at all if there is just one electron in the dot, even for a dot that is considerably different from the average.

Secondly, the coupling between the dot and the 2DEG is too small. It has been found in the experiments that the coupling of the dots to the 2DEG becomes stronger with increasing gate voltage. Studying the experimental data, one arrives at the assumption that at V_1 the coupling is too weak for the Kondo-state to build up, even if the 2DEG would be sufficiently filled.

Experimentalists could overcome both obstacles by fabricating more 'shallow' dots, i.e. dots where the first localized level, the s-level, is very close or inside the continuum of states of the 2DEG. Such 'shallow' dots have indeed already been fabricated but they have not yet been studied experimentally.

We want to examine the excitation of excitons in the dot, so to construct the new model another local level is needed which originates from the InAs valence band that contains the holes. This local level will be referred to as the 'local valence band level'. Thus we are going to add a term $\sum_\sigma \epsilon_v v_\sigma^\dagger v_\sigma$, where ϵ_v is the energy of this level, again to be measured from the Fermi level, and $v_\sigma^\dagger (v_\sigma)$ creates (annihilates) an electron in the level with spin σ. In the language of holes, a local valence band level occupied with an electron with spin σ means that it contains a hole with opposite spin $\bar{\sigma}$. There is also a coulomb repulsion of two holes in the local level, thus we need to add a term with the repulsion energy U_v in the case in which there are no electrons in the level: $U_v(1 - v_\uparrow^\dagger v_\uparrow)(1 - v_\downarrow^\dagger v_\downarrow)$. Our new '2-level' dot-Hamiltonian reads

$$\mathcal{H}_{\text{dot}} = \sum_\sigma \epsilon_c c_\sigma^\dagger c_\sigma + \sum_\sigma \epsilon_v v_\sigma^\dagger v_\sigma + U_c \hat{n}_{c,\uparrow} \hat{n}_{c,\downarrow} + U_v(1 - \hat{n}_{v,\uparrow})(1 - \hat{n}_{v,\downarrow}), \tag{3.3}$$

where $n_{c,\sigma}$ and $n_{v,\sigma}$ are the number operators for the local conduction and valence band level, respectively.

We will neglect the coupling between the local valence band level and the valence band as the holes are very heavy and therefore couple only weakly to the valence band of the GaAs.

To describe the Coulomb attraction between holes and electrons of an excitons in the quantum dot, we still need a coupling between the local valence band and local conduction band level. As the energy of an exciton originates from the attractive Coulomb force between an electron and a hole, for every hole in the local valence band level the energy U_{exc} will be subtracted in the Hamiltonian for every electron in the local conduction band level. For instance, if there is one hole in the local valence band level and two electrons in the local conduction band level, the energy $2U_{\mathrm{exc}}$ will be subtracted. Therefore the term

$$\mathcal{H}_{\mathrm{level-coupling}} = -\sum_{\sigma,\nu=\uparrow,\downarrow} U_{\mathrm{exc}} \hat{n}_{c,\sigma}(1-\hat{n}_{v,\nu}) \tag{3.4}$$

will be added to the Hamiltonian.

Altogether, the model includes the following parameters: ϵ_c, U_c, ϵ_v, U_v, U_{exc}, $V_{\vec{k}c}$ and $\epsilon_{\vec{k}}$. Thus the parameter space is rather large and several constraints and assumptions for the parameters will be put forward. The dispersion relation $\epsilon_{\vec{k}}$ is given by the InAs band structure, whereby in this thesis the band will assumed to be flat. For more details about $\epsilon_{\vec{k}}$ and also the coupling strength $V_{\vec{k}c}$, see Chapter 5. In the following we are only interested in the case where at most one exciton is in the dot, which means that, after absorption, there is at least one electron in the local valence band level. This is justified by considering that the bandgap of order 1 eV is by far the largest energy scale of the problem, so a state with two holes is a highly excited state. In [8], a model for the InAs quantum dot is used which reduces to the model of this section in the case where only the s-level and at most one exciton in the dot are considered. From experimental data, they estimate the parameters U_c and U_{exc} to be approximately 50 meV and 35 meV, respectively, so they are of the same order of magnitude.

The last term that needs to be added to the Hamiltonian to complete the model is the term for exciton excitation by an incident photon. It is given by

$$\mathcal{H}' = \gamma \sum_{\sigma} \left(c_{\sigma}^{\dagger} v_{\sigma} + h.c. \right), \tag{3.5}$$

where the first term creates an electron in the local conduction band level and annihilates an electron in the local valence band level, i. e. it creates an exciton. The h. c. term annihilates an exciton. This part of the Hamilton is considered as perturbation of the system. In an absorption experiment, this perturbation is caused by a laser which exites the excitons. So the strength γ of the perturbation is proportional to the intensity of the laser. In the next section, the absorption spectrum of a quantum dot will be calculated with the help of Fermi's Golden Rule, with $\mathcal{H}'$ as perturbation. To use perturbation theory, we need $\gamma \ll 1$, which can be fulfilled for a small laser intensity.

The unperturbed part of the Hamiltonian, i.e. the part without $\mathcal{H}'$, will be referred to as $\mathcal{H}_0$, so that $\mathcal{H} = \mathcal{H}_0 + \mathcal{H}'$. The complete Hamiltonian is given by

$$\mathcal{H} = \mathcal{H}_{\mathrm{dot}} + \mathcal{H}_{\mathrm{level-coupling}} + \mathcal{H}_{\mathrm{lead}} + \mathcal{H}_{\mathrm{coupling}} + \mathcal{H}', \tag{3.6}$$

with

$$\begin{aligned}
\mathcal{H}_{\text{dot}} &= \sum_{\sigma} \epsilon_c c_\sigma^\dagger c_\sigma + \sum_{\sigma} \epsilon_v v_\sigma^\dagger v_\sigma + U_c \hat{n}_{c,\uparrow}\hat{n}_{c,\downarrow} + U_v(1-\hat{n}_{v,\uparrow})(1-\hat{n}_{v,\downarrow}), \\
\mathcal{H}_{\text{level-coupling}} &= -\sum_{\sigma,\nu} U_{exc}\hat{n}_{c,\sigma}(1-\hat{n}_{v,\nu}), \\
\mathcal{H}_{\text{lead}} &= \sum_{\vec{k},\sigma} \epsilon_{\vec{k}} l_{\vec{k}\sigma}^\dagger l_{\vec{k}\sigma}, \\
\mathcal{H}_{\text{coupling}} &= \sum_{\vec{k},\sigma} \left(V_{\vec{k}c} l_{\vec{k}\sigma}^\dagger c_\sigma + V_{\vec{k}c}^* c_\sigma^\dagger l_{\vec{k}\sigma} \right), \\
\mathcal{H}' &= \gamma \sum_{\sigma} \left(c_\sigma^\dagger v_\sigma + v_\sigma^\dagger c_\sigma \right). \qquad (3.7)
\end{aligned}$$

3.3 Ansatz for calculation of absorption spectra

Having constructed the model describing the semiconductor quantum dots in the last section, it will be the task of this section to derive predictions for optical absorption measurements from it. First an ansatz for calculating the absorption spectrum will be put forward. In general we will need NRG to calculate the spectra. In the limiting case $U_{\text{exc}} = 0$, however, it is possible, with a short calculation, to transcribe the ansatz to an expression which is proportional to the density of states of the local conduction band level. This short calculation will be presented and it will be shown that for the case $U_{\text{exc}} = 0$ there exists a simple interpretation for the absorption spectrum.

The absorption spectrum is calculated with help of Fermi's Golden Rule,

$$W_{\tilde{i}\to\tilde{f}} = \left(\frac{2\pi}{\hbar}\right) \int d\tilde{E}_{\tilde{f}}\rho(\tilde{E}_{\tilde{f}}) \left|\langle\tilde{i}|\mathcal{H}'|\tilde{f}\rangle\right|^2 \delta\left(\tilde{E}_{\tilde{f}} - \tilde{E}_{\tilde{i}}\right), \qquad (3.8)$$

which is derived, e.g., in [14]. It applies to the following situation: an unperturbed system is initially in a stationary eigenstate $|\tilde{i}\rangle$ with eigenenergy $\tilde{E}_{\tilde{i}}$. After a perturbation is switched on, there is a probability for the system to undergo a transition to $|\tilde{f}\rangle$, where $|\tilde{f}\rangle$ is another eigenstate of the unperturbed system with eigenenergy $\tilde{E}_{\tilde{f}}$. $W_{\tilde{i}\to\tilde{f}}$ is the transition rate, i.e. the transition probability per time unit. Here $\mathcal{H}'$ is the perturbation Hamilton and $\rho(\tilde{E}_{\tilde{f}})$ is the unperturbed density of states at energy $\tilde{E}_{\tilde{f}}$.

Due to the delta function, only transitions fulfilling energy conservation are possible. Therefore, studying absorption, we have to consider the energy of the absorbed photon. The state of the system can be decomposed into two parts: the state of the combined system of dot and lead and the state of the photon field:

$$|\tilde{\Psi}\rangle = |\Psi\rangle \otimes |\Psi_{photon-field}\rangle, \qquad (3.9)$$

with $|\Psi\rangle$ denoting the state of the system 'dot + lead'. The energy of the state $|\tilde{\Psi}\rangle$ can be decomposed in the same manner,

$$\tilde{E}_{\tilde{\Psi}} = E_\Psi + E_{\Psi,photon-field}, \qquad (3.10)$$

where E_Ψ is the energy of the system 'dot + lead'. Thus $\tilde{E}_{\tilde{f}} - \tilde{E}_{\tilde{i}} = E_f - E_i + E_{f,photon-field} - E_{i,photon-field}$. If a photon of frequency ω is absorbed, $E_{f,photon-field} - E_{i,photon-field} = -\hbar\omega$. We will now define ω by $\hbar\omega \equiv E_{f,photon-field} - E_{i,photon-field}$ and therefore allow for negative ω. Thus the absorption spectra will be plotted along negative energies in keeping with standard experimental conventions. Since the photon field is only important while considering energy conservation, no term for the photon-field is explicitly listed in the Hamiltonian and from now on the state of the photon field is neglected. Thus Fermi's Golden Rule becomes

$$W_{i \to f} = \left(\frac{2\pi}{\hbar}\right) \int \rho(E_f) \left|\langle i|\mathcal{H}'|f\rangle\right|^2 \delta\left(E_f - E_i + \hbar\omega\right) dE_f, \tag{3.11}$$

where now $|i\rangle$ and $|f\rangle$ refer to states of the combined 'dot + lead' system and $\rho(E_f)$ is the density of states of the combined system at energy E_f.

Eq. (3.11) already gives the desired absorption spectrum, apart from a constant factor. The absorption spectrum, a function of frequency ω, gives the probability that a photon with frequency ω is absorbed by the quantum dot in the ground state. Thus $W_{i\to f}$ is proportional to the absorption spectrum. The constant of proportionality is not important here, as the absorption spectrum is proportional to $|\gamma|^2$, where γ is the strength of the perturbation, see Section 3.2, and the value of γ depends on the intensity of the laser perturbation, which can be set to arbitrary values.

No analytical method is known to calculate all the matrix elements $\mathcal{H}'_{fi}$ exactly. In Chapter 5 they will be calculated with NRG. To do the numerical calculation, the integral has to be discretized into a sum, so $\int dE_f \rho(E_f)$ will be replaced by a sum over final states $\sum_f$. Therefore, to obtain a continuous function, one needs to 'broaden' the delta-function, see Section 5.2. On account of this, Eq. 3.11 can be written as

$$W_{i \to f} = \left(\frac{2\pi}{\hbar}\right) \sum_f \left|H'_{fi}\right|^2 \delta\left(E_f - E_i + \hbar\omega\right). \tag{3.12}$$

If the parameter $U_{\text{exc}} = 0$, it will now be shown that the function $W_{i\to f}(\omega)$ can be obtained by shifting the mirrored density of states function of the local conduction band level, calculated for the unperturbed system at $T = 0$. The local density of states at $T = 0$ for an electron with spin σ in the local conduction band level is given by

$$A_{c,\sigma}(\omega) = \sum_n \left[\left|\langle n|c_\sigma^\dagger|0\rangle\right|^2 \delta\left(\omega - (E_n - E_0)\right) + \left|\langle 0|c_\sigma^\dagger|n\rangle\right|^2 \delta\left(\omega + (E_n - E_0)\right)\right]. \tag{3.13}$$

Here $\hbar$ has been set to one, $\hbar = 1$, so frequency and energy have the same dimension. The states $|n\rangle$ denote states of the unperturbed combined system of dot and lead, i. e. the system described by $\mathcal{H}_0$, with energy E_n and $|0\rangle$ is the ground state with the ground state energy E_0. A derivation of Eq. 3.13 can be found in A.1.

If $U_{\text{exc}} = 0$, then the unperturbed Hamiltonian can be written as $\mathcal{H}_0 = \mathcal{H}_{c+lead} \otimes \mathbb{1}_v + \mathbb{1}_{c+lead} \otimes \mathcal{H}_v$, where the operators $\hat{O}_{c+lead}$ act only on the local conduction band level and the lead and the operators $\hat{O}_v$ act only on the local valence band level. In this case the energy and the states can be decomposed into a part determined by the local conduction band level and the lead, and into another part determined by the local valence band level:

$$U_{\text{exc}} = 0 \Rightarrow E = E_{c+lead} + E_v \, ; \, |\Psi\rangle = |\Psi_{c+lead}\rangle \otimes |\Psi_v\rangle . \tag{3.14}$$

Thus for $U_{\text{exc}} = 0$ the local density of states of the conduction band level for both spin up and spin down electrons $A_c(\omega)$ can be written as

$$\begin{aligned}
A_c(\omega) &= A_{c,\uparrow}(\omega) + A_{c,\downarrow}(\omega) \\
&= \sum_{n,\sigma} \Bigg[\left|\langle n_{c+lead}|c_\sigma^\dagger|0_{c+lead}\rangle\right|^2 \underbrace{|\langle n_v|0_v\rangle|^2}_{=\delta_{n_v,0_v}} \delta\left(\omega - (E_{n,c+lead} - E_{0,c+lead}) - (E_{n,v} - E_{0,v})\right) \\
&\quad + \left|\langle 0_{c+lead}|c_\sigma^\dagger|n_{c+lead}\rangle\right|^2 \underbrace{|\langle 0_v|n_v\rangle|^2}_{=\delta_{0_v,n_v}} \delta\left(\omega + (E_{n,c+lead} - E_{0,c+lead}) + (E_{n,v} - E_{0,v})\right) \Bigg] \\
&= \sum_{n_{c+lead},\sigma} \Big[\left|\langle n_{c+lead}|c_\sigma^\dagger|0_{c+lead}\rangle\right|^2 \delta\left(\omega - (E_{n,c+lead} - E_{0,c+lead})\right) \\
&\quad + \left|\langle 0_{c+lead}|c_\sigma^\dagger|n_{c+lead}\rangle\right|^2 \delta\left(\omega + (E_{n,c+lead} - E_{0,c+lead})\right) \Big] .
\end{aligned} \tag{3.15}$$

To compare this result to the absorption spectrum, Eq. (3.12) needs to be reformulated for the case $U_{\text{exc}} = 0$ and for $\hbar = 1$:

$$\begin{aligned}
W_{i\to f} &= 2\pi \sum_f \underbrace{\left|\langle f|H'|i\rangle\right|^2}_{=\left|\langle i|H'|f\rangle\right|^2} \delta\left(E_f - E_i + \omega\right) \\
&= 2\pi|\gamma|^2 \sum_{f,\sigma} \Big[\left|\langle i_{c+lead}|c_\sigma^\dagger|f_{c+lead}\rangle\right|^2 |\langle i_v|v_\sigma|f_v\rangle|^2 + \\
&\quad |\langle i_{c+lead}|c_\sigma|f_{c+lead}\rangle|^2 \left|\langle i_v|v_\sigma^\dagger|f_v\rangle\right|^2 \Big] \cdot \\
&\quad \delta\left(\omega + E_{f,c+lead} - E_{i,c+lead} + E_{f,v} - E_{i,v}\right) .
\end{aligned} \tag{3.16}$$

If we set the initial state to be the ground state, $|i\rangle = |0\rangle$, change the notation from 'f' to 'n' and note that $\langle 0_v|v_\sigma = 0$ because we define the ground state to have a doubly occupied local valence band level, we obtain

$$\begin{aligned}
W_{0\to n} &= 2\pi|\gamma|^2 \sum_{n,\sigma} |\langle 0_{c+lead}|c_\sigma|n_{c+lead}\rangle|^2 \left|\langle 0_v|v_\sigma^\dagger|n_v\rangle\right|^2 \cdot \\
&\quad \delta\left(\omega + (E_{n,c+lead} - E_{0,c+lead}) + (E_{n,v} - E_{0,v})\right) .
\end{aligned} \tag{3.17}$$

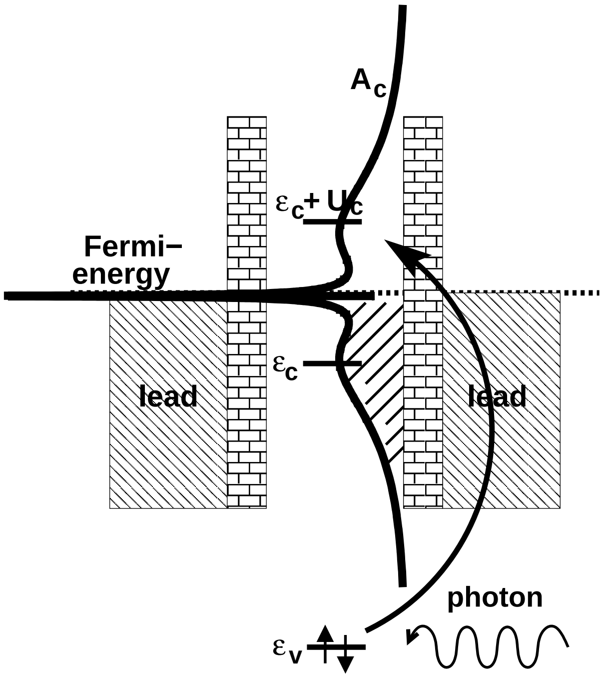

Figure 3.5: Illustration of the absorption process for the limiting case $U_{exc} = 0$, where the local valence band level is decoupled. In the absorption process, an incident photon excites an electron from the local valence band level into the local conduction band level. For $T = 0$, only states above the Fermi energy are unoccupied. Since, for the case $U_{exc} = 0$, the absorption spectrum is proportional to the available density of states, the absorption spectrum will be the mirrored positive energy half of the local density of states function, shifted by ϵ_v.

As $|0_v\rangle$ is doubly occupied, the matrix element $\left|\langle 0_v|v_\sigma^\dagger|n_v\rangle\right|$ is 1 for a singly occupied local v-level and 0 otherwise. Without a magnetic field, the singly occupied local valence band states are degenerate, thus $E_{n,v} - E_{0,v}$ is a constant shift, $\Delta\omega \equiv E_{n,v} - E_{0,v} = 2\epsilon_v - \epsilon_v = \epsilon_v$. Finally we see that

$$W_{0\to n} = 2\pi|\gamma|^2 \sum_{n_{c+lead},\sigma} \left|\langle n_{c+lead}|c_\sigma^\dagger|0_{c+lead}\rangle\right|^2 \delta\left(\omega + (E_{n,c+lead} - E_{0,c+lead}) + \Delta\omega\right). \quad (3.18)$$

We see that, apart from a constant factor, Eq. (3.18) is the shifted and mirrored positive energy part of Eq. (3.15). This result can be understood by looking at Fig. 3.5. The initial state, before the absorption, is the Kondo state, thus the local density of states of the local c-level, given by Eq. (3.15), features the Kondo resonance at the Fermi-energy, see Section 3.1. At $T = 0$, all states up to the Fermi-energy are occupied. The density of states of the unoccupied states above the Fermi-energy is given by the positive energy part of Eq. (3.15). If $U_{\text{exc}} = 0$, the local v-level is completely decoupled from the rest of the system. In the absorption process, one electron is taken out of the v-level and is put into the c-level. Since all available, i. e. unoccupied, states of the c-level are at or above the Fermi-energy, one needs at least the energy ϵ_v, which explains the shift $\Delta\omega$. Because the v-level is completely decoupled, the absorption is proportional to the density of unoccupied states, which explains the relation between the eqs. (3.15) and (3.18).

3.4 Other theoretical approaches

We know about two other approaches to calculate the absorption spectrum of a quantum dot. In [15], the same model is used as in this thesis, expcept for the fact that it is more general, since more than one p-level is considered, cf. Section 3.2. However, in [15] the restriction is made that the Coulomb interactions in the dot are considered to be small compared to the quantization energies. Therefore the Coulomb interactions in the dot can be included with perturbation theory in the calculation. The presented results are only qualitative. Our results, see Chapter 6, agree with the two main results in [15]: In the Kondo regime, the width of the absortion spectrum is determined by the Kondo temperature, and the position and shape of the absorption spectrum are strongly dependent on the applied gate voltage, which shifts the energies of the local levels with respect to the Fermi energy.

In [16], again a similar but more complicated model is used. As our model described in this chapter, the model consists of two local levels coupled by an exciton binding energy. However, in [16], both the local valence band level and the local conduction band level are coupled to two different leads. Four different rigimes are found for the model, where both levels can either couple 'ferromagnetic' or 'antiferromagnetic' to the lead, see Chapter 4 for a definition for 'ferromagnetic' and 'antiferromagnetic' coupling. No closed expression is given for the absorption spectrum. The presented results are constricted to proportionalities in the low energy regime.

Chapter 4

Poor Man's Scaling

In Section 3.2 the Hamiltonian of the semi-conductor quantum dot system was introduced. Furthermore an ansatz for the calculation of the absorption spectrum of the dots was presented. As already mentioned, it is possible to calculate the absorption spectrum with the help of NRG, aswill be discussed in Chapter 5. However, to interpret the results it will be helpful to have a qualitative understanding of the system's behaviour. Such a qualitative understanding can be obtained by Anderson's Poor Man's Scaling approach [3]. To be more specific, using scaling one can see how the system behaves as the temperature is lowered.

The Poor Man's Scaling approach will be applied to the Kondo model in Section 4.1, where the Kondo Model itself will also be explained. The same approach is applied to the Anderson model in Section 4.2. We will see that the scaling for the Anderson model has to stop when a certain temperature is reached. At this temperature, however, the Anderson model can be transformed to the Kondo model by the Schrieffer-Wolff transformation, see Section 3.1 and [2], and the scaling can be continued for the obtained Kondo model as explained in Section 4.1. In Section 4.3, the scaling method will be used for the extended Anderson model of Section 3.2, which will turn out to be an easy task if the results of Section 4.2 are used. It will be shown that two Kondo temperatures T_{K1} and T_{K2} determine the behaviour of the system.

4.1 Scaling for the Kondo model

In this section the Poor Man's Scaling Approach will be applied to the Kondo model. First of all the Kondo model will be introduced, followed by the explanation of the idea of scaling.

4.1.1 Kondo model

The Kondo model deals with a local moment with spin S which is coupled to a lead. In the following we set $S = 1/2$. In this case we can employ the Kondo model for our quantum dot system, where the local moment corresponds to a singly occupied quantum dot level interacting with a lead. The Hamiltonian describing the lead is the same as the one used in Chapter 3, $\mathcal{H}_{lead} = \sum_{\vec{k},\sigma} \epsilon_{\vec{k}} l^\dagger_{\vec{k}\sigma} l_{\vec{k}\sigma}$, where $l^\dagger_{\vec{k}\sigma}(l_{\vec{k}\sigma})$ creates (destroys) a quasi-particle with wavevector $\vec{k}$, spin σ and energy $\epsilon_{\vec{k}}$. Potential scattering of the lead electrons on the dot can be included into the lead Hamiltonian by redefining the energy of the quasi particles, see [2]. Besides potential scattering, there is scattering due to a Heisenberg exchange interaction between the local moment and the spin of the lead electrons. This interaction, together with the description of the lead, is given by the Kondo Hamiltonian,

$$\mathcal{H}_{Kondo} = \sum_{\vec{k},\vec{k}'} J_{\vec{k},\vec{k}'} \left(S^+ l^\dagger_{\vec{k},\downarrow} l_{\vec{k}',\uparrow} + S^- l^\dagger_{\vec{k},\uparrow} l_{\vec{k}',\downarrow} + S^z \left(l^\dagger_{\vec{k},\uparrow} l_{\vec{k}',\uparrow} - l^\dagger_{\vec{k},\downarrow} l_{\vec{k}',\downarrow} \right) \right) + \mathcal{H}_{lead}. \tag{4.1}$$

The first two terms describe the scattering of a lead electron on the local moment, whereby the spins of the local moment and the lead electron are flipped. The last two terms relate to scattering without spin-flip. For the case $S = 1/2$ the Hamiltonian (4.1) can be obtained from the Anderson Hamiltonian (3.1) by the Schrieffer-Wolff transformation, see Section 3.1 or [2].

In the following we consider a localized, $\vec{k}$-independent interaction and a slightly generalized model, where the couplings $J_\pm$ for spin-flip scattering can be different from the coupling J_z for potential scattering,

$$\mathcal{H}_{Kondo} = \sum_{\vec{k},\vec{k}'} \left(J_+ S^+ l^\dagger_{\vec{k},\downarrow} l_{\vec{k}',\uparrow} + J_- S^- l^\dagger_{\vec{k},\uparrow} l_{\vec{k}',\downarrow} + J_z S^z \left(l^\dagger_{\vec{k},\uparrow} l_{\vec{k}',\uparrow} - l^\dagger_{\vec{k},\downarrow} l_{\vec{k}',\downarrow} \right) \right) + \mathcal{H}_{lead}. \tag{4.2}$$

4.1.2 Scaling

As mentioned in Chapter 1, perturbation theory in the coupling $J_{\vec{k},\vec{k}'}$ fails as the temperature is decreased below a certain limit. Therefore we have to rely on other methods to investigate the low temperature regime, as e. g. NRG. To obtain a qualitative understanding of the low temperature regime one can use Poor Man's Scaling. The central idea behind this approach is the following. Let's consider the lead. We assume that it has a constant density of states between two band edges with energies, say, -D and D and that it is half-filled, i. e. the Fermi-energy is zero, see Fig. 4.1. At low temperatures the highly excited states near the band edges with energy $|D| - \delta D \leq \epsilon_{\vec{k}} \leq |D|$ are either completely occupied or completely empty, and we would like to neglect them. Unfortunately it turns out, e. g. by pursuing perturbation theory, that the states close to the band edges are important, e. g. for calculating the resistivity, and therefore cannot be disregarded, see [2]. Thus the following procedure is employed. We eliminate the states with energy $D - \delta D \leq |\epsilon_{\vec{k}}| \leq D$ and introduce an effective Hamiltonian $\mathcal{H}'$ with exactly the same form as $\mathcal{H}$, which describes a local moment coupled to a lead with a constant density of states between the band edges $-D + \delta D$ and $D - \delta D$. Of course the effective Hamiltonian must produce the same results, for instance the scattering rate off the impurity for lead electrons with energies $-D + \delta D \leq \epsilon_{\vec{k}} \leq D - \delta D$ has to be the same for both Hamiltonians. This

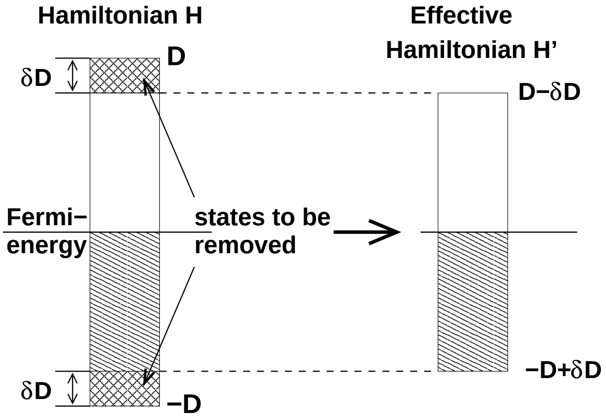

Figure 4.1: Idea of poor man's scaling: Highly excited states at the band edges are removed and absorbed in renormalized parameters of an effective Hamiltonian $\mathcal{H}'$ which has the same form as the original Hamiltonian $\mathcal{H}$.

can be achieved by absorbing the high energy excitations into renormalized parameters of $\mathcal{H}'$.

To eliminate the states at the band edges, we separate the total wavefunction into three parts, $\psi = \psi_0 + \psi_1 + \psi_2$. Here ψ_1 is the component of the total wavefunction with no conduction electrons at the upper band edge or no holes at the lower band edge and ψ_0 and ψ_2 are the parts in which there is at least one hole at the lower band edge or at least one electron at the upper band edge, respectively. Here we have neglected highly excited states which have both electrons at the upper band edge and holes at the lower band edge. If we introduce the projection operators P_n which project the total wavefunction onto the subspace of the components ψ_n and define $\mathcal{H}_{nn'} \equiv P_n H P_{n'}$, we can write the Schrödinger equation $\mathcal{H}\psi = E\psi$ as

$$\begin{pmatrix} \mathcal{H}_{00} & \mathcal{H}_{01} & \mathcal{H}_{02} \\ \mathcal{H}_{10} & \mathcal{H}_{11} & \mathcal{H}_{12} \\ \mathcal{H}_{20} & \mathcal{H}_{21} & \mathcal{H}_{22} \end{pmatrix} \begin{pmatrix} \psi_0 \\ \psi_1 \\ \psi_2 \end{pmatrix} = E \begin{pmatrix} \psi_0 \\ \psi_1 \\ \psi_2 \end{pmatrix} . \tag{4.3}$$

For instance the component $\mathcal{H}_{21}$ scatters an electron from state $\vec{k}$ with energy $\epsilon_{\vec{k}}$ in the range $-D + \delta D \leq \epsilon_{\vec{k}} \leq D - \delta D$, into a state $\vec{q}$ in the unoccupied region at the upper band edge, $D - \delta D \leq \epsilon_{\vec{q}} \leq D$,

$$\mathcal{H}_{12} = \sum_{\vec{q},\vec{k}} J_+ S^+ l^\dagger_{\vec{q},\downarrow} l_{\vec{k},\uparrow} + J_- S^- l^\dagger_{\vec{q},\uparrow} l_{\vec{k},\downarrow} + J_z S^z \left(l^\dagger_{\vec{q},\uparrow} l_{\vec{k},\uparrow} - l^\dagger_{\vec{q},\downarrow} l_{\vec{k},\downarrow} \right) . \tag{4.4}$$

To first order in δD, one can neglect the components $\mathcal{H}_{02}$ and $\mathcal{H}_{20}$. Thus, from Eq. (4.3) for the effective Hamiltonian we obtain $\mathcal{H}'\psi_1 = E\psi_1$,

$$\left[\mathcal{H}_{11} + \mathcal{H}_{12} \left(E - \mathcal{H}_{22} \right)^{-1} \mathcal{H}_{21} + \mathcal{H}_{10} \left(E - \mathcal{H}_{00} \right)^{-1} \mathcal{H}_{01} \right] \psi_1 = E\psi_1 . \tag{4.5}$$

The first part, $\mathcal{H}_{11}$, already has the form of the original Hamiltonian (4.2), but it does not contain any contributions from states at the band edges, which are included in the second and third term. These two terms will now be approximated by lowest order perturbation theory in the coupling. This will yield terms that can be added to $\mathcal{H}_{11}$ by renormalizing the parameters.

In the lowest order in the coupling, i. e. zeroth order, $\mathcal{H}_{00}$ and $\mathcal{H}_{22}$ are given by the lead Hamiltonian $\mathcal{H}_{lead}$. In this order, the second and third term of Eq. (4.5) can be written as $\mathcal{H}_{12}\left(E-\mathcal{H}_{lead}\right)^{-1}\mathcal{H}_{21}$ and $\mathcal{H}_{10}\left(E-\mathcal{H}_{lead}\right)^{-1}\mathcal{H}_{01}$, respectively. These terms correspond to virtual scattering of conduction band electrons or conduction band holes, respectively, to the band edges, which are second order processes in the coupling. In these processes we start and finish with a state without excitations at the band edges, i. e. they can be understood as corrections to the Hamiltonian $\mathcal{H}_{11}$ resulting from the band edges. The processes are presented in Fig. 4.2. We will now take a closer look at diagrams a) and b) and demonstrate, in which way they can be absorbed in renormalized parameters of $\mathcal{H}'$. The other diagrams can be interpreted along the same lines.

The diagram Fig. 4.2 a) illustrates two parts (black, red) of the contribution of the term $\mathcal{H}_{12}\left(E-\mathcal{H}_{lead}\right)^{-1}\mathcal{H}_{21}$, whereby the contribution corresponding to the black illustration is given by

$$J_+J_-\sum_{\vec{q},\vec{k},\vec{q}',\vec{k}'} S^-l^\dagger_{\vec{k}',\uparrow}l_{\vec{q},\downarrow}\frac{1}{E-\mathcal{H}_{lead}}S^+l^\dagger_{\vec{q}',\downarrow}l_{\vec{k},\uparrow}. \tag{4.6}$$

In the black part of the diagram, a conduction band electron, depicted by the curved line, scatters twice on the localized electron, represented by the straight line at the bottom. First, the conduction band electron is in a state $\vec{k}$ between the band edges, i. e. $-D+\delta D<\epsilon_{\vec{k}}<D-\delta D$, with spin up and the localized electron has spin down. The interaction flips both spins and scatters the conduction band electron into an intermediate state $\vec{q}$ at the upper band edge, i. e. $D-\delta D<\epsilon_{\vec{q}}<D$. After the second interaction, both spins are flipped again and the conduction band electron is scattered back into a state $\vec{k}'$ between the band edges.

After a short calculation, see Appendix A.2.1, Eq. (4.6) can be written as

$$J_+J_-\sum_{\vec{q},\vec{k},\vec{q}',\vec{k}'} S^-S^+l^\dagger_{\vec{k}',\uparrow}l_{\vec{k},\uparrow}l_{\vec{q},\downarrow}l^\dagger_{\vec{q}',\downarrow}\left(E-H_{lead}-\epsilon_{\vec{q}'}+\epsilon_{\vec{k}}\right)^{-1}. \tag{4.7}$$

For small δD, $\epsilon_{\vec{q}'}=D$ can be used. If the energy E is measured relative to the ground state of the conduction electron gas then $\mathcal{H}_{\text{lead}}$ can effectively be set equal to zero. Furthermore, regarding that the upper band edge is unoccupied in the initial state, we have $l_{\vec{q},\downarrow}l^\dagger_{\vec{q}'}=\delta_{\vec{q},\vec{q}'}$, thus we have $\sum_{\vec{q},\vec{q}'}\delta_{\vec{q},\vec{q}'}=\sum_{\vec{q}}1=\rho_0\delta D$, where ρ_0 is the density of states which we assumed to be constant. For $S=1/2$ we can use the relation $S^-S^+=1/2-S^z$. Collecting everything we see that Eq. (4.7) is equal to

$$J_+J_-\sum_{\vec{k},\vec{k}'}\left(\frac{1}{2}-S^z\right)\rho_0\delta Dl^\dagger_{\vec{k}',\uparrow}l_{\vec{k},\uparrow}\left(E-D+\epsilon_{\vec{k}}\right)^{-1}. \tag{4.8}$$

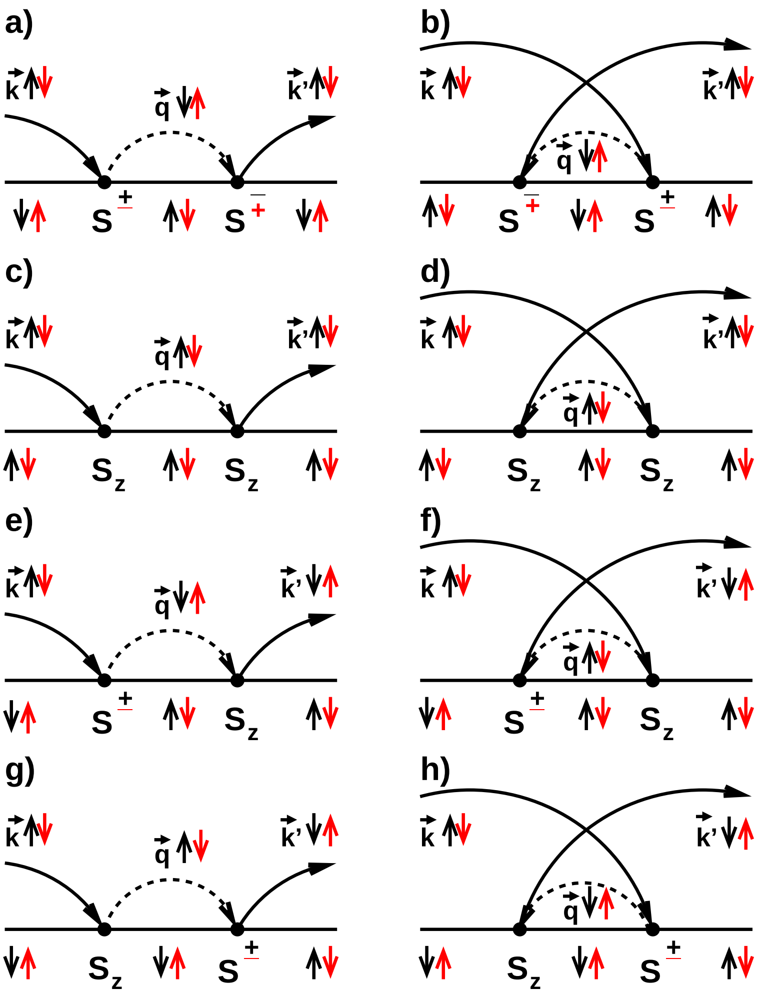

Figure 4.2: Scattering between conduction band electrons (curved lines) and the localized electron (straight lines) in second order in the coupling, which includes intermediate states at the lower or upper band edges. In the scaling procedure the diagrams are summed up and the contributions are absorbed in renormalized parameters of an effective Hamiltonian $\mathcal{H}'$. On the left hand side, a conduction band electron is scattered into an intermediate state $\vec{q}$ at the upper band edge. On the right hand side, an electron at the lower band edge in state $\vec{q}$ is scattered in a state $\vec{k'}$ between the band edges. After the scattering a hole with state $\vec{q}$ propagates until a conduction band electron with state $\vec{k}$ between the band edges is scattered into state $\vec{q}$.

Before we show how this correction can be added to $\mathcal{H}_{11}$ to build the effective Hamiltonian, we first compute the other three contributions from the diagrams a) and b). The term corresponding to the red illustration of a) can be evaluated in an analogous manner as the term corresponding to the black part. Here $S^+S^- = 1/2 + S^z$ is used and all spins have opposite directions. The result is

$$J_+J_- \sum_{\vec{k},\vec{k}'} \left(\frac{1}{2} + S^z\right) \rho_0 \delta D l^\dagger_{\vec{k}',\downarrow} l_{\vec{k},\downarrow} \left(E - D + \epsilon_{\vec{k}}\right)^{-1}. \tag{4.9}$$

Calculating the contributions of diagram b), one has to regard that the excitation at the lower band edge are holes. Here, in the initial state, all states at the lower band edge are occupied, thus $l^\dagger_{\vec{q},\uparrow\downarrow} l_{\vec{q}',\uparrow\downarrow} = \delta_{\vec{q},\vec{q}'}$. Furthermore we set $\epsilon_{\vec{q}'} = -D$. Then

$$J_+J_- \sum_{\vec{k},\vec{k}'} \left(\frac{1}{2} + S^z\right) \rho_0 \delta D \left(\delta_{\vec{k},\vec{k}'} - l^\dagger_{\vec{k}',\uparrow} l_{\vec{k},\uparrow}\right) \left(E - D - \epsilon_{\vec{k}'}\right)^{-1} \tag{4.10}$$

is the correction corresponding to the black part and

$$J_+J_- \sum_{\vec{k},\vec{k}'} \left(\frac{1}{2} - S^z\right) \rho_0 \delta D \left(\delta_{\vec{k},\vec{k}'} - l^\dagger_{\vec{k}',\downarrow} l_{\vec{k},\downarrow}\right) \left(E - D - \epsilon_{\vec{k}'}\right)^{-1} \tag{4.11}$$

is the contribution of the red part. The term $\delta_{\vec{k},\vec{k}'} - l^\dagger_{\vec{k}',\uparrow\downarrow} l_{\vec{k},\uparrow\downarrow}$ results from commuting $l_{\vec{k},\uparrow\downarrow} l^\dagger_{\vec{k}',\uparrow\downarrow}$.

Now we will add these four corrections to $\mathcal{H}_{11}$. In the terms $1/2 \pm S^z$ we will omit the constant terms and just keep the S^z terms, since the constant terms do not contain any operators acting on the local moment and therefore describe potential scattering of the lead electrons, which can be incorporated in $\mathcal{H}_{\text{lead}}$. In the terms $\delta_{\vec{k},\vec{k}'} - l^\dagger_{\vec{k}',\uparrow\downarrow} l_{\vec{k},\uparrow\downarrow}$ we will not consider the $\delta_{\vec{k},\vec{k}'}$ part, because it represents a constant term, i. e. a change in the ground state energy, which can be included in a redefinition of E. By defining

$$\delta J_z \equiv -J_+J_-\rho_0 \delta D \left(\frac{1}{E - D + \epsilon_{\vec{k}}} + \frac{1}{E - D - \epsilon_{\vec{k}'}}\right), \tag{4.12}$$

all terms left can be included into $\mathcal{H}_{11}$ by replacing J_z by a renormalized parameter, $J_z \longrightarrow J_z + \delta J_z$.

All other contributions are listed in Section A.2.2 in the appendix. It turns out that the corrections derived from diagrams c) and d) just contain operators acting on the lead and thus can be incorporated as potential scattering in $\mathcal{H}_{\text{lead}}$, or they are constant terms which again can be accounted for by including them in a redefinition of E. The corrections stemming from diagrams e), f), g) and h) can be absorbed in a renormalized parameter $J_\pm \longrightarrow J_\pm + \delta J_\pm$, with

$$\delta J_\pm \equiv -J_\pm J_z \rho_0 \delta D \left(\frac{1}{E - D + \epsilon_{\vec{k}}} + \frac{1}{E - D - \epsilon_{\vec{k}'}}\right). \tag{4.13}$$

Thus we have constructed a Hamiltonian of the form (4.2). The states at the band edges have been removed, but their effect on the states between the band edges has been incorporated in renormalized parameters.

From eqns. (4.12) and (4.13) we can gain useful information about the system. For low energy excitations relative to D the E dependence can be neglected. Similarly for scattering of conduction electrons with energies near the Fermi energy, which are the dominant processes at low temperature, $\epsilon_{\vec{k}}$ and $\epsilon_{\vec{k}'}$ can also be neglected. Hence, we find

$$\begin{aligned} \delta J_z &= 2\rho_0 J_+ J_- \frac{\delta D}{D}, \\ \delta J_\pm &= 2\rho_0 J_z J_\pm \frac{\delta D}{D}. \end{aligned} \tag{4.14}$$

This can be written as a set of coupled differential equations for J_z and $J_\pm$,

$$\begin{aligned} \frac{\partial J_z}{\partial D} &= -2\rho_0 \frac{J_+ J_-}{D}, \\ \frac{\partial J_\pm}{\partial D} &= -2\rho_0 \frac{J_\pm J_z}{D}. \end{aligned} \tag{4.15}$$

The minus signs appear due to the fact that D is decreased by δD in the scaling process. The equations are called 'scaling equations'. We will first study the isotropic and then the anisotropic case.

For isotropic coupling, $J_z = J_\pm = J$, we can write Eq. (4.15) as

$$\frac{\partial(\rho_0 J)}{\partial D} = -2\frac{(\rho_0 J)^2}{D}. \tag{4.16}$$

Let's consider $J < 0$ first. This case is called 'ferromagnetic coupling', because for $J_z = J < 0$ the S_z term of the Kondo Hamiltonian favours parallel spins of the conduction band electrons and the local moment. Here, since the derivative in Eq. (4.16) is always negative, J decreases as D increases, i. e. J is increased as D is decreased. Hence, $J \to 0$ as $D \to 0$, since zero is a fix point. As Eq. (4.16) was derived by second order perturbation theory in the coupling J, the scaling works better and better as $J \to 0$. We scale towards a free impurity spin.

For the anti-ferromagnetic case $J_z = J > 0$, $J \to \infty$ as $D \to 0$. Therefore the perturbation theory will break down at some point of the scaling process, Eq. (4.16) only holds for $\rho_0 J \ll 1$. If we recall that the scaling process is performed to investigate the low temperature regime, i. e. we actually would like to continue the scaling process until $D \sim k_B T$, this can be reformulated into the statement that in the anti-ferromagnetic case, the scaling is bound to fail at some temperature T. However, we are still able to gain information from the scaling equation (4.16). If we write (4.16) as

$$\frac{\partial(1/J)}{\partial(\ln D)} = 2\rho_0, \tag{4.17}$$

we see that

$$\begin{aligned}
\frac{1}{J}-\frac{1}{\tilde{J}} &= 2\rho_0\left(\ln D-\ln\tilde{D}\right)\\
\Rightarrow \frac{1}{J}-2\rho_0\ln D &= \frac{1}{\tilde{J}}-2\rho_0\ln\tilde{D}\\
\Rightarrow De^{-1/(2J\rho_0)} &= \tilde{D}e^{-1/(2\tilde{J}\rho_0)}\equiv k_BT_K,
\end{aligned}\tag{4.18}$$

where the Kondo temperature T_K has been defined. We see that T_K is a 'scaling invariant', which stays constant during the scaling process. Moreover, two materials with different J, ρ_0, and D, but with the same Kondo temperature T_K are equivalent below T_K. For low temperatures their Hamiltonians can be scaled towards the same effective Hamiltonian, thus they have the same low temperature properties. One very important consequence following from this argument is that T_K is the only relevant energy scale. Therefore the temperature dependence of all observables must be one universal function of T/T_K. For instance, just by following these scaling arguments, we know that the susceptibility must be an universal function f_χ of T/T_K,

$$\chi=\chi_0 f_\chi\left(T/T_K\right).\tag{4.19}$$

Looking at Eq. (4.18), we see that J diverges at $D/k_B=T_K$, i. e. at $T=T_K$. This is an artifact of the second order perturbation theory. The scaling process can be carried out by third order perturbation theory. As the calculation is lengthy and bears no new illuminating facts, see [2], just the result for the Kondo temperature will be quoted here,

$$k_BT_K\sim D\left|2J\rho_0\right|^{1/2}e^{-1/(2J\rho_0)}.\tag{4.20}$$

We see that J diverges now at $T=0$. This time, this is no artefact of the perturbation theory. In fact, using the Numerical Renormalization Group, K. Wilson showed that $J\rho_0\to\infty$, as $D\to 0$ or $T\to 0$ [4]. He also showed that T_K remains the only energy scale even for couplings $\rho_0 J\geq 1$.

We now turn to the anisotropic case with the constraint $J_+=J_-=J_\pm$. If we divide the first equation of (4.15) by the second and integrate by parts, we see that $J_\pm^2-J_z^2$ stays constant during the scaling process,

$$J_\pm^2-J_z^2=\text{const.}\tag{4.21}$$

Therefore $J_\pm$, understood as a function of J_z, will flow along curves with constant $J_\pm^2-J_z^2$. This is shown in Fig. 4.3. As $\partial J_z/\partial D$ is always negative, cf. Eq. (4.15), J_z always increases as the scaling is carried out. Therefore the flow is always in the direction of increasing J_z.

4.2 Scaling for Anderson model

In this section the scaling method will be applied to the Anderson Model, see Section 3.1 for a description of the model. It was first done by F. Haldane, see [17]. In contrast

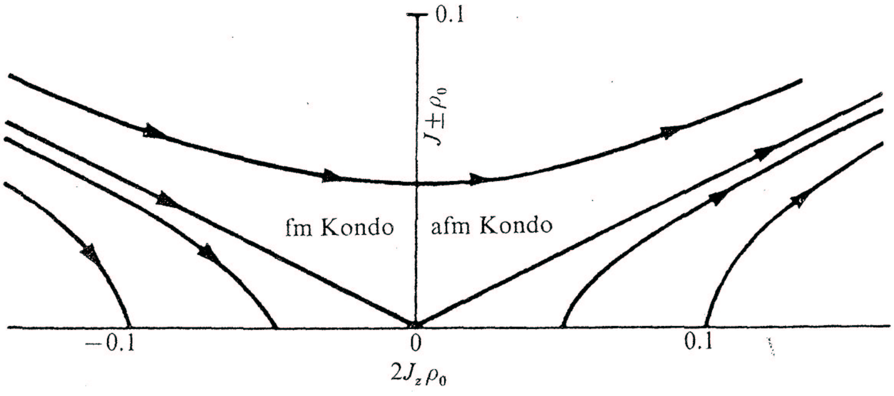

Figure 4.3: Scaling trajectories for the anisotropic Kondo model, calculated with second order perturbation theory. As J_z always increases in the scaling process, the direction of the flow is to the right. The line $J_\pm = 0$ is a fix point. If it is reached or if the scaling starts with $J_\pm = 0$, it will always stay constant at $J_\pm = 0$. However, if $J_z > 0$, this fix point is unstable, since a slight perturbation away from $J_\pm = 0$ will lead to trajectory which flows to $J_z = J_\pm = \infty$.

to the Kondo model, where we have just the freedom of spin of the local moment, the Anderson model includes hybridization between the lead and the local level. The charge on the local level can change and one has charge fluctuations, too, in contrast to the Kondo model which allows spin fluctuations only. In complete analogy to the previous section, we will now remove the states at the band edges and absorb their effect on the system into renormalized parameters of an effective Hamiltonian, which has the same form as the Anderson Hamiltonian. To be more specific, will will calculate the effect of second order processes, where lead electrons are scattered to the band edges and back, on the charge fluctuations. Therefore, we will calculate the change in the energies E_0, E_1 and E_2 which correspond to an empty, a singly or a doubly occupied local level, respectively. For this purpose, we separate the states and the Hamiltonian analogously to Eq. (4.3). The parts $\mathcal{H}_{01}$ and $\mathcal{H}_{12}$ of the Hamiltonian can be written as

$$\begin{aligned}\mathcal{H}_{01} &= \sum_{\vec{q},\sigma} V_{\vec{q}} \left(X_{1,\sigma:0} + X_{2:1,-\sigma}\right) l_{\vec{q},\sigma}, \\ \mathcal{H}_{12} &= \sum_{\vec{q},\sigma} V_{\vec{q}}^{*} l_{\vec{q},\sigma}^{\dagger} \left(X_{0:1,\sigma} + X_{1,\sigma:2}\right). \end{aligned} \tag{4.22}$$

Here the Hubbard X-operator notation is used, where $X_{p:q}$ denotes $|p\rangle\langle q|$ and $|p\rangle$, $|q\rangle$ are many body states. In (4.22), the subscripts 0, $(1, \sigma)$, and 2 label the empty, singly, and doubly occupied dot, respectively, where σ denotes the spin in the case of single occupation. For instance,

$$X_{1,\sigma:0} = c_\sigma^\dagger(1 - \hat{n}_{c,-\sigma}) \text{ and } \mathrm{X}_{0:1,\sigma} = \mathrm{c}_\sigma(1 - \hat{\mathrm{n}}_{\mathrm{c},-\sigma}). \tag{4.23}$$

Proceeding as in the previous section, we illustrate the second order processes, where a conduction band electron or hole between the two band edges is scattered to one of the band edges and subsequently is scattered back, in diagrams, see Fig. 4.4. Here the dashed baseline depicts the conduction electron at the upper band edge (upper four panels) or the conduction hole at the lower band edge (lower four panels), respectively. The solid lines correspond to the local level.

Using lowest order perturbation theory in the coupling, where $\mathcal{H}_{00}$ and $\mathcal{H}_{22}$ can be replaced by $\mathcal{H}_0 = \mathcal{H}_{\text{dot}} + \mathcal{H}_{\text{lead}}$, cf. Eq. (3.1), diagram a) yields the contribution

$$\sum_{\vec{q}} V_{\vec{q}} X_{1,\uparrow:0} c_{\vec{q},\uparrow} \left(E - \mathcal{H}_0\right)^{-1} \sum_{\vec{q}'} V^*_{\vec{q}'} c^\dagger_{\vec{q}'\uparrow} X_{0:1,\uparrow}. \tag{4.24}$$

With the help of Eq. (4.23) and applying the same simplifications following Eq. (4.6), where $[\mathcal{H}_0, X_{0:1,\sigma}] = -\epsilon_c X_{0:1,\sigma}$ has to be used, this can be evaluated to

$$\frac{-\rho_0 \delta D |V|^2}{D - \epsilon_c} X_{1,\uparrow:1,\uparrow}. \tag{4.25}$$

Here one also has to avail oneself of the contraction $X_{1,\uparrow:0} X_{0:1,\uparrow} = X_{1,\uparrow:1,\uparrow}$. Furthermore the assumption has been made that the hybridization does not depend on the wavevector, $V_{\vec{q}} = V$. Diagram b) results in the same correction, but with the opposite spin direction,

$$\frac{-\rho_0 \delta D |V|^2}{D - \epsilon_c} X_{1,\downarrow:1,\downarrow}. \tag{4.26}$$

The two terms (4.25) and (4.26) can be interpreted as a correction to the energy E_1 of the singly occupied dot which results from second order virtual processes involving excitations at the upper band edge. Thus it can be absorbed by renormalizing the energy E_1. Another contribution to E_1 arises from processes illustrated in diagrams g) and h), resulting from virtual excitations of holes at the lower band edge. The other diagrams correspond to corrections which include the operators $X_{0:0}$ and $X_{2:2}$, i. e. they can be absorbed by renormalizing the energies E_0 or E_2 respectively. All these contributions are listed in Section A.2.3. Collecting all terms, we obtain for the renormalized energies

$$\begin{aligned} E_0' &= E_0 - \frac{2\Delta \delta D}{\pi} \frac{1}{D + \epsilon_c}, \\ E_1' &= E_1 - \frac{\Delta \delta D}{\pi} \left(\frac{1}{D - \epsilon_c} + \frac{1}{D + \epsilon_c + U_c} \right), \\ E_2' &= E_2 - \frac{2\Delta \delta D}{\pi} \frac{1}{D - \epsilon_c - U_c}, \end{aligned} \tag{4.27}$$

with the level width $\Delta \equiv \pi \rho_0 |V|^2$. As $\epsilon_c = E_1 - E_0$ and $U_c = E_2 - 2E_1 + E_0$, we can also express the renormalization by an effective Anderson Hamiltonian with renormalized

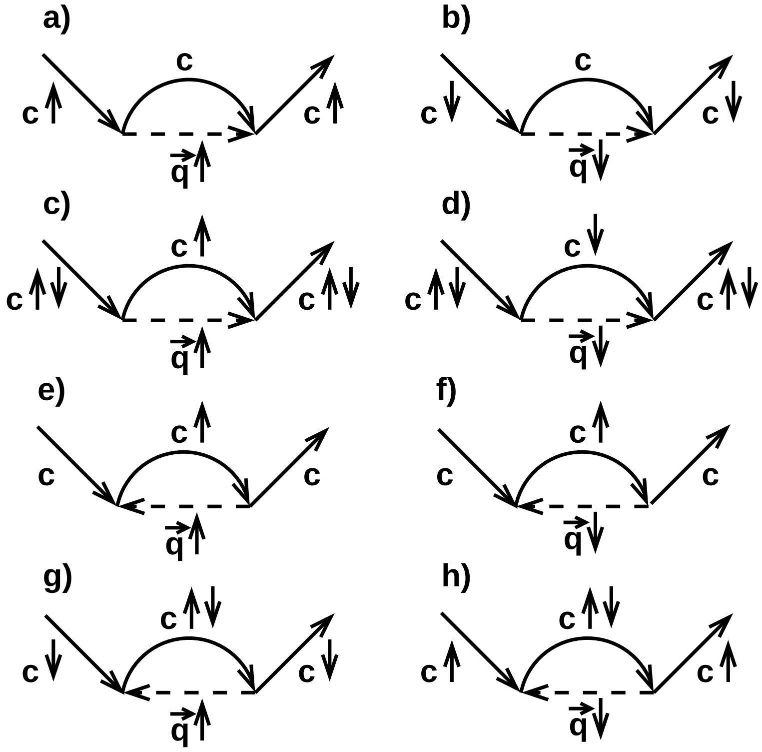

Figure 4.4: Illustration for the second order processes used in Poor Man's Scaling for the Anderson model. In contrast to the Kondo model, the Anderson model allows for charge fluctuations on the local level. Here fluctuations are depicted, which involve intermediate states with excitations at the upper or lower band edge. In contrast to the diagrams in Section 4.1, cf. Fig. 4.2, the dashed baseline illustrates the conduction electron at the upper band edge (upper four panels) or the conduction hole at the lower band edge (lower four panels), respectively. The solid lines depict the state of the local level, where 'c' stands for local conduction band level. The plain letter 'c' without arrows represents the empty local level. In the upper four panels an electron on the local level is scattered to the upper band edge and back. In the lower four panels an electron from the lower band edge is scattered into the local level and back, thereby creating an intermediate state with an hole at the lower band edge.

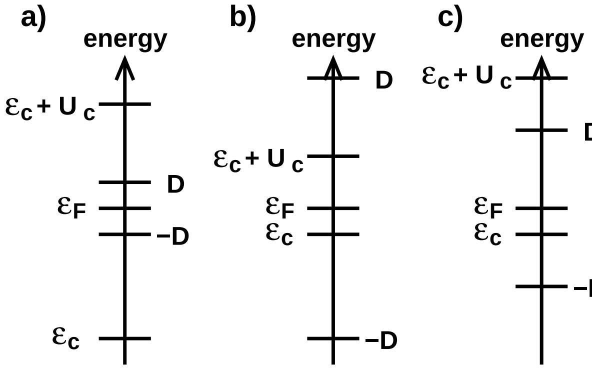

Figure 4.5: Three parameter regimes of the Anderson model. In the situation shown in panel a), the Anderson model can be transformed to the Kondo model by the Schrieffer-Wolff transformation and the scaling for the Kondo model can be applied. For the case demonstrated in panel b), there is no significant renormalization of the parameters until D is decreased to a size comparable with the order ϵ_c. In panel c), scaling can be applied until D reaches the order $\tilde{\epsilon_c}$. Then the Schrieffer-Wolff transformation can be applied again.

parameters, $\epsilon_c \to \epsilon_c + \delta\epsilon_c$ and $U_c \to U + \delta U_c$, with

$$\begin{aligned}\delta\epsilon_c &= \frac{\Delta\delta D}{\pi}\left(\frac{2}{D+\epsilon_c} - \frac{1}{D-\epsilon_c} - \frac{1}{D+\epsilon_c+U_c}\right),\\ \delta U_c &= \frac{2\Delta\delta D}{\pi}\left(\frac{1}{D-\epsilon_c} - \frac{1}{D+\epsilon_c} + \frac{1}{D+\epsilon_c+U_c} - \frac{1}{D-\epsilon_c-U_c}\right).\end{aligned} \tag{4.28}$$

Obviously we have a large parameter space. We will now look closer at three special cases, shown in Fig. 4.5. If $\epsilon_c \ll -D$ and $\epsilon_c + U_c \gg D$, see panel a), then the local level will be exactly singly occupied. In this case, the second order scattering processes to the band edges can only cause virtual charge fluctuations, since , they cannot cause real charge fluctuations of the impurity. As explained in Section 3.1, in this regime we can transform the Anderson model to the Kondo model by the Schrieffer-Wolff transformation. If the transformation is carried out, one gets an expression for the coupling parameter J of the Kondo model as a function of the parameters of the Anderson model, see [2],

$$J = |V|^2\left(\frac{1}{\epsilon_c+U_c} - \frac{1}{\epsilon_c}\right) > 0, \tag{4.29}$$

which gives the anti-ferromagnetic isotropic Kondo model. Thus the results of the previous section can be used. If Eq. (4.29) is plugged in (4.20), one finds

$$k_B T_K \sim D\left(\frac{\Delta U_c}{|\epsilon_c||\epsilon_c+U_c|}\right)^{1/2} e^{\pi\epsilon_c(\epsilon_c+U_c)/2\Delta U_c}. \tag{4.30}$$

Let us next consider the regime $|\epsilon_c|, |\epsilon_c + U_c| \ll D$, see panel b) of Fig. 4.5. In this case Eq. (4.28) gives $\delta\epsilon_c \sim 0$ and $\delta U_c \sim 0$, i. e. there is no significant renormalization. Thus the scaling can be continued until D reaches a value $\tilde{D} \sim \max(|\epsilon_c|, |\epsilon_c + \mathrm{U_c}|)$.

The situation $\epsilon_c + U_c \gg D \gg |\epsilon_c|$ is depicted in panel c). In this case the scaling equation (4.28) for ϵ_c is approximately given by

$$\frac{d\epsilon_c}{d\ln D} = -\frac{\Delta}{\pi}. \tag{4.31}$$

Up to second order, there is no renormalization of the hybridization matrix element $V_{\vec{k}}$. If $\mathcal{H}_{00}$ and $\mathcal{H}_{22}$ are not approximated by $\mathcal{H}_0$ but expanded in powers of V, one can create higher order terms leading to a renormalization of V. The lowest order corrections to V are of order $\delta V = O\left(\frac{\Delta}{D^2}\right)$, such that $\frac{d\Delta}{d\ln D} = O\left(\frac{\Delta}{D}\right)$. Hence, for $\Delta \ll D$, Δ is a scaling invariant. Therefore, Δ can be regarded as a constant in Eq. (4.31) and we can integrate Eq. (4.31) leading to $\epsilon_c + \frac{\Delta}{\pi}\ln D = \text{const.}$ which can be reformulated as

$$\epsilon_c + \frac{\Delta}{\pi}\ln\left(\frac{\pi D}{2\Delta}\right) \equiv \epsilon_c^*. \tag{4.32}$$

We have found two scaling invariants ϵ_c^* and Δ. Following the same argumentation conducted in the previous section, we can write all observables as universal function of T/Δ and T/ϵ_c^*. For instance, the impurity susceptibility can be written as $\chi_{imp} = \chi_0 f_\chi\left(T/\Delta, T/\epsilon_c^*\right)$, with a universal function f_χ. More information about scaling for the Anderson model can be found in [17].

4.3 Scaling for extended Anderson model

In this section the scaling method will be applied to the generalized Anderson Model of Section 3.2. It will turn out that this is a rather easy task, because it is possible to map the generalized model back to the Anderson model. After the mapping the results of the previous section can be used. First, the mapping will be explained.

Inspecting the generalized Hamiltonian, see Section 3.2, we see that $[\mathcal{H}, \hat{n}_{v,\sigma}] = 0$, i. e. the number of electrons on the local valence band level is conserved. Therefore the operators $\hat{n}_{v,\sigma}$ can be replaced by the numbers $n_{v,\sigma} = 0, 1$ and the Hamiltonian can be written in the following way,

$$\begin{aligned}\mathcal{H} \; = \; & \sum_\sigma \tilde{\epsilon}_c \hat{n}_{c,\sigma} + U_c \hat{n}_{c,\uparrow}\hat{n}_{c,\downarrow} \\ & + \sum_\sigma \epsilon_v n_{v,\sigma} + U_v\left(1 - n_{v,\uparrow}\right)\left(1 - n_{v,\downarrow}\right) \\ & + \mathcal{H}_{\text{lead}} + \mathcal{H}_{\text{coupling}}.\end{aligned} \tag{4.33}$$

If we disregard the second line, since it just represents a constant term, we see that we recovered the Anderson model, yet with a shifted local level with energy

$$\tilde{\epsilon}_c \equiv \sum_\sigma \left(\epsilon_c - U_{\text{exc}} \sum_\nu (1 - n_{v,\nu}) \right). \tag{4.34}$$

For this Hamiltonian, the scaling method of the previous section can be applied. For the Kondo temperature we obtain from Eq. (4.30),

$$k_B T_K \sim D \left(\frac{\Delta U_c}{|\tilde{\epsilon}_c||\tilde{\epsilon}_c + U_c|} \right)^{1/2} e^{\pi \tilde{\epsilon_c}(\tilde{\epsilon_c} + U_c)/2\Delta U_c}, \tag{4.35}$$

where we have just replaced ϵ_c by $\tilde{\epsilon}_c$.

The commutator $[\mathcal{H}, \hat{n}_{v,\sigma}] = 0$ follows from the fact that the Hamiltonian is diagonal in the states of the local valence band level, i. e. it can be written as

$$\begin{array}{cc} \begin{array}{cccc} |0\rangle_v & |\uparrow\rangle_v & |\downarrow\rangle_v & |\uparrow\downarrow\rangle_v \end{array} & \\ \left(\begin{array}{cccc} -\sum_\sigma 2U_{exc}\hat{n}_{c,\sigma} + U_v & 0 & 0 & 0 \\ 0 & -\sum_\sigma U_{exc}\hat{n}_{c,\sigma} + \epsilon_v & 0 & 0 \\ 0 & 0 & -\sum_\sigma U_{exc}\hat{n}_{c,\sigma} + \epsilon_v & 0 \\ 0 & 0 & 0 & 2\epsilon_v \end{array} \right) & \begin{array}{c} |0\rangle_v \\ |\uparrow\rangle_v \\ |\downarrow\rangle_v \\ |\uparrow\downarrow\rangle_v \end{array} \end{array}, \tag{4.36}$$

where $\sum_\sigma \epsilon_c \hat{n}_{c,\sigma} + U_c \hat{n}_{c,\uparrow} \hat{n}_{c,\downarrow} + \mathcal{H}_{\text{lead}} + \mathcal{H}_{\text{coupling}}$ has been left out at each one of the diagonal elements. Essentially each diagonal element represents one Hamiltonian of the form (4.33), with different $\tilde{\epsilon}_c$. The bandgap is by far the largest energy scale involved (order of 1 eV) and therefore the ground-state of the system will always be a state with no holes, which can be found in the block at the lower right, let's call it the fourth block. In the case of absorption the initial state will be the ground state, and we will look at transitions from the fourth block to the second or third block, as one hole is created. Thus we see that two different Kondo temperatures are involved in this process. The first one is the Kondo temperature of the fourth block, which is independent of U_{exc} and is given by Eq. (4.35) with $\tilde{\epsilon}_c = \epsilon_c$. The second one is the Kondo temperature of the second and third block, which is again given by Eq. (4.35), but with $\tilde{\epsilon_c} = \epsilon_c - U_{exc}$.

Chapter 5

The Numerical Renormalization Group

In this chapter the central method of this thesis, the numerical renormalization group (NRG), will be introduced. The NRG has been applied to the extended Anderson Model of Section 3.2 to calculate the absorption spectrum via the ansatz presented in Section 3.3. The intention of this chapter is to explain how the NRG works in principle (Section 5.1), and to give a rough idea of how the usual NRG method was adopted to the extended Anderson model to calculate the absorption function (Section 5.2). Extensive information about the NRG can be found in [4], where the NRG is applied to the Kondo model.

5.1 The idea behind the NRG

This section is closely related to [18], where the NRG is applied to the Anderson model, cf. Eq. (3.1). The aim of this section is to introduce a renormalization group transformation of Hamiltonians $\mathcal{H}_N$, where the Anderson Hamiltonian is given by $\mathcal{H}_{\text{Anderson}} = \lim_{N\to\infty} c\mathcal{H}_N$. The prefactor c will be derived at the end of the section. This renormalization group transformation will lead to a recursion relation which can be solved numerically by iteration.

We will start by rewriting the Anderson Hamiltonian, Eq. (3.1). It can be written as

$$\begin{aligned}\mathcal{H}_{\text{Anderson}} &= -\frac{1}{2}U_c + \sum_{\sigma=\uparrow,\downarrow}\left(\epsilon_c + \frac{1}{2}U_c\right) c_\sigma^\dagger c_\sigma + \frac{1}{2}U_c\left(\hat{n}_{c,\uparrow} + \hat{n}_{c,\downarrow} - 1\right)^2 \\ &\quad + \sum_{\vec{k},\sigma} \epsilon_{\vec{k}} l_{\vec{k}\sigma}^\dagger l_{\vec{k}\sigma} \\ &\quad + \sum_{\vec{k},\sigma}\left(V_{\vec{k}c} l_{\vec{k}\sigma}^\dagger c_\sigma + V_{\vec{k}c}^* c_\sigma^\dagger l_{\vec{k}\sigma}\right), \qquad (5.1)\end{aligned}$$

which can easily be verified by expanding the last term in the first line of (5.1). We will now simplify the Hamiltonian (5.1) by making several assumptions. We will again set the Fermi energy equal to zero, $\epsilon_F = 0$. As in the previous chapters, we will assume that the density of states of the conduction band is equal to a constant ρ_0 between two band edges $-D$ and D and zero otherwise. As before, we will assume that $V_{\vec{k}c}$ is independent of $\vec{k}$, $V_{\vec{k}c} = V_c$. This implies that the impurity couples only to s-waves, if the conduction band states are expanded in a basis of spherical waves around the impurity. We can therefore neglect higher angular momentum states since they are not affected by the presence of the impurity. Furthermore we will assume the conduction band to be isotropic, i. e. the dispersion relation depends only on $|\vec{k}|$, $\epsilon_{\vec{k}} = \epsilon_{|\vec{k}|}$. To simplify the Hamiltonian further, the energies are measured relative to the band edge D. Therefore the variable $k \equiv \epsilon/D$ is defined, which has the advantage of being dimensionless. One should not confuse k with the wavevector $\vec{k}$. A detailed calculation in [18], with Eq. (5.1) as starting point, shows that with the help of these simplifications the Hamiltonian can be written in a continuous manner as

$$\begin{aligned}\mathcal{H}_{\text{Anderson}} &= D\Bigg(\int_{-1}^{1} k \sum_{\sigma=\uparrow,\downarrow} a^{\dagger}_{k\sigma} a_{k\sigma} dk \\ &\quad + \frac{1}{D}\left(\epsilon_c + \frac{1}{2}U_c\right) \sum_{\sigma=\uparrow,\downarrow} c^{\dagger}_{\sigma} c_{\sigma} + \frac{1}{2}\frac{U_c}{D}\left(\sum_{\sigma=\uparrow,\downarrow} c^{\dagger}_{\sigma} c_{\sigma} - 1\right)^2 \\ &\quad + \left(\frac{\Gamma}{\pi D}\right)^{1/2} \int_{-1}^{1} dk \sum_{\sigma=\uparrow,\downarrow} \left(a^{\dagger}_{k\sigma} c_{\sigma} + c^{\dagger}_{\sigma} a_{k\sigma}\right)\Bigg) . \qquad (5.2)\end{aligned}$$

Here $\Gamma \equiv \pi \rho_0 V_c^2$. The operator $a_{k\sigma}$ is defined by $a_{k\sigma} \equiv \sqrt{D} a_{\epsilon\sigma}$ ($\epsilon = kD$), where $a^{\dagger}_{\epsilon\sigma}(a_{\epsilon\sigma})$ creates (destroys) a s-wave electron with energy ϵ and spin σ. The operators $a_{k\sigma}$ fulfill the anticommutation relation $\left[a^{\dagger}_{k\sigma}, a_{k'\mu}\right]_{+} = \delta_{\sigma,\mu}\delta(k - k')$. The advantage of the form (5.2) is that the Hamiltonian only contains the dimensionless parameters (ϵ_c/D), (U_c/D) and (Γ/D), i. e. all parameters are given in units of the bandwidth D.

The difficulties in solving the Anderson Hamiltonian, i. e. finding its eigenstates and eigenenergies, result from the conduction band rather than from the impurity. What lies at the heart of the problem is the fact that the Anderson model represents a true many-body problem for the following reason. The conduction band by itself can be described by quasi particles. However, if the impurity is present, the conduction band electron can scatter on it. The Kondo regime, $\epsilon_c < 0 < \epsilon_c + U_c$, is particular important here. In this case the impurity contains one electron and thus has a spin. Suppose that it is in the spin down state. Then spin-flip scattering can take place, where an conduction electron with spin up is scattered on the impurity and thereby the spins of both the impurity electron and the conduction band electron are flipped. Afterwards the impurity is in the spin up state. Consequently, no other spin-flip process featuring a conduction electron with spin up can take place. Therefore, the conduction band electrons cannot be treated independently of the impurity.

Another central aspect of the problem is that all energy scales are important, which is already visible in the Poor Man's Scaling method, see Chapter 4. We have seen there that

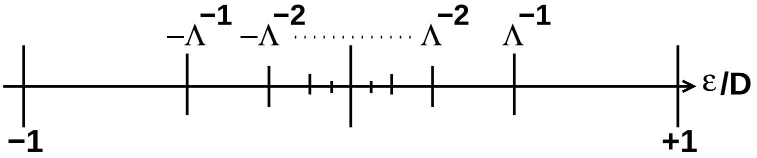

Figure 5.1: Logarithmic discretization of the conduction band. The Fermi energy is at zero and the band edges are at $k \equiv \epsilon/D = -1$ and 1, respectively.

scattering processes including electrons of the entire energy range of the conduction band are important, i. e. we have correlations over many orders of wavelength. The key to the solution of the problem lies in a logarithmic discretization of the conduction band, see Fig. 5.1. This procedure will first be explained and motivated afterwards. In the discretization a parameter $\Lambda > 1$ is introduced and the band width $[-1, +1]$ is divided into intervals with successive exponentially decreasing lengths and upper bound, where the nth interval extends from $\Lambda^{-(n+1)}$ to Λ^{-n} for positive energies and accordingly from $-\Lambda^{-n}$ to $-\Lambda^{-(n+1)}$ for negative energies. Now a set of functions can be defined by setting up a Fourier series in each of the intervals,

$$\psi_{np}^{\pm}(k) \equiv \begin{cases} \frac{\Lambda^{n/2}}{(1-\Lambda^{-1})^{1/2}} e^{\pm i\omega_n pk} \text{ if } \Lambda^{-(\mathrm{n}+1)} < \pm \mathrm{k} < \Lambda^{-\mathrm{n}}, \\ 0 \text{ if } \pm \mathrm{k} \text{ is outside the interval } \left[\Lambda^{-(\mathrm{n}+1)}, \Lambda^{-\mathrm{n}}\right]. \end{cases} \tag{5.3}$$

Here $n \in \mathbf{N}_0$ labels the interval and p is the Fourier harmonic index, where $p \in \mathbf{Z}$. The superscript indicates if the function is defined for positive energies (+) or negative energies (-). The Fourier frequency ω_n for the nth interval is given by

$$\omega_n \equiv \frac{2\pi}{\Lambda^{-n} - \Lambda^{-(n+1)}} = \frac{2\pi\Lambda^n}{1 - \Lambda^{-n}}. \tag{5.4}$$

Since the functions $\psi_{np}^{\pm}$ define a complete set of orthonormal functions, we can expand the operators $a_{k\sigma}$ in this basis,

$$a_{k\sigma} = \sum_{np} \left[a_{np\sigma} \psi_{np}^{+}(k) + b_{np\sigma} \psi_{np}^{-}(k) \right], \tag{5.5}$$

where

$$a_{np\sigma} = \int_{-1}^{+1} dk \left[\psi_{np}^{+}(k)\right]^* a_{k\sigma}; \quad b_{np\sigma} = \int_{-1}^{+1} dk \left[\psi_{np}^{-}(k)\right]^* a_{k\sigma}. \tag{5.6}$$

The operators $a_{np\sigma}$ and $b_{np\sigma}$ form a complete set of independent and discrete electron operators obeying standard anti-commutation rules, $\left[a_{np\sigma}, a^{\dagger}_{n'p'\sigma'}\right]_+ = \delta_{n,n'}\delta_{p,p'}\delta_{\sigma,\sigma'}$. The Hamiltonian (5.2) can thus be written in the basis of the operators $a_{np\sigma}$ and $b_{np\sigma}$ using the relations

$$\begin{aligned}
\int_{-1}^{+1} k \sum_{\sigma=\uparrow,\downarrow} a_{k\sigma}^{\dagger} a_{k\sigma} dk &= \frac{1}{2}\left(1+\Lambda^{-1}\right) \sum_{n,p,\sigma} \Lambda^{-n}\left(a_{np\sigma}^{\dagger} a_{np\sigma}-b_{np\sigma}^{\dagger} b_{np\sigma}\right) \\
&\quad +\frac{1-\Lambda^{-1}}{2\pi i} \sum_{n,p\neq p',\sigma}\left(a_{np\sigma}^{\dagger} a_{np'\sigma}-b_{np\sigma}^{\dagger} b_{np'\sigma}\right) \exp\left(\frac{2\pi i(p'-p)}{1-\Lambda^{-1}}\right), \\
\int_{-1}^{1} \sum_{\sigma=\uparrow,\downarrow} a_{k\sigma} dk &= \left(1-\Lambda^{-1}\right)^{1/2} \sum_{n,\sigma} \Lambda^{-n/2}\left(a_{n0\sigma}+b_{n0\sigma}\right), \qquad (5.7)
\end{aligned}$$

which can be verified by a lengthy but straightforward calculation. Inserting Eq. (5.7) into Eq. (5.2), we see that the impurity couples directly only to the operators $a_{n0\sigma}$ and $b_{n0\sigma}$. The operators $a_{np\sigma}$ and $b_{np\sigma}$ couple only indirectly to the impurity, via the second term in Eq. (5.7). Since the factor $(1-\Lambda^{-1})/2\pi$ in this term is small for Λ close to one, we will neglect all terms containing operators $a_{np\sigma}$ and $b_{np\sigma}$ for $p \neq 0$. This is a surprisingly good approximation even for Λ as large as 3, see [4]. If we drop the subscript '0' from the operators $a_{n0\sigma}$ and $b_{n0\sigma}$ and define the operator

$$f_{0\sigma} \equiv \left[\frac{1}{2}\left(1-\Lambda^{-1}\right)\right]^{1/2} \sum_{n=0}^{\infty} \Lambda^{-n/2} \sum_{\sigma}\left(a_{n\sigma}+b_{n\sigma}\right)=\frac{1}{\sqrt{2}} \int_{-1}^{1} dk \sum_{\sigma} a_{k\sigma}, \qquad (5.8)$$

with $\left[f_{0\sigma}, f_{0\mu}^{\dagger}\right]=\delta_{\sigma,\mu}$, we can write the Hamiltonian (5.2) as

$$\begin{aligned}
\frac{\mathcal{H}_{\text{Anderson}}}{D} &= \frac{1}{2}\left(1+\Lambda^{-1}\right) \sum_{n=0}^{\infty} \Lambda^{-n} \sum_{\sigma}\left(a_{n\sigma}^{\dagger} a_{n\sigma}-b_{n\sigma}^{\dagger} b_{n\sigma}\right) \\
&\quad +\frac{1}{D}\left(\epsilon_c+\frac{1}{2} U_c\right) \sum_{\sigma} c_{\sigma}^{\dagger} c_{\sigma}+\frac{1}{2} \frac{U_c}{D}\left(\sum_{\sigma} c_{\sigma}^{\dagger} c_{\sigma}-1\right)^2 \\
&\quad +\left(\frac{2\Gamma}{\pi D}\right)^{1/2} \sum_{\sigma}\left(f_{0\sigma}^{\dagger} c_{\sigma}+c_{\sigma}^{\dagger} f_{0\sigma}\right). \qquad (5.9)
\end{aligned}$$

The motivation for the logarithmic discretization is the following. Let's consider an instructive example, see [4]. Suppose one has a Hamiltonian $\mathcal{H} = \mathcal{H}_0 + \mathcal{H}_1$, where the level spacings of $\mathcal{H}_0$ and of $\mathcal{H}_1$ are of order ~ 1 and ~ 0.01, respectively, i. e. $\mathcal{H}_1$ can be understood as a perturbation to $\mathcal{H}_0$. Furthermore we assume that the Hamiltonian $\mathcal{H}_0$ is nontrivial and can only be solved numerically with an accuracy of 5%, say. Finally, suppose that $\mathcal{H}_0$ has two degenerate ground states consisting of the states $|\Psi_0\rangle$ and $|\Psi_1\rangle$. We know that the perturbation will split up the degeneracy. One way to attack the problem is to first diagonalize $\mathcal{H}_0$ and then calculate the contribution of $\mathcal{H}_1$. The matrix elements in the perturbation theory, $\langle\Psi_0|\mathcal{H}_1|\Psi_0\rangle$, $\langle\Psi_0|\mathcal{H}_1|\Psi_1\rangle$, etc., then can be calculated with the accuracy of 5%. Therefore, as the eigenenergies of $\mathcal{H}_1$ are of order 0.01, the splitting can be calculated with an accuracy of about 0.0005. Another way of attacking the problem is to diagonalize $\mathcal{H}_0 + \mathcal{H}_1$ directly. However, this is obviously a bad choice, since in this case all energies are calculated with an accuracy of about 0.05 and hence one does not get reasonable results for the energy splitting which is of order 0.01. The same argument holds if another term $\mathcal{H}_2$ is added to the Hamiltonian, where the level spacing of $\mathcal{H}_2$ is of order ~ 0.0001. Given this case, one just gets reasonable results if one first diagonalizes $\mathcal{H}_0$, then treats $\mathcal{H}_1$ as a perturbation to $\mathcal{H}_0$ and finally treats $\mathcal{H}_2$ as a perturbation to $\mathcal{H}_1$.

The problem we are facing is even more challenging. Considering the conduction band, we have operators $a_{k,\sigma}$ with all energies $k \leq 1$ of all orders of magnitude, e. g. we have energies $k \sim 1$, $k \sim 0.01$, $k \sim 0.0001$, $k \sim 0.000001$, etc. The operators $a_{k,\sigma}$ with $k \sim 1$ create states with level splitting of the order ~ 1. As in the abovementioned example, these states can be split, for instance, by operators $a_{k,\sigma}$ with $k \sim 0.01$, etc. We are interested in level spacings down to the order of $k_B T$. Since we are interested in the limit $T \to 0$, $k_B T$ would be arbitrary small. Fortunately it turns out that the renormalization group transformation we are going to derive, which will start by considering large energies and then going successively to smaller energies, will reach a fixed point when the energy decreases below a certain crossover scale, the Kondo scale. However, we see that we have to consider energies of several orders of magnitude. As the scaling method, Chapter 4, teaches us, we have to take all these energies into account properly at the same time. The analogy between our problem and the example is certainly imperfect. In our case there is no obvious separation into parts $\mathcal{H}_0$, $\mathcal{H}_1$, etc. The logarithmic discretization separates the conduction band and thereby the Hamiltonian in parts with different energies, depending on the value of the parameter Λ. There is no obvious choice for Λ, such as $\Lambda = 2$ or $\Lambda = 3$, neither doet there exist a strict justification for the logarithmic discretization procedure. The ultimate justification is that it successfully solves the problem. Furthermore we can not use perturbation theory to calculate the contribution of the different parts. The renormalization group transformation will be set up to overcome this problem.

To finally derive the renormalization group transformation, another transformation is necessary. Looking at the Hamiltonian (5.9), we see that the impurity couples directly only to the operator $f_{0\sigma}$, which reflects the fact that the impurity is localized, see [18]. We will now again follow [18] and make a unitary transformation from the set of operators $\{a_{n\sigma}, b_{n,\sigma}\}$ to a new orthonormal set $\{f_{n\sigma}\}$, with the constraint that $f_{0\sigma}$ is still given by Eq. (5.8). Since the first term in the Hamiltonian (5.9), which represents the conduction band, is diagonal in the operators $\{a_{n\sigma}, b_{n,\sigma}\}$, the transformation will necessarily lead to operators $\{f_{n\sigma}\}$ that are coupled to each other. We will deliberately choose a transformation which leads to nearest neighbor coupling, i. e. the operator $f_{n,\sigma}$ will couple directly only to the operators $f_{n-1,\sigma}$ and $f_{n+1,\sigma}$. A geometric interpretation of these operators will be given further below. The transformation is carried out in [4], here we will just quote the result

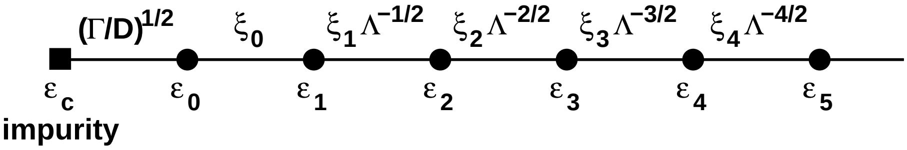

Figure 5.2: Illustration of the Hamiltonian (5.10) as a semi-infinite chain with nearest neighbor hopping. At the end of the chain is the local level with energy ϵ_c of the impurity. It is coupled to the first site, the f_0-site, with a coupling strength proportional to $(\Gamma/D)^{1/2}$. The f_0-site represents the state created by $f^\dagger_{0\sigma}$. It is coupled to the f_1-site, the f_1-site is coupled to the f_2-site, etc. The strength of the coupling between the neighbor n and $n+1$ falls of exponentially with $\Lambda^{-n/2}\xi_n$. The energies $\epsilon_n = 0$, see [18].

for the Hamiltonian stated in [18],

$$\begin{aligned}\mathcal{H}_{\text{Anderson}} &= \frac{1}{2}\left(1-\Lambda^{-1}\right)\sum_{n=0}^{\infty}\Lambda^{-n/2}\xi_n\sum_\sigma\left[f^\dagger_{n\sigma}f_{(n+1)\sigma}+f^\dagger_{(n+1)\sigma}f_{n\sigma}\right]\\ &\quad+\frac{1}{D}\left(\epsilon_c+\frac{1}{2}U_c\right)\sum_\sigma c^\dagger_\sigma c_\sigma+\frac{1}{2}\frac{U_c}{D}\left(\sum_\sigma c^\dagger_\sigma c_\sigma-1\right)^2\\ &\quad+\left(\frac{2\Gamma}{\pi D}\right)^{1/2}\sum_\sigma\left(f^\dagger_{0\sigma}c_\sigma+c^\dagger_\sigma f_{0\sigma}\right), \qquad (5.10)\end{aligned}$$

where

$$\xi_n = \left(1-\Lambda^{-n-1}\right)\left(1-\Lambda^{-2n-1}\right)^{-1/2}\left(1-\Lambda^{-2n-3}\right)^{-1/2}. \qquad (5.11)$$

For $n \to \infty$, $\xi_n \to 1$. The Hamiltonian can be visualized by a semi-infinite chain, see Fig. 5.2. At the one end of the chain there is the local impurity level with energy ϵ_c. It is coupled to the first site of the chain, representing the state created by $f^\dagger_{0\sigma}$, through a coupling with a strength proportional to $(\Gamma/D)^{1/2}$. The nearest neighbor coupling connects the f_0-site with the f_1-site, the f_1-site with the f_2-site, etc. The coupling strength between the sites n and $n+1$ is proportional to $\Lambda^{-n/2}\xi_n$. For large n it decreases as $\Lambda^{-n/2}$, since $\xi_n \to 1$. The energies $\epsilon_n = 0$, see [18].

The geometrical interpretation of the operators $f_{n\sigma}$ is depicted in Fig. 5.3, see [18]. Since the mean energies $\epsilon_n = 0$, which is the Fermi energy, one can conclude that the operators $f_{n\sigma}$ contain equal amounts of positive and negative energy electron operators. The single-particle states $|f_n\rangle$ created by $f^\dagger_{n\sigma}$ are all peaked at the impurity site and have a spread in energy $\sim \Lambda^{-n/2}$, which is the strength of the coupling in (5.10), cf. [18]. Thus $|f_0\rangle$ has the biggest spread in energy and consequently is the most localized wavefunction, Fig. 5.3.

To derive the renormalization group transformation, one now defines a set of Hamilto-

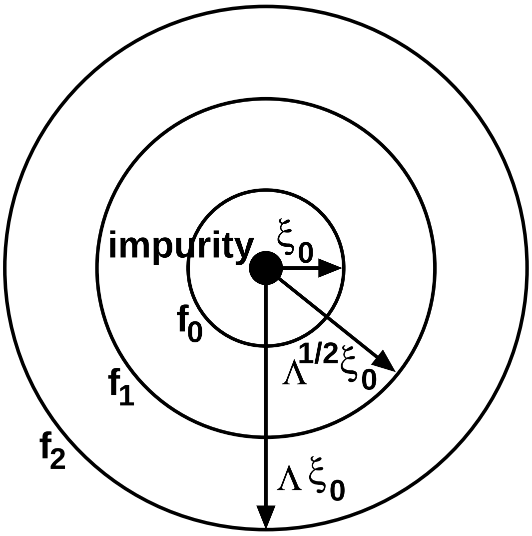

Figure 5.3: The local extent of the single-particle wavefunctions $|f_n\rangle$, which are created by the operators $f^\dagger_{n\sigma}$, can be depicted as spherical shells around the impurity. Since the mean energy of the wavefunctions is the Fermi energy, their mean wavenumber is $\sim k_F$. The wavefunction $|f_0\rangle$ is the most localized wavefunction, because it has the biggest spread in energy ~ 1. It has an extend of $\zeta_0 \sim 1/k_F$. The extend of $|f_n\rangle$ is $\sim \zeta_0\Lambda^{n/2}$. The impurity is coupled directly only to $|f_0\rangle$.

nians, $\mathcal{H}_N$, as follows,

$$\begin{aligned}\mathcal{H}_N \equiv \Lambda^{(N-1)/2} \Bigg[\sum_{n=0}^{N-1} \Lambda^{-n/2} \xi_n \sum_{\sigma} \left(f^{\dagger}_{n\sigma} f_{(n+1)\sigma} + f^{\dagger}_{(n+1)\sigma} f_{n\sigma} \right) \\ + \tilde{\delta}_c \sum_{\sigma} c^{\dagger}_{\sigma} c_{\sigma} + \tilde{U}_c \left(\sum_{\sigma} c^{\dagger}_{\sigma} c_{\sigma} - 1 \right)^2 \\ + \tilde{\Gamma}^{1/2} \sum_{\sigma} \left(f^{\dagger}_{0\sigma} c_{\sigma} + c^{\dagger}_{\sigma} f_{0\sigma} \right) \Bigg], \end{aligned} \tag{5.12}$$

where the constants

$$\begin{aligned} \tilde{\delta}_c &\equiv \left(\frac{2}{1+\Lambda^{-1}} \right) \frac{1}{D} \left(\epsilon_c + \frac{1}{2} U_c \right) \equiv \tilde{\epsilon}_c + \tilde{U}_c, \\ \tilde{U}_c &\equiv \left(\frac{2}{1+\Lambda^{-1}} \right) \frac{U_c}{2D}, \\ \tilde{\Gamma} &\equiv \left(\frac{2}{1+\Lambda^{-1}} \right)^2 \frac{2\Gamma}{\pi D} = \left(\frac{2}{1+\Lambda^{-1}} \right)^2 \frac{2\rho_0 |V_c|^2}{D} \end{aligned} \tag{5.13}$$

have been defined for convenience. The originally Hamiltonian can be recovered by

$$\mathcal{H}_{\text{Anderson}} = \lim_{N\to\infty} \frac{1}{2} \left(1 + \Lambda^{-1} \right) D \Lambda^{-(N-1)/2} \mathcal{H}_N. \tag{5.14}$$

Here the factor $\Lambda^{(N-1)/2}$ in Eq. (5.12) has been introduced in order to make the lowest energy scale in $\mathcal{H}_N$, which is the coefficient of $f^{\dagger}_{N-1\sigma} f_{N\sigma} + f^{\dagger}_{N\sigma} f_{N-1\sigma}$, of order ~ 1. From the definition of $\mathcal{H}_N$, the central recursion relation of the NRG method can be defined,

$$\mathcal{H}_{N+1} = \Lambda^{1/2} \mathcal{H}_N + \xi_N \sum_{\sigma} \left(f^{\dagger}_{N\sigma} f_{N+1\sigma} + f^{\dagger}_{N+1\sigma} f_{N\sigma} \right). \tag{5.15}$$

With the help of this relation, a renormalization group transformation $\mathcal{H}_{N+1} = \mathcal{T}\left[\mathcal{H}_N\right]$ can be defined. The introduction of the set $\mathcal{H}_N$ and the recursion relation can be motivated with the example at the beginning of the section. There, we have seen that given a Hamiltonian $\mathcal{H} = \mathcal{H}_0 + \mathcal{H}_1 + \mathcal{H}_2$ (there is no relation between the $\mathcal{H}_N$ in the example and in the recursion relation), where the level spacing of $\mathcal{H}_n$ is by two orders of magnitude smaller than the level spacing of $\mathcal{H}_{n-1}$, see above, the best strategy is the following. We first diagonalize $\mathcal{H}_0$, then add the contribution of $\mathcal{H}_1$ by perturbation theory, then diagonalize $\mathcal{H} = \mathcal{H}_0 + \mathcal{H}_1$ and finally add $\mathcal{H}_2$ in the same way as $\mathcal{H}_1$. The purpose of defining the set $\mathcal{H}_N$ is that one can now make use of the same strategy to solve the Hamiltonian (5.9), except that one applies the recursion relation (5.15) instead of perturbation theory and that one has infinetly many contributions. One starts by diagonalizing $\mathcal{H}_1$, which contains the contributions of the impurity and the f_0-site, representing the largest energy scale of the problem. To obtain the subsequent Hamiltonians $\mathcal{H}_{N+1}$, one adds the successively smaller terms $\xi_N \left(f^\dagger_{N\sigma} f_{N+1\sigma} + f^\dagger_{N+1\sigma} f_{N\sigma} \right)$ of the f_{N+1}-site, where first the Hamiltonian $\mathcal{H}_N$ is diagonalized and then the f_{N+1}-terms are added in the basis of $\mathcal{H}_N$.

Except for special cases, e. g. $\Lambda = 1$, no analytical method is known to diagonalize the Hamiltonians $\mathcal{H}_N$. Thus numerically methods are used. To conclude this section, a rough idea will be given of how the algorithm works. As a starting point, one sets up the Hamiltonian $\mathcal{H}_1$. It is a 16x16 matrix, where the 16 basis states are product states of the f_0-site and the the local impurity level, $|\Psi_n\rangle_{N=1} = \{|0\rangle_0, |\uparrow\rangle_0, |\downarrow\rangle_0, |\uparrow\downarrow\rangle_0\} \otimes \{|0\rangle_c, |\uparrow\rangle_c, |\downarrow\rangle_c, |\uparrow\downarrow\rangle_c\}$, $n = 1, 2, 3, .., 16$, where '0' denotes the f_0-site states and 'c' the local impurity states. Then one numerically diagonalizes the Hamiltonian by a unitary transformation U, $U^T \mathcal{H}_1 U = \mathcal{H}_1^{\text{diag}}$, where $\mathcal{H}_1^{\text{diag}}$ has only entries at the principal axis, which are the eigenenergies.. All physical observables that one would like to compute are first set up in the basis $|\Psi_n\rangle_{N=1}$ and then are transformed into the new bases with the help of U. In the step $N = 2$, a new basis is set up by defining

$$\begin{aligned}
|1, \Psi_n\rangle_{N=2} &\equiv |0\rangle_1 \otimes |\Psi_n\rangle_{N=1}, \\
|2, \Psi_n\rangle_{N=2} &\equiv |\uparrow\rangle_1 \otimes |\Psi_n\rangle_{N=1}, \\
|3, \Psi_n\rangle_{N=2} &\equiv |\downarrow\rangle_1 \otimes |\Psi_n\rangle_{N=1}, \\
|4, \Psi_n\rangle_{N=2} &\equiv |\uparrow\downarrow\rangle_1 \otimes |\Psi_n\rangle_{N=1}, \qquad (5.16)
\end{aligned}$$

where '1' denotes the f_1-site states. In this new basis, the contributions of the f_1-site are added to build the Hamiltonian $\mathcal{H}_2$,

$$\mathcal{H}_2 = \begin{pmatrix} \Lambda^{1/2}\mathcal{H}_1^{\text{diag}} & \xi_1 f^\dagger_{1,\uparrow} & \xi_1 f^\dagger_{1,\downarrow} & 0 \\ \xi_1 f^\dagger_{1,\uparrow} & \Lambda^{1/2}\mathcal{H}_1^{\text{diag}} & 0 & \xi_1 f^\dagger_{1,\downarrow} \\ \xi_1 f^\dagger_{1,\downarrow} & 0 & \Lambda^{1/2}\mathcal{H}_1^{\text{diag}} & -\xi_1 f^\dagger_{1,\uparrow} \\ 0 & \xi_1 f^\dagger_{1,\downarrow} & -\xi_1 f^\dagger_{1,\uparrow} & \Lambda^{1/2}\mathcal{H}_1^{\text{diag}}. \end{pmatrix} \qquad (5.17)$$

The whole procedure can now be repeated. We see that for each iteration the basis has the 4-fold size of the basis of the iteration before. Soon a matrix size is reached that cannot be handled anymore by even large computer memories. Therefore, after a certain size is reached, the states are truncated after the diagonaliation procedure and one just keeps the lowest lying states, typically a number about 1000.

Further information can be found in [4], [18], [19], [20].

5.2 The NRG applied to the extended model

The intention of this section is to give a rough idea of how the NRG method was applied to the extended model of Section 3.2.

As explained in the previous section, the difficulties in solving the model result from the fact that that the local level with the conduction band is a many-body problem where all energy scales in the conduction band are important. Since we can make the same assumptions about the conduction band as above, we can closely follow the procedure

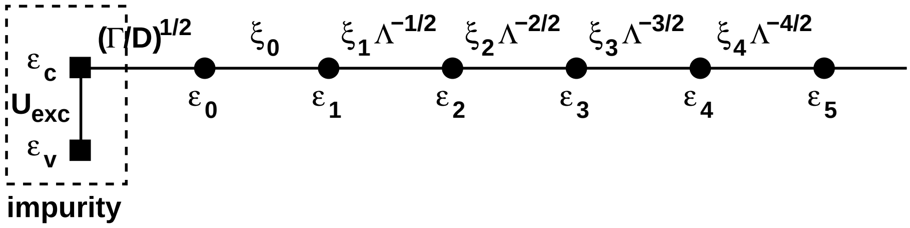

Figure 5.4: By following the transformations of Section 5.1, we can analogously map the extended Anderson Hamiltonian to a semi-infinite chain, cf. Fig. 5.2. However, the impurity, i. e. in our case the quantum dot, has a more complicated structure. As described in Section 3.2, here also a local valence band level is considered, which couples to the local conduction band level via an exciton binding energy with a strength proportional to U_{exc}.

of the usual NRG method. After the logarithmic discretization of the conduction band and the unitary transformation described above, we can map the extended model to a Hamiltonian which once again can be illustrated by a semi-infinite chain, Fig. 5.4, which should be compared to Fig. 5.2. As described in Section 3.2, the local valence band level with energy ϵ_v has been added to the quantum dot. It is coupled to the local conduction band level by the exciton binding energy where the strength of the coupling is proportional to U_{exc}. Essentially just the starting point, i. e. the Hamiltonian $\mathcal{H}_1$ of the usual NRG method has to be changed. It is now a 64x64 matrix, where the 64 basis states are product states of the two local levels and the f_0-site, $|\Psi_n\rangle_{N=1} = \{|0\rangle_0, |\uparrow\rangle_0, |\downarrow\rangle_0, |\uparrow\downarrow\rangle_0\} \otimes \{|0\rangle_c, |\uparrow\rangle_c, |\downarrow\rangle_c, |\uparrow\downarrow\rangle_c\} \otimes \{|0\rangle_v, |\uparrow\rangle_v, |\downarrow\rangle_v, |\uparrow\downarrow\rangle_v\}$, $n = 1, 2, 3, .., 64$. If the basis states have the following order,

$$
\begin{aligned}
|1\rangle &= |0\rangle_0 |0\rangle_c |0\rangle_v, \\
|2\rangle &= |\uparrow\rangle_0 |0\rangle_c |0\rangle_v, \\
|3\rangle &= |\downarrow\rangle_0 |0\rangle_c |0\rangle_v, \\
|4\rangle &= |\uparrow\downarrow\rangle_0 |0\rangle_c |0\rangle_v, \\
|5\rangle &= |0\rangle_0 |\uparrow\rangle_c |0\rangle_v, \\
|6\rangle &= |\uparrow\rangle_0 |\uparrow\rangle_c |0\rangle_v, \\
&\dots \\
|16\rangle &= |\uparrow\downarrow\rangle_0 |\uparrow\downarrow\rangle_c |0\rangle_v, \\
|17\rangle &= |0\rangle_0 |0\rangle_c |\uparrow\rangle_v, \\
|18\rangle &= |\uparrow\rangle_0 |0\rangle_c |\uparrow\rangle_v, \\
&\dots \\
|64\rangle &= |\uparrow\downarrow\rangle_0 |\uparrow\downarrow\rangle_c |\uparrow\downarrow\rangle_v,
\end{aligned}
\tag{5.18}
$$

then $\mathcal{H}_1$ has the following block-diagonal form, cf. Eq. (4.36),

$$\mathcal{H}_1 = \begin{array}{c} \begin{array}{cccc} |0\rangle_v & |\uparrow\rangle_v & |\downarrow\rangle_v & |\uparrow\downarrow\rangle_v \end{array} \\ \left(\begin{array}{cccc} \mathcal{H}_{|0\rangle,v} & 0 & 0 & 0 \\ 0 & \mathcal{H}_{|\uparrow\rangle,v} & 0 & 0 \\ 0 & 0 & \mathcal{H}_{|\downarrow\rangle,v} & 0 \\ 0 & 0 & 0 & \mathcal{H}_{|\uparrow\downarrow\rangle_v} \end{array} \right) \end{array}, \tag{5.19}$$

where

$$\begin{aligned} \mathcal{H}_{|0\rangle,v} &= \mathcal{H}_1' - \sum_\sigma 2U_{exc}\hat{n}_{c,\sigma} + U_v \\ \mathcal{H}_{|\uparrow\rangle,v} &= \mathcal{H}_1' - \sum_\sigma U_{exc}\hat{n}_{c,\sigma} + \epsilon_v \\ \mathcal{H}_{|\downarrow\rangle,v} &= \mathcal{H}_1' - \sum_\sigma U_{exc}\hat{n}_{c,\sigma} + \epsilon_v \\ \mathcal{H}_{|\uparrow\downarrow\rangle_v} &= \mathcal{H}_1' + 2\epsilon_v. \end{aligned} \tag{5.20}$$

The matrix $\mathcal{H}_1'$ is the starting point of the usual NRG process, which is explicitly given by the matrix

$$\begin{array}{cccc} |0\rangle_c & |\uparrow\rangle_c & |\downarrow\rangle_c & |\uparrow\downarrow\rangle_c \\ \begin{array}{cccc} |0\rangle_0 & |\uparrow\rangle_0 & |\downarrow\rangle_0 & |\uparrow\downarrow\rangle_0 \end{array} & \begin{array}{cccc} |0\rangle_0 & |\uparrow\rangle_0 & |\downarrow\rangle_0 & |\uparrow\downarrow\rangle_0 \end{array} & \begin{array}{cccc} |0\rangle_0 & |\uparrow\rangle_0 & |\downarrow\rangle_0 & |\uparrow\downarrow\rangle_0 \end{array} & \begin{array}{cccc} |0\rangle_0 & |\uparrow\rangle_0 & |\downarrow\rangle_0 & |\uparrow\downarrow\rangle_0 \end{array} \end{array}$$

$$\left(\begin{array}{cccc} 0 & \begin{matrix} 0 & 0 & 0 & 0 \\ \tilde{\Gamma}^{1/2} & 0 & 0 & 0 \\ 0 & 0 & 0 & 0 \\ 0 & 0 & -\tilde{\Gamma}^{1/2} & 0 \end{matrix} & \begin{matrix} 0 & 0 & 0 & 0 \\ 0 & 0 & 0 & 0 \\ \tilde{\Gamma}^{1/2} & 0 & 0 & 0 \\ 0 & \tilde{\Gamma}^{1/2} & 0 & 0 \end{matrix} & 0 \\ \begin{matrix} 0 & \tilde{\Gamma}^{1/2} & 0 & 0 \\ 0 & 0 & 0 & 0 \\ 0 & 0 & 0 & -\tilde{\Gamma}^{1/2} \\ 0 & 0 & 0 & 0 \end{matrix} & \tilde{\epsilon}_c \mathbf{1}_{4x4} & 0 & \begin{matrix} 0 & 0 & 0 & 0 \\ 0 & 0 & 0 & 0 \\ -\tilde{\Gamma}^{1/2} & 0 & 0 & 0 \\ 0 & -\tilde{\Gamma}^{1/2} & 0 & 0 \end{matrix} \\ \begin{matrix} 0 & 0 & \tilde{\Gamma}^{1/2} & 0 \\ 0 & 0 & 0 & \tilde{\Gamma}^{1/2} \\ 0 & 0 & 0 & 0 \\ 0 & 0 & 0 & 0 \end{matrix} & 0 & \tilde{\epsilon}_c \mathbf{1}_{4x4} & \begin{matrix} 0 & 0 & 0 & 0 \\ \tilde{\Gamma}^{1/2} & 0 & 0 & 0 \\ 0 & 0 & 0 & 0 \\ 0 & 0 & -\tilde{\Gamma}^{1/2} & 0 \end{matrix} \\ 0 & \begin{matrix} 0 & 0 & -\tilde{\Gamma}^{1/2} & 0 \\ 0 & 0 & 0 & -\tilde{\Gamma}^{1/2} \\ 0 & 0 & 0 & 0 \\ 0 & 0 & 0 & 0 \end{matrix} & \begin{matrix} 0 & \tilde{\Gamma}^{1/2} & 0 & 0 \\ 0 & 0 & 0 & 0 \\ 0 & 0 & 0 & -\tilde{\Gamma}^{1/2} \\ 0 & 0 & 0 & 0 \end{matrix} & \begin{matrix} \left(2\tilde{\epsilon}_c + \tilde{U}_c\right) \cdot \\ \mathbf{1}_{4x4} \end{matrix} \end{array} \right)$$

Here $\tilde{\epsilon}_c$, $\tilde{U}_c$ and $\tilde{\Gamma}$ are given by Eq. (5.13). We see that the starting point Hamiltonian (5.19) has the same block structure which was already mentioned in Section 4.3. As before we will enumerate them from 1 to 4, where the block at the upper left corner is 1 and the block at the lower right corner is 4.

To determine the absorption spectrum, cf. Eq. (3.12), we need to calculate the matrix elements and the δ-functions. The perturbation $\mathcal{H}'$ can be set up as a matrix analogously to the unperturbed Hamiltonian (5.19), using the same basis. After as many iterations have passed as needed for a certain desired resolution, the matrix elements of $\mathcal{H}'$ can be computed. Besides the matrix elements, we also need to compute the functions $\delta\left(E_f - E_i + \hbar\omega\right)$. The energies E_f and E_i are computed by the NRG process, but we are facing a problem of principle of how to treat the δ-function numerically. Eq. (3.12) would just yield a continuous function for an infinite sum, which naturally cannot be obtained numerically. Thus a procedure is used which is called the 'broadening' of δ-functions, where the δ-functions are approximated by other distributions with finite width, as e. g. Gaussians, which leads to a continuous function for a finite sum. In fact, the procedure contains some elaborate details, which can be found in [20].

One main obstacle had to be overcome to successfully apply the NRG method to the extended model. Since the NRG was designed to resolve the ground state, it computes the properties of excited states with less accuracy. The reason for this lies in the logarithmic discretization of the conduction band. The discretization has the finest resolution around the Fermi energy. With increasing energy, each discretized state represents larger and larger energy intervals. Therefore physical quantities depending on the properties of highly excited states are computed qualitatively rather than quantitatively by the NRG. At first sight, the absorption spectrum looks like such a quantity. It depends on matrix elements involving transitions from the ground state, which contains no holes, to states containing one hole, which are highly excited, i. e. which have energies $E \gg \epsilon_F$. In terms of the block structure which was mentioned above, we would like to compute a quantity involving transitions from block 4 ($\mathcal{H}_{|\uparrow\downarrow\rangle_v}$) to block 2 ($\mathcal{H}_{|\uparrow\rangle_v}$) or 3 ($\mathcal{H}_{|\downarrow\rangle_v}$), respectively. One solution to the problem would be to employ two usual NRG procedures. The first solves the Hamiltonian $\mathcal{H}_{|\uparrow\downarrow\rangle_v}$ and the second one the Hamiltonian $\mathcal{H}_{|\downarrow\rangle_v}$, where the ground states of both $\mathcal{H}_{|\uparrow\downarrow\rangle_v}$ and $\mathcal{H}_{|\downarrow\rangle_v}$) would be resolved with a high precision. Since no magnetic fields are considered, $\mathcal{H}_{|\uparrow\rangle_v}$ equals $\mathcal{H}_{|\downarrow\rangle_v}$ and does not have to be considered separately. In principle, the matrix elements could the be determined, but there is one severe difficulty. As the unitary transformations diagonalizing the Hamiltonian $\mathcal{H}_N$ at each iteration will be different for the two NRG procedures, the final states will be computed in two different basises. To overcome this problem, one would need to keep track of all the unitary transformations of all iterations and to convert one of the results to the other basis, which is a quite tedious and lengthy task. Thus we chose a slightly different method. By modifying the procedure of truncation, we essentially carry out the two NRG procedures, which have just been described, at the same time. Instead of keeping the K lowest lying states, the used procedure keeps $K/2$ of the lowest lying states of each block 4 ($\mathcal{H}_{|\uparrow\downarrow\rangle_v}$) and block 3 ($\mathcal{H}_{|\downarrow\rangle_v}$). Thereby the ground states of $\mathcal{H}_{|\uparrow\downarrow\rangle_v}$ and $\mathcal{H}_{|\downarrow\rangle_v}$ are resolved with a high precision, which produces the same results as making two runs.

Since significant changes have been made in the NRG process, one has to check that the method is still working. One possibility to examine the results so produced is to compare them with established results or analytical calculations which can be done for limiting cases. For the limiting case $U_{exc} = 0$ we have shown, see Section 3.3, that the absorption spectrum is proportional to the local density of states, which can be calculated with the usual NRG method. We will find a cut-off energy for the absorption function. Photons with energies below this cut-off will not be absorbed. For energies close to the cut-off, the absorption function has a power-law divergence, and it is possible to calculate the corresponding exponent analytically, which yields another test for the numerical calculations. The modified method has passed several of these tests, as will be shown in Chapter 6.

Chapter 6

Results

In this chapter the results will be presented that have been produced with the modified NRG procedure introduced in Chapter 5.

In Section 6.1, it will be demonstrated that the numerical method passes several checks. Firstly, we will look at the density of states of the local conduction band level, where the Kondo resonance should be visible in the Kondo regime. Secondly, the height of the resonance has to fulfill the Friedel sum rule, which will be shown to be the case. Thirdly, the relation between the local density of states function and the absorption spectrum will be checked, which was derived in Section 3.3 for the limiting case $U_{\text{exc}} = 0$. Furthermore it will be shown that the density of states of the local conduction band level does not depend on U_{exc}. Thus Section 6.1 deals with cases where the local valence band level is either decoupled, $U_{\text{exc}} = 0$, or of no importance at all. Therefore we essentially only study the properties of the local conduction band coupled to the lead. In this situation it is rather easy to interpret the results, which in principle could be produced with the usual NRG method. We will turn to the more interesting case $U_{\text{exc}} \neq 0$ in Section 6.2. It will be shown that if U_{exc} is gradually increased, the absorption function yields two interesting features. The first one is a shift of the threshold energy, below which no photons are absorbed. In general the threshold energy decreases if U_{exc} is increased. However, depending on the parameters there is a certain interval of U_{exc} where the threshold energy increases with increasing U_{exc}. This behavior can be understood by looking closer at the involved charging energies. Secondly, there is a tremendous increase in height of about three orders of magnitude, which results from the fact that the absorption function becomes divergent at the threshold energy. The exponent of the divergence close to the threshold energy can be calculated analytically, yielding another test for the modified NRG method. We will see that there is a very good agreement between the numerical results and the analytical predictions.

One general remark has to be made about the choice of the parameters. As already mentioned in Chapter 5, it is convenient to measure all parameters in units of bandwidth. In Chapter 4 an explanation was given that the physics and thus the obtained results of two systems with different sets of parameters will be the same, as long as the parameters in each set have the same relation to each other and as long as the modulus of all parameters is $\lesssim 1$ in units of the bandwidth. This argument only holds for the parameters ϵ_c, U_c and V_c, since only the local conduction band level is coupled to a band and thus only the parameters of the local conduction band level will be renormalized. Therefore we can always choose the parameters ϵ_c, U_c and V_c such that $|\epsilon_c|, |\epsilon_c+U_c|, |V_c|$ are smaller or about the order of the bandwidth. However, since the local valence band is not coupled to a band, the parameters ϵ_v and U_v are not subject to renormalization. They are only involved indirectly by the coupling of the local conduction band level and the local valence band level via the exciton binding energy. As we have seen in Section 4.3, the effect of a hole in the local valence band level is to 'pull down' the local conduction band level and that in fact the energy $\tilde{\epsilon}_c \equiv \sum_\sigma (\epsilon_c - U_{\text{exc}} \sum_\nu (1 - n_{v,\nu}))$ is renormalized.

However, for the choice of the parameter ϵ_v we are facing a numerical problem. As already mentioned several times, the bandgap is the largest energy scale involved. Therefore the energy of the local valence band level ϵ_v, measured from the Fermi level of the conduction band which we set equal to zero, $\epsilon_F = 0$, is about three orders of magnitude larger than the other parameters. This poses a problem for the numerical calculations, which arises from the fact that all eigenenergies in the NRG process are stored with the same limited number of digits. Thus one looses precision if one has energies which differ by several order of magnitude. We therefore are going to neglect the bandgap to enhance the precision, which does not change the results. In case of the absorption spectrum one just has to bear in mind that the function is shifted by a constant offset, i. e. the bandgap. In general we will thus also set $|\epsilon_v| < 1$. Since we do not want to consider states with two holes, see Chapter 3, we always set the parameter $U_v \gg 1$ to supress these states. However, if the energy of the local valence band level is set below the energy of the local conduction band level, $\epsilon_v < \epsilon_c$, states with two holes are highly excited states anyway, even if the bandgap is neglected. Thus the parameter U_v has very little influence on the system. In fact, for a reasonable choice of parameters, the calculations show that the results vary by less than one percent if U_v is varied between 0 and 10 (regard $U_v > 0$ always). In the following, we will set $U_v = 10$.

For a physical choice of parameters one has to note the following. In the experiments studied in Chapter 2, U_{exc} is of order $U_{\text{exc}} \sim U_c$, see [8]. The parameter ϵ_c is experimentally controllable and can be set to any desired value in the experiments by adjusting the gate voltage, see Chapter 2. The choice $|\epsilon_v| < 1$ is of course unphysical, but as mentioned above one obtains the physical result for the absorption function by shifting it by an appropriate value. As explained above, any positive value of U_v leads to physical results since the choice of U_v does not influence the calculations. For the current generation of experiments, the choice $|\epsilon_c|, |\epsilon_c + U_c|$ about the order of 1, i. e. 'deeplying levels', is not physical. However, as mentioned in Chapter 3, it is possible to build more shallow dots.

6.1 Checking the modified NRG procedure

In the first part of this section we will show that the density of states function of the local conduction band level $A_{c,\sigma}$ fulfills the Friedel sum rule, which will be introduced below.

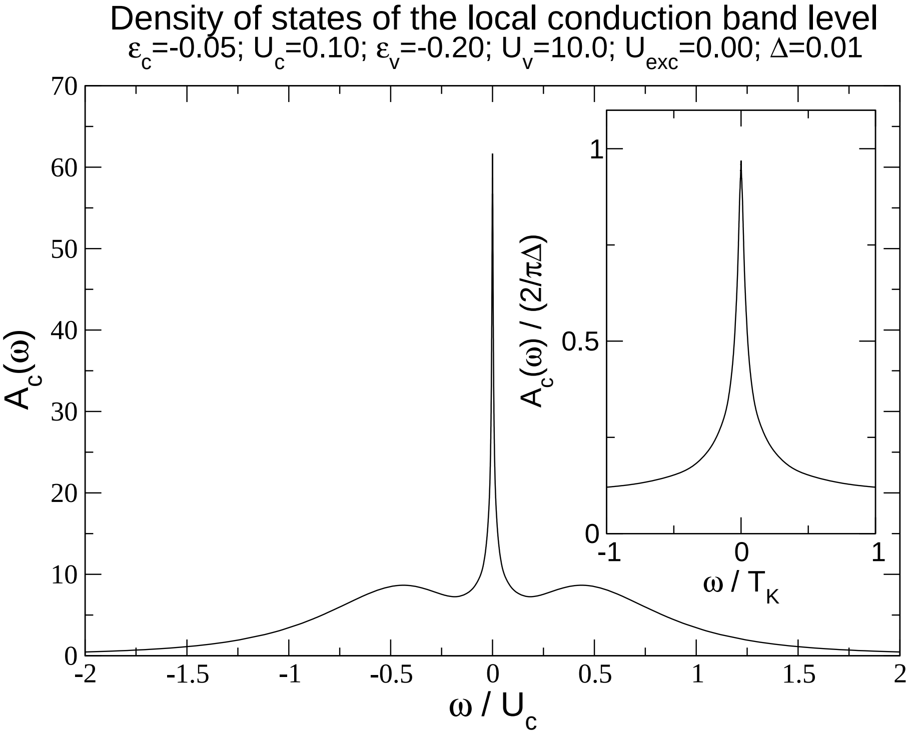

Figure 6.1: The local density of states $A_c(\omega)$ summed over both spin directions in the Kondo regime, with $\epsilon_c = -U_c/2$. The Kondo resonance is at the Fermi energy $\epsilon_F = 0$. The local level at the energy $-U_c/2$ is broadened by the coupling to the lead and has a level width $\Gamma = 2\Delta$. If two electrons are in the dot, the second electron has to pay the charging energy U_c to enter, thus we see another side peak at $U_c/2$, also with level width 2Δ. The inset shows that the Kondo resonance fulfills the Friedel-sum-rule to within 3% accuracy.

In the second part we will demonstrate that the modified method passes the test put forward in Section 3.3, where for the limiting case $U_{\text{exc}} = 0$ a relation between $A_{c,\sigma}$ and the absorption function was derived.

The density of states $A_{c,\sigma}(\omega)$ of the local conduction band level can be computed with the help of Eq. (3.13), where the matrix elements and the eigenenergies are determined by NRG. The function $A_{c,\sigma}$ does not depend on the parameters U_{exc} and ϵ_v, since only states with no holes, i. e. states of block 4 in terms of the block structure, are involved in Eq. (3.13): The ground state $|0\rangle$ does not contain holes and as only transitions mediated by the operator $c_\sigma^\dagger$ are considered, the states $|n\rangle$ do not contain any holes, either. If we study a system with the set of parameters $\epsilon_c = -0.05$, $U_c = 0.10$ and $\Delta \equiv \pi\rho_0|V_c|^2 = 0.01$, then we expect to find the Kondo resonance, as the local level will be singly occupied, see Section 3.1. This is indeed the case, see Fig. 6.1, where the density of states for both spin directions is plotted, $A_c(\omega) = A_{c,\uparrow}(\omega) + A_{c,\downarrow}(\omega)$. We see the Kondo resonance at the Fermi energy $\epsilon_F = 0$ and the side peaks of the singly and doubly occupied local level with width

$\Gamma = 2\Delta \propto |V_c|^2$ at the energies $\pm U_c/2$. From the Friedel sum rule, the height of the Kondo resonance should fulfill the relation

$$A_c(\epsilon_F = 0) = 2\frac{\sin^2(\pi\langle n_c\rangle)}{\pi\Delta} \tag{6.1}$$

where $\langle n_c\rangle$ is the average occupation of the local conduction band level. See [2] for a derivation. The case $\epsilon_c = -U_c/2$ is called 'symmetric', where one knows that the occupation of the local conduction band level is exactly one, which agrees with the occupation determined with NRG. Thus Eq. (6.1) can be written as $A_c(\epsilon_F = 0) = 2/\pi\Delta$, which is shown to be the case to within 3% accuracy in the inset of Fig. 6.1. There we also see that the Kondo resonance has a width of roughly $2T_K$, where T_K is given by Eq. (4.30). Since the occupation of the local level is one, the integral of the density of states function from minus infinity until zero should be one, and since the local level can be occupied by maximally two electrons, the integral from minus infinity until infinity should be two. These results are found with an accuracy of one percent, if $A_c(\omega)$ is numerically integrated.

Let us now look at the absorption spectrum,

$$\alpha(\omega) \equiv \frac{W_{i\to f}}{|\gamma|^2} = 2\pi \sum_f \frac{\left|H'_{fi}\right|^2}{|\gamma|^2}\delta\left(E_f - E_i + \omega\right), \tag{6.2}$$

cf. Eq. (3.12), where we have set $\hbar = 1$. As mentioned in Chapter 3, the height of the absorption spectrum is proportional to $|\gamma|^2$, because $|H'_{fi}|^2 \propto |\gamma|^2$. Since the value of γ depends on the laser intensity in the absorption measurements, we devide by $|\gamma|^2$ to make our results independent of the actual value of γ. For the same set of parameters as in Fig. 6.1, we get the result shown in Fig. 6.2. The absorption spectrum is plotted along negative energies. We see that no photons are absorbed below a threshold energy ω_0, where $\omega_0 = \epsilon_v$ in the case $U_{\text{exc}} = 0$. As mentioned above, here the bandgap has been neglected, which should actually be subtracted from ϵ_v, i. e. be added to the threshold energy ω_0. If we compare Fig. 6.1 with Fig. 6.2, we see, that it is the mirrored positive energy half of the density of states of function, shifted by ϵ_v, which we expected, cf. Eq. (3.18).

One could object that it is not a rigorous test to compare Fig. 6.2 with Fig. 6.1, since both results have been received with the modified NRG method and that Fig. 6.2 should be compared with a result produced with the usual NRG method. This has been done in Fig. 6.3, where the local density of states has been calculated with the usual NRG method for a single level coupled to a conduction band. For the local level and the coupling to the lead the same parameters as above were chosen, $\epsilon_c = -0.05$, $U_c = 0.10$ and $\Delta = 0.01$. Of course, the parameters U_{exc}, ϵ_v and U_v do not occur in this calculation. In Fig. 6.3, just the mirrored positive half of the local density of states has been plotted, shifted by ϵ_v. We see that there is an excellent agreement between the result produced with the usual NRG method and the absorption spectrum calculated with the modified NRG, where the same parameters were taken as in Fig. 6.1. The local density of states function calculated with the usual NRG method is a well established result. It has first been calculated in [19], and

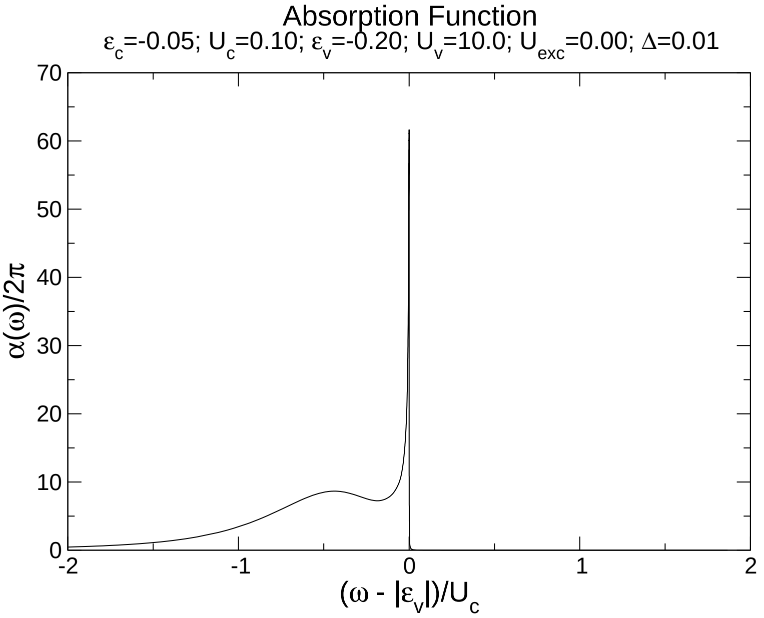

Figure 6.2: Absorption function for the case of a decoupled local valence band level, i. e. $U_{\text{exc}} = 0$. We see that it is the mirrored positive energy half of the density of states of function of the local conduction band level, shifted by $|\epsilon_v|$, cf. Eq. (3.18).

confirmed many times. Thus we can regard the comparison in Fig. 6.3 as a rigorous test for the modified method.

Having well understood the results produced for $U_{\text{exc}} = 0$, i. e. a decoupled local valence band level, we turn to the case $U_{\text{exc}} \neq 0$ in the next section.

6.2 Results

The local valence band level interacts with its enviroment only via the exciton binding energy with coupling strength $\propto U_{\text{exc}}$. The case $U_{\text{exc}} = 0$, where the local valence band level is completely decoupled, was studied in the previous section.

Let us explore how the absorption spectrum changes if U_{exc} is increased. In Fig. 6.4, the absorption spectrum is plotted for the parameters $\epsilon_c = -0.05$, $U_c = 0.10$, $\epsilon_v = -0.5$ and $\Delta = 0.01$, where U_{exc} is increased from 0.00 to 0.14. For this set of parameters, the quantum dot is in the Kondo state before absorption. Using the modified NRG method, it is possible to calculate the absorption spectrum for an arbitrary choice of parameters, including initial states which are not strong correlated Kondo states. In fact, in the second part of this section, where the height of the absorption spectrum is investigated, see below, we study results gained for a variety of different choices of parameters. However, we are especially interested in the case where the initial state is the Kondo state. In this regime, NRG is the only known method which can be used to obtain the produced results. Thus

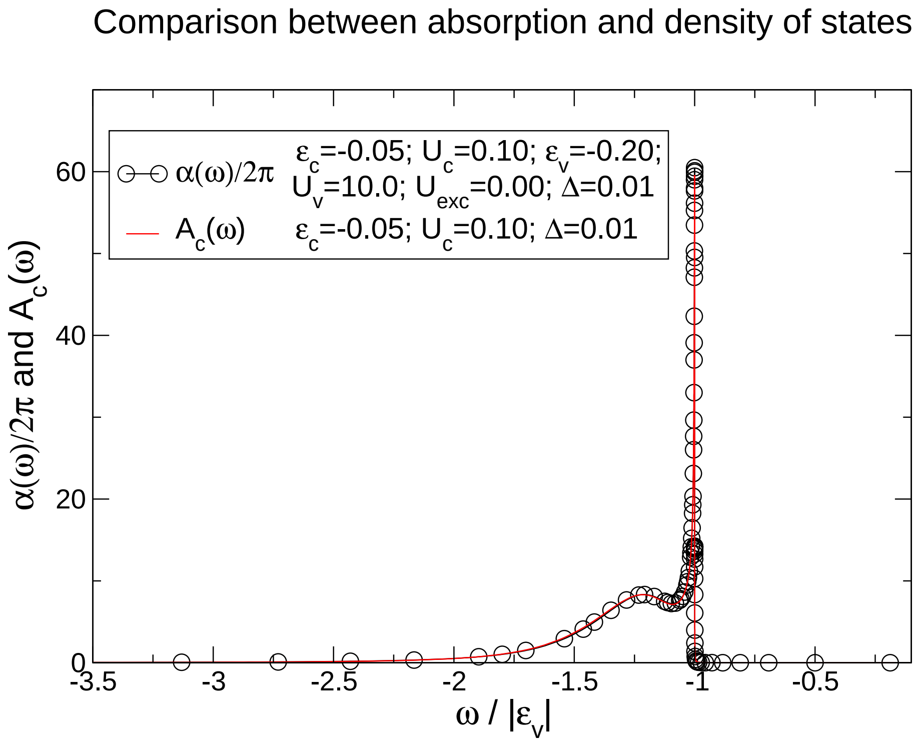

Figure 6.3: Comparison between the absorption spectrum, calculated with the modified NRG method, and the local density of states of a single level, calculated with the usual NRG method. Only the positive energy half of the local density of states is shown, mirrored and shifted by ϵ_v. The numerical results show an excellent agreement between the two functions which, according to Eq. (3.18), should be the same.

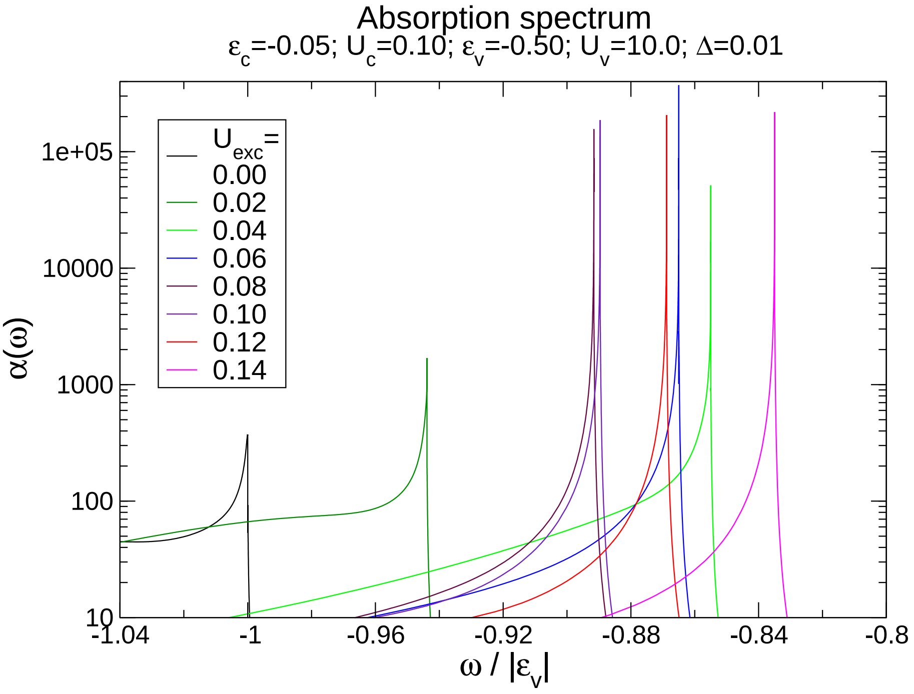

Figure 6.4: Absorption spectra for gradually increasing U_{exc}. The threshold energy is first shifted to the right, until $U_{\text{exc}} = 0.04$ (light green) is reached, then it is shifted back to the left until $U_{\text{exc}} = 0.08$ (brown), and finally moves to the right again. There is also a tremendous increase in height: the maximum of the absorption spectrum for $U_{\text{exc}} = 0.06$ (blue) is about three orders of magnitude larger than the maximum for $U_{\text{exc}} = 0.00$ (black).

we consider fig. 6.4 as our main result.

Before we look at the absorption spectrum more closely, one last remark is made concerning the choice of parameters. For a physical choice of U_{exc}, we have $U_{\text{exc}} \sim U_c$. In this case the Kondo state is destroyed by the absorption. To see why, note that the average occupation of the local conduction band level of the final state increases as U_{exc} increases, as will be explained below. For $U_{\text{exc}} \gtrsim 0.05$, the average occupation is $\gtrsim 1.5$, thus the final state has been shifted out of the Kondo regime.

We notice two relevant behaviors of the absorption spectrum as U_{exc} is increased. Firstly, the modulus of the threshold energy $|\omega_0|$ first decreases, then increases and finally decreases again. We will give an explanation for this behavior and show what is happening at the turning points. Secondly, there is a tremendous increase in height of the absorption spectrum (note that a logarithmic scale is used!). The increase in height is due to the fact that the absorption spectrum diverges at the threshold energy ω_0, as will be explained below.

To understand the shift of the threshold energy ω_0, let us look at the absorption process again, Fig. 6.5. The final state has one hole, therefore one gains the energy U_{exc} for every

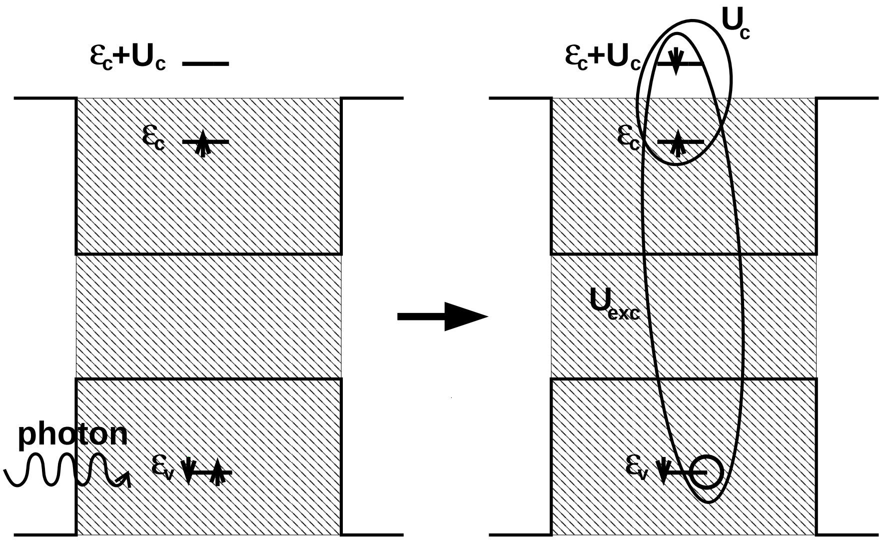

Figure 6.5: The absorption process in the quantum dot. Since in the final there is one hole, the energy U_{exc} is gained for every electron in the local conduction band level. Thus it becomes more favorable to doubly occupy the local conduction band level. However, if the average occupation is larger than one, the exciton binding energy competes with the Coulomb repulsion with strength U_c.

electron in the local conduction band level. Thus, for the final state, the Coulomb repulsion energy with strength U_c and the exciton binding energy with strength U_{exc} are competing against each other as soon as the occupation becomes larger than one. For increasing U_{exc}, one can predict the occupation of the local conduction band level quite well if one thinks in terms of Section 4.3. There the extended Anderson model is transformed to the Anderson model, where the local conduction band level is 'pulled down' by U_{exc} if one hole is present. Thus one can predict that a second electron starts to enter the dot, i. e. the average occupation starts to become larger than one, as soon as $\epsilon_c - U_{\text{exc}} + U_c \sim \Delta$, where $\Gamma = 2\Delta$ is the level width. If U_{exc} is increased further, the occupation will reach a value close to two if $\epsilon_c - U_{\text{exc}} + U_c \sim -\Delta$. We now roughly estimate the energy of the dot before and after absorption. We neglect the lead, except for considering the average occupation of the local conduction band level. The dot in the initial and final state has the energy

$$\begin{aligned} E_{\text{initial}} &= 2\epsilon_v + \epsilon_c \langle n_c \rangle_{\text{initial}} + U_c \Theta\left(\langle n_c \rangle_{\text{initial}} - 1\right)\left(\langle n_c \rangle_{\text{initial}} - 1\right), \\ E_{\text{final}} &= \epsilon_v + \epsilon_c \langle n_c \rangle_{\text{final}} + U_c \Theta\left(\langle n_c \rangle_{\text{final}} - 1\right)\left(\langle n_c \rangle_{\text{final}} - 1\right) - U_{\text{exc}} \langle n_c \rangle_{\text{final}}. \end{aligned} \tag{6.3}$$

To get a rough estimate for the threshold energy ω_0, we calculate the energy difference between the dot in the initial and final state,

$$\begin{aligned} \omega_0 &\approx E_{\text{initial}} - E_{\text{final}} \\ &= \epsilon_v + \epsilon_c \left(\langle n_c \rangle_{\text{initial}} - \langle n_c \rangle_{\text{final}}\right) + U_{\text{exc}} \langle n_c \rangle_{\text{final}} \\ &\quad + U_c \left[\Theta\left(\langle n_c \rangle_{\text{initial}} - 1\right)\left(\langle n_c \rangle_{\text{initial}} - 1\right) - \Theta\left(\langle n_c \rangle_{\text{final}} - 1\right)\left(\langle n_c \rangle_{\text{final}} - 1\right)\right]. \end{aligned} \tag{6.4}$$

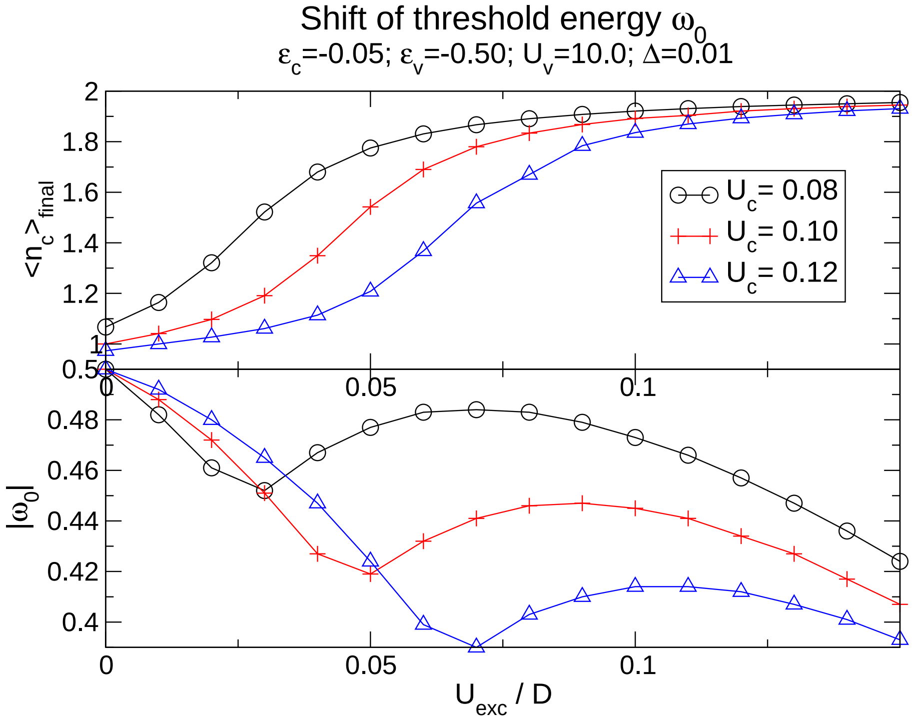

Figure 6.6: Behaviour of the threshold energy for different values of U_c. In the lower panel the moduls of the threshold energy $|\omega_0|$, which has been determined with NRG, has been plotted versus U_{exc}. The upper panel shows the average occupation of the local conduction band level in the final state, i. e. in the state with one hole. For explanations see text.

To extract the meaning of the formula, we simplify it by assuming that the parameters are chosen such that the average occupation of the initial state is one, $\langle n_c \rangle_{\text{initial}} = 1$. Thus also $\langle n_c \rangle_{\text{final}} \geq 1$. Then

$$\omega_0 \approx \epsilon_v - \epsilon_c \left(\langle n_c \rangle_{\text{final}} - 1 \right) + U_{\text{exc}} \langle n_c \rangle_{\text{final}} - U_c \left(\langle n_c \rangle_{\text{final}} - 1 \right) . \tag{6.5}$$

We see that the two last terms compete against each other. As U_{exc} is increased, initially $\langle n_c \rangle_{\text{final}} \approx 1$ remains constant, until $\epsilon_c - U_{\text{exc}} + U_c \sim \Delta$. Thus the modulus of the threshold, $|\omega_0|$, decreases linearly with U_{exc}. If U_{exc} is increased further, such that $\epsilon_c - U_{\text{exc}} + U_c$ drops below Δ, the average occupation will go roughly from one to two. At $\epsilon_c - U_{\text{exc}} + U_c \sim \Delta$, U_{exc} is significantly smaller than U_c, therefore the U_c-term in Eq. (6.5) dominates as $\langle n_c \rangle_{\text{final}}$ increases, causing $|\omega_0|$ to increase again. Finally, when $\langle n_c \rangle_{\text{final}}$ reaches a value close to two, the U_c-term will become constant, and the U_{exc} will dominate again, thus $|\omega_0|$ decreases again.

This explanation is confirmed by the results shown in Fig. 6.6 and Fig. 6.7, where the threshold energy is plotted versus increasing U_{exc}. In Fig. 6.6, the behavior of the threshold energy has been plotted for three different values of U_c, 0.08, 0.10 and 0.12. For increasing U_c, the point $\epsilon_c - U_{\text{exc}} + U_c \sim \Delta$, where the second electron starts to enter the

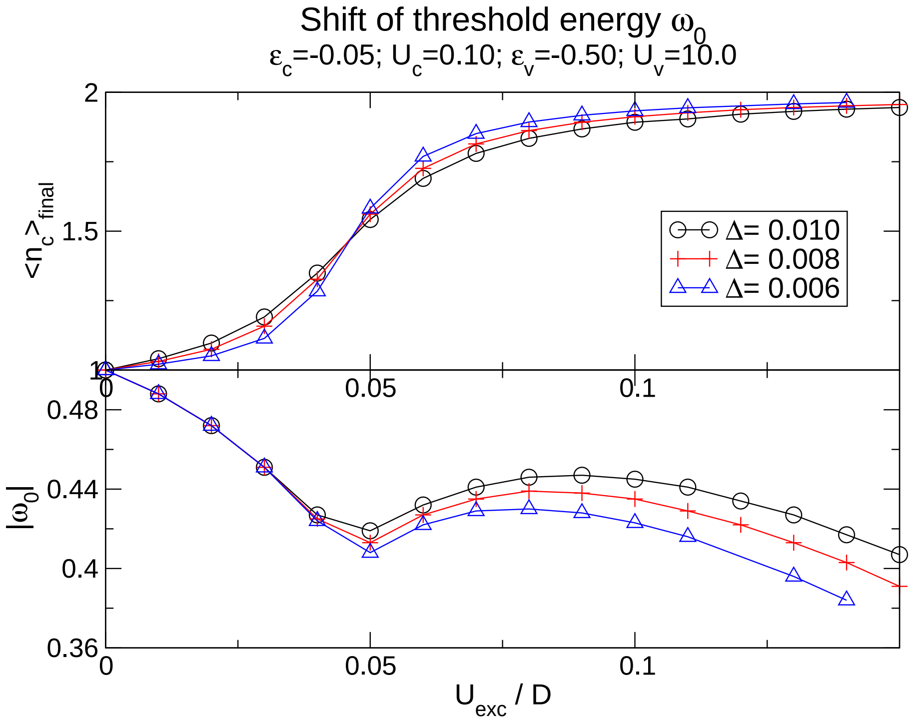

Figure 6.7: Behaviour of the threshold energy for different values of Δ, cf. Fig. 6.6. For explanations see text.

dot, is reached for higher values of U_{exc}. Since the U_c-term in Eq. (6.5) starts to dominate for higher values of U_{exc}, the first turning point is shifted to the right, which is reached at values of the average occupation about $\langle n_c \rangle_{\text{final}} \sim 1.5$. Furthermore the second turning point is also shifted to the right, as $\langle n_c \rangle_{\text{final}} \sim 2$ is reached for higher values of U_{exc}.

In Fig. 6.7, the parameter $U_c = 0.10$ is kept fixed and Δ is varied instead. We see that the first turning point stays constant at $U_{\text{exc}} = 0.05$, since there $\langle n_c \rangle_{\text{final}} \sim 1.5$ is reached. However, the value $|\omega_0|$ at the first turning point decreases as Δ decreases, since the occupation starts to change at larger values of U_{exc}. As $\langle n_c \rangle_{\text{final}} \sim 2$ is reached at smaller values of U_{exc} as Δ decreases, the second turning point is shifted to the left.

Let us now study the height of the absorption spectrum. For energies ω near the threshold energy ω_0 we find a power-law divergence,

$$\alpha(\omega) \sim \left(\frac{1}{|\omega - \omega_0|} \right)^{\beta}, \ \ \omega \sim \omega_0. \tag{6.6}$$

This result is also found in [21], where the absorption spectrum is studied for the X-ray edge problem. There, only a local valence band level is considered which can either be empty or singly occupied, where the empty local level is considered as a hole. The local level interacts with the conduction band only via potential scattering if it is empty, due to the Coulomb attraction of the hole. In the absorption process, the electron from the local valence band level is excited directly into the conduction band. It is shown in [21] that the exponent β is given by

$$\beta = 1 - \sum_{\sigma} N_{\sigma}^2, \tag{6.7}$$

where N_σ is the 'effective number of electrons' (not necessarily an integer), with spin σ, which flow away from the local level in the absorption process. There are more contributions to N_σ than just the electron which is excited from the localized level into the conduction band. After the electron is excited out of the local level, there is a hole left. The potential of the hole will be screened by a change in the charge density of the conduction band, whereby a certain amount of negative charge, say n_σ^{screen}, is drawn towards the local level. This amount has to be subtracted, as it is charge flowing towards the local level. Thus, if an electron with spin σ, say, is excited, $N_\sigma = 1 - n_\sigma^{\text{screen}}$ and $N_{-\sigma} - n_\sigma^{\text{screen}}$. For Fermi liquids, n_σ^{screen} can be determined from the Friedel sum rule, which relates it to the change in scattering phase shift.

We can use the result (6.7) to analyze our case, too, because at $T = 0$, which we are considering, the system is always in a Fermi liquid ground state, so that arguments based on the relation between phase shifts and screening charges do apply. In the absorption process which we are considering, the electron is excited from the local valence band level to the local conduction band level. In our model, there is hybridization between the local conduction band level and the conduction band. In the following argument, we thus consider the local conduction band level and the conduction band to be a single entity, and the local valence band level to correspond to the local level considered in [21]. To determine N_σ, we have to sum up the charges with spin σ, which flow away from the local valence band level in the absorption process. The actual sign of N_σ does not matter, since (6.7) depends on N_σ^2. For definiteness, we shall take N_σ to be positive if a all in all positive electron number, i. e. negative charge, flows away from the local level. In the absorption process, an electron with spin σ, say, is excited from the local valence band level into the local conduction band level. However, the electron hops immediately into the conduction band and hence flows away from the local valence band level, thus making a contribution +1 to N_σ and 0 to $N_{-\sigma}$. As to n_σ^{screen}, its value is determined by the value of U_{exc}, which pulls down the local conduction band level, causing its charge to change by $\Delta n \equiv \langle n_c \rangle_{\text{final}} - \langle n_c \rangle_{\text{initial}}$. This charge Δn screens the Coulomb attraction of the hole in the local valence band level. Since the charge Δn, i. e. $\Delta n/2$ per spin direction, is brought towards the local valence band level, we have to take $n_\sigma^{\text{screen}} = \Delta n/2$, implying $N_\sigma = 1 - \Delta n/2$ and $N_{-\sigma} = -\Delta n/2$. Therefore, in our case, Eq. (6.7) can be written as

$$\beta = \Delta n - \frac{(\Delta n)^2}{2}. \tag{6.8}$$

A similar argument has been used in [22], [23], where the local spectral function of the Anderson was studied.

We have extracted the exponent of the absorption spectrum in the limit $\omega \to \omega_0$ from our numerical NRG results. To check this formula, we have varied Δn in two independent ways, namely by varying the value of ϵ_c between -0.05 and 0.05 in steps of 0.02, and by varying the value of U_{exc} between 0.00 and 0.10 in steps of 0.01. The other parameters are constant, $\epsilon_v = -0.20$, $U_c = 0.10$ and $\Delta = 0.030$ or $\Delta = 0.015$ for the cases $\epsilon_c = -0.01, 0.01$ or $\epsilon_c = -0.05, -0.03, 0.03, 0.05$, respectively. For one choice of parameters, the mirrored absorption spectra, shifted by $|\omega_0|$, are shown in Fig. 6.8. We find the power law behavior for energies $|\omega - \omega_0| < 10^{-4}D$. The number of iterations of the NRG process sets a lower bound for $|\omega - \omega_0|$. For energies below this lower bound, the absorption spectrum is not calculated accurately, see Chapter 5. The number of NRG iterations for the result shown in Fig. 6.8 is 50, which gives a lower bound of $\omega - \omega_0| \approx 10^{-6}D$.

The results are shown in Fig. 6.9. We see that the numerical results agree well with the prediction (6.8): all data points collapse onto a single curve, given by (6.8). Note that Eq. (6.8) holds for arbitrary values of ϵ_c, including initial states that lie either in the Kondo or the non-Kondo regime. We see that for $\Delta n = 0$, which corresponds to $U_{\text{exc}} = 0$, the exponent is zero. With increasing height, the exponent also increases and the absorption function thus diverges at the threshold energy ω_0, which explains the dramatic increase in peak heights in Fig. 6.4.

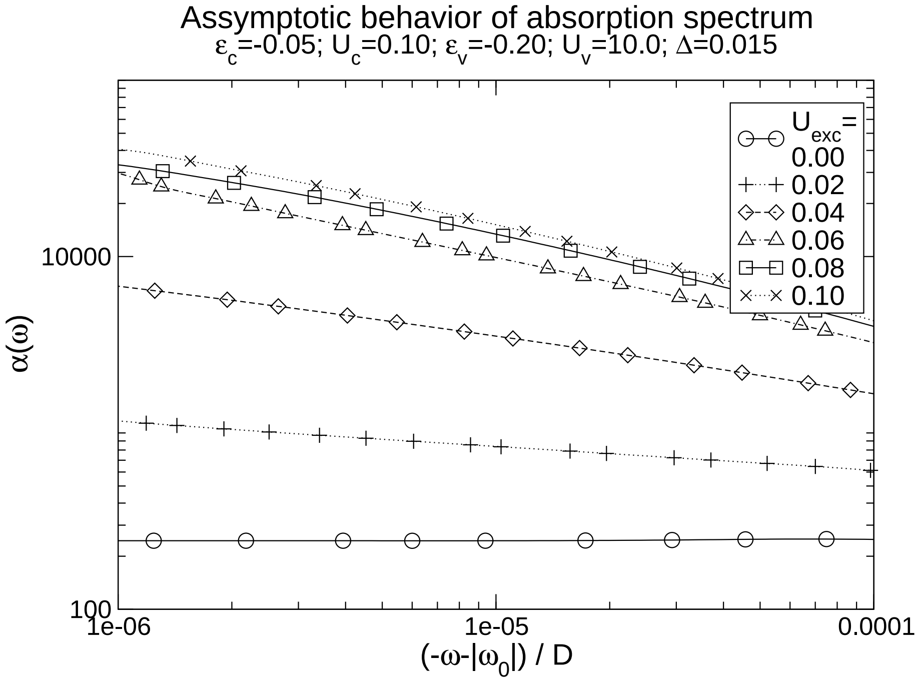

Figure 6.8: Mirrored absorption spectra shifted by the threshold energy ω_0. For energies $|\omega - \omega_0| < 10^{-4}D$, we find the power-law behavior predicted by Eq. (6.6). Since the functions have been mirrored, a negative slope corresponds to a positive Exponent. We see that the exponent increases as U_{exc} increases.

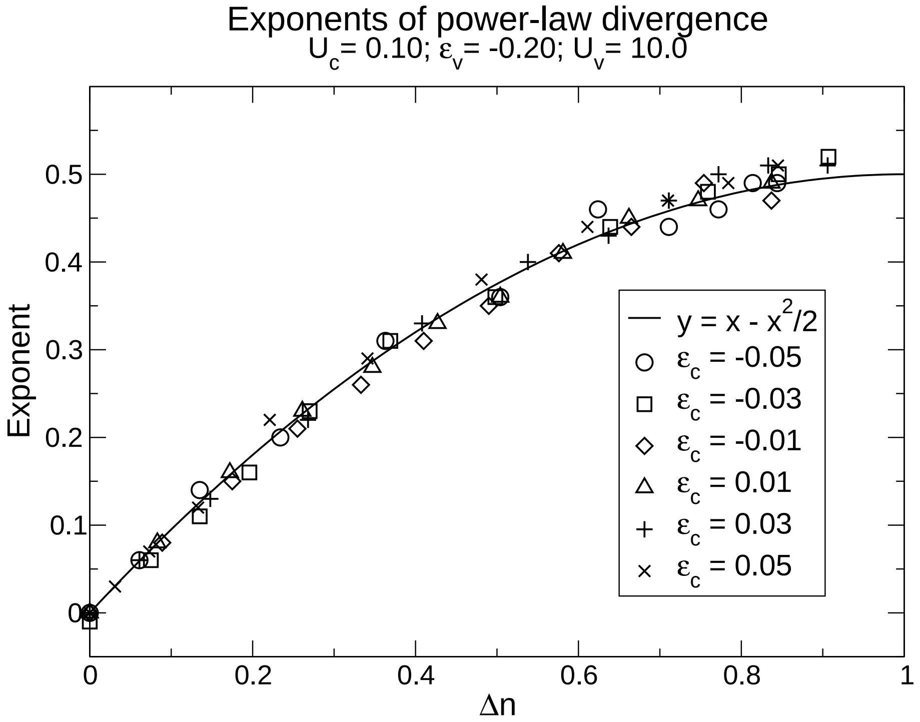

Figure 6.9: The exponent of the power-law divergence, see Eq. (6.6), extracted from the numerical NRG results, cf. Fig. 6.8, for different values of ϵ_c and U_{exc}, where U_{exc} is varied between 0.00 and 0.10 in steps of 0.01 for each value of ϵ_c.

Chapter 7

Conclusions

The aim of this thesis was to calculate the absorption spectrum of a quantum dot in the Kondo ground-state. Motivated by experimental results [6], a model was set up describing InAs quantum dots in a GaAs semiconductor, see Chapter 3.

The Poor Man's Scaling method was used to study the model qualitatively in Chapter 4. It was shown that the model can be transformed to the Anderson model, whereby the exciton binding energy is absorbed by redefining the energy of the local level, which is 'pulled down' by the exciton binding energy. We determined the Kondo temperature for the model, which depends on the exciton binding energy.

By modifying the numerical renormalization method (NRG), we solved the model in a numerically exact manner and calculated the absorption spectrum, see Chapter 5.

The academic limiting case of a vanishing exciton binding energy was studied and well understood, see Chapters 3 and 6. In Chapter 3, it was shown that in this limiting case it is possible to find a relation between the absorption spectrum and the density of states function of the local level in the quantum dot. This result was used in Chapter 6 to check whether the modified NRG method is working correctly.

Finally, we used the modified NRG method to calculate our main result, Fig. 6.4, the absorption spectrum of a quantum dot in the strongly correlated Kondo ground-state. Starting from the well-understood limiting case of vanishing exciton binding energy, the absorption spectrum was studied for increasing exciton binding energy. Two rather dramatic features are predicted. Firstly, there is a marked shift of the threshold energy, below which no photons are observed. By considering the involved energy scales, we gave an explanation for the behavior of the threshold energy as a function of the exciton binding energy. Secondly, we noticed a tremendous increase in height of the absorption spectrum as the exciton binding energy increases. In fact, the absorption spectrum diverges at the threshold energy. We gave an expression for the exponent of the divergence, which depends on the difference of the average occupation of the local level of the quantum dot before and after absorption.

In principle, experiments measuring the absorption spectrum are feasible and will hopefully be done in the near future. It will be exciting to see if the experimental results agree with our predictions. In the future, it would be interesting to calculate the emission spectrum of the quantum dot, which is easier to measure in experiments than the absorption spectrum.

Appendix A

Further Details

A.1 Local density of States

The local density of states for spin σ at $T = 0$ can be calculated with help of the retarded Green function,

$$A_{c,\sigma}(\omega) = -\frac{1}{\pi}\Im\left(G^R_{c_\sigma,c^\dagger_\sigma}(\omega)\right), \tag{A.1}$$

with

$$G^R_{c_\sigma,c^\dagger_\sigma}(t) = -i\Theta(t)\left\langle\left[c_\sigma(t), c^\dagger_\sigma(0)\right]\right\rangle, \tag{A.2}$$

see, e. g., [24]. Here $\hbar = 1$ and $\langle\rangle$ denotes an thermal average which reduces to $\langle 0|\ |0\rangle$ for $T = 0$, where $|0\rangle$ is the ground state. To obtain the result 3.13, we first evaluate the Fourier-Transform of eq. (A.2):

$$\begin{aligned}
G^R_{c_\sigma,c^\dagger_\sigma}(\omega) &= \int_{-\infty}^{\infty} G^R_{c_\sigma,c^\dagger_\sigma}(t)e^{i\omega t}dt \\
&= -i\int_0^\infty e^{i\omega t}\left\langle\left[c_\sigma(t), c^\dagger_\sigma(0)\right]_+\right\rangle dt \\
&= -i\sum_n\int_0^\infty e^{i\omega t}\left(\langle 0|e^{iHt}c_\sigma e^{-iHt}|n\rangle\langle n|c^\dagger_\sigma|0\rangle\right. \\
&\quad \left.+\langle 0|c^\dagger_\sigma|n\rangle\langle n|e^{iHt}c_\sigma e^{-iHt}|0\rangle\right)dt \\
&= -i\lim_{\delta\to 0}\sum_n\int_0^\infty e^{-\delta t}e^{i\omega t}\left(e^{iE_0t-iE_nt}\left|\langle n|c^\dagger_\sigma|0\rangle\right|^2\right. \\
&\quad \left.+e^{iE_nt-iE_0t}\left|\langle n|c_\sigma|0\rangle\right|^2\right)dt.
\end{aligned} \tag{A.3}$$

If eq. (A.3) is inserted in eq. (A.1), and if we use $\lim_{\delta\to 0}\frac{1}{\omega+i\delta} = P(1/\omega) - i\pi\delta(\omega)$, we get

$$A_{c,\sigma}(\omega) = \sum_n \left[\left| \langle n | c_\sigma^\dagger | 0 \rangle \right|^2 \delta\left(\omega - (E_n - E_0)\right) + \left| \langle 0 | c_\sigma^\dagger | n \rangle \right|^2 \delta\left(\omega + (E_n - E_0)\right) \right] \tag{A.4}$$

This is eq. (3.13) of Chapter 2.

A.2 Details of Poor Man's Scaling calculation

In this section, lengthy but straightforward derivations of results are presented, which have been used in Chapter 4.

A.2.1 Explicit calculation of a contribution to the effective Hamiltonian

We start with eq. (4.6) of Section 4.1,

$$J_+ J_- \sum_{\vec{q},\vec{k},\vec{q}',\vec{k}'} S^- l^\dagger_{\vec{k}',\uparrow} l_{\vec{q},\downarrow} \frac{1}{E - \mathcal{H}_{\mathrm{lead}}} S^+ l^\dagger_{\vec{q}',\downarrow} l_{\vec{k},\uparrow}. \tag{A.5}$$

Let's rewrite the following exprissions, $\left(E - \mathcal{H}_{\mathrm{lead}}\right)^{-1} l^\dagger_{\vec{q}'}$ and $\left(E - \mathcal{H}_{\mathrm{lead}}\right)^{-1} l_{\vec{k}}$. If we expand the first term, $\left(E - \mathcal{H}_{lead}\right)^{-1} = \left(E - \sum_{\vec{j}} \epsilon_{\vec{j}} l^\dagger_{\vec{j}} l_{\vec{j}}\right)^{-1} = \sum_{i,\vec{j}} c_i \left(\epsilon_{\vec{j}} l^\dagger_{\vec{j}} l_{\vec{j}}\right)^i$, where the coefficiants c_i are unknown, and use $\left[l^\dagger_{\vec{j}} l_{\vec{j}}, l^\dagger_{\vec{q}'}\right]_- = l^\dagger_{\vec{q}'} \delta_{\vec{j},\vec{q}'}$, we receive

$$\begin{aligned} \left(E - \mathcal{H}_{\mathrm{lead}}\right)^{-1} l^\dagger_{\vec{q}'} &= \sum_{i,\vec{j}} c_i \left(\epsilon_{\vec{j}} l^\dagger_{\vec{j}} l_{\vec{j}}\right)^i l^\dagger_{\vec{q}'} = \sum_{i,\vec{j}} c_i \left(\epsilon_{\vec{j}}\right)^i l^\dagger_{\vec{j}} l_{\vec{j}} l^\dagger_{\vec{q}'} \\ &= l^\dagger_{\vec{q}'} \left(\sum_{i,\vec{j}} c_i \left(\epsilon_{\vec{j}} l^\dagger_{\vec{j}} l_{\vec{j}}\right)^i + \sum_i c_i \left(\epsilon_{\vec{q}'}\right)^i \right) = l^\dagger_{\vec{q}'} \left(E - \mathcal{H}_{\mathrm{lead}} - \epsilon_{\vec{q}'}\right)^{-1} \end{aligned} \tag{A.6}$$

and, using $\left[l^\dagger_{\vec{j}} l_{\vec{j}}, l_{\vec{k}}\right]_- = -l_{\vec{k}} \delta_{\vec{j},\vec{k}}$,

$$\left(E - \mathcal{H}_{\mathrm{lead}}\right)^{-1} l_{\vec{k}} = l_{\vec{k}} \left(E - \mathcal{H}_{\mathrm{lead}} + \epsilon_{\vec{k}}\right)^{-1}. \tag{A.7}$$

With the help of eqns. (A.6) and (A.7), we see that eq. (A.5) can be rewritten as

$$J_+ J_- \sum_{\vec{q},\vec{k},\vec{q}',\vec{k}'} S^- S^+ l^\dagger_{\vec{k}',\uparrow} l_{\vec{k},\uparrow} l_{\vec{q},\downarrow} l^\dagger_{\vec{q}',\downarrow} \left(E - H_{lead} - \epsilon_{\vec{q}'} + \epsilon_{\vec{k}}\right)^{-1}, \tag{A.8}$$

which is eq. (4.7) of Section 4.1.

A.2.2 List of contributions (Kondo model)

In this subsection the contributions corresponing to the panels c) to h) of fig. 4.2 to the effective Hamiltonian will be listed. The following contributions result from diagram c),

$$\begin{aligned}
&\sum_{\vec{k},\vec{k}'}\sum_{\vec{q}} J_z S^z l^\dagger_{\vec{k}',\uparrow(\downarrow)} l_{\vec{q},\uparrow(\downarrow)} \left(E-\mathcal{H}_{\text{lead}}\right)^{-1} \sum_{\vec{q}'} J_z S^z l^\dagger_{\vec{q}',\uparrow(\downarrow)} l_{\vec{k},\uparrow(\downarrow)} \\
= \quad &\sum_{\vec{k},\vec{k}'} J_z^2 \rho_0 \delta D S_z^2 l^\dagger_{\vec{k}',\uparrow(\downarrow)} l_{\vec{k},\uparrow(\downarrow)} \left(E-D+\epsilon_{\vec{k}}\right)^{-1},
\end{aligned} \tag{A.9}$$

where the spin up (spin down) term corresponds to the black (red) part. As S_z^2 can be replaced by $S_z^2 = 1/4$, these terms describe potential scattering and can be included in $\mathcal{H}_{\text{lead}}$. This is also true for the terms originating from diagram d),

$$\begin{aligned}
&\sum_{\vec{k},\vec{k}'}\sum_{\vec{q}} J_z S^z l^\dagger_{\vec{q},\uparrow(\downarrow)} l_{\vec{k},\uparrow(\downarrow)} \left(E-\mathcal{H}_{\text{lead}}\right)^{-1} \sum_{\vec{q}'} J_z S^z l^\dagger_{\vec{k}',\uparrow(\downarrow)} l_{\vec{q}',\uparrow(\downarrow)} \\
= \quad &\sum_{\vec{k},\vec{k}'} J_z^2 \rho_0 \delta D S_z^2 \left(\delta_{\vec{k},\vec{k}'} - l^\dagger_{\vec{k}',\uparrow(\downarrow)} l_{\vec{k},\uparrow(\downarrow)}\right) \left(E-D+\epsilon_{\vec{k}}\right)^{-1}.
\end{aligned} \tag{A.10}$$

Here additionally a $\delta_{\vec{k},\vec{k}'}$ term appears by commuting the operators, which represents a constant term that can be incorporated in a redefenition of E, see Section 4.1. The terms corresponding to the black (red) parts of the panels e), f), g) and h) are, using the notation $\sigma = (\uparrow,\downarrow) = (+,-)$,

$$\begin{aligned}
&\mp\sum_{\vec{k},\vec{k}'} J_\pm J_z \sum_{\vec{q}} S^z l^\dagger_{\vec{k}',\mp} l_{\vec{q},\mp} \left(E-\mathcal{H}_{\text{lead}}\right)^{-1} \sum_{\vec{q}'} S^\pm l^\dagger_{\vec{q}',\mp} l_{\vec{k},\pm} \\
&\qquad = -\frac{1}{2} J_\pm J_z \rho_0 \delta D S^\pm l^\dagger_{\vec{k}',\mp} l_{\vec{k},\pm)} \left(E-D+\epsilon_{\vec{k}}\right)^{-1}, \\
&\pm\sum_{\vec{k},\vec{k}'} J_\pm J_z \sum_{\vec{q}} S^z l^\dagger_{\vec{q},\pm} l_{\vec{k},\pm} \left(E-\mathcal{H}_{\text{lead}}\right)^{-1} \sum_{\vec{q}'} S^\pm l^\dagger_{\vec{k}',\mp} l_{\vec{q},\pm} \\
&= \frac{1}{2} J_\pm J_z \rho_0 \delta D S^\pm \left(\delta_{\vec{k},\vec{k}'} - l^\dagger_{\vec{k}',\mp} l_{\vec{k},\pm}\right) \left(E-D-\epsilon_{\vec{k}'}\right)^{-1}, \\
&\mp\sum_{\vec{k},\vec{k}'} J_\pm J_z \sum_{\vec{q}} S^\pm l^\dagger_{\vec{k}',\mp} l_{\vec{q},\pm} \left(E-\mathcal{H}_{\text{lead}}\right)^{-1} \sum_{\vec{q}'} S^z l^\dagger_{\vec{q}',\pm} l_{\vec{k},\pm} \\
&\qquad = -\frac{1}{2} J_\pm J_z \rho_0 \delta D S^\pm l^\dagger_{\vec{k}',\mp} l_{\vec{k},\pm} \left(E-D+\epsilon_{\vec{k}}\right)^{-1}, \\
&\pm\sum_{\vec{k},\vec{k}'} J_\pm J_z \sum_{\vec{q}} S^\pm l^\dagger_{\vec{q},\mp} l_{\vec{k},\pm} \left(E-\mathcal{H}_{\text{lead}}\right)^{-1} \sum_{\vec{q}'} S^z l^\dagger_{\vec{k}',\mp} l_{\vec{q}',\mp} \\
&= +\frac{1}{2} J_\pm J_z \rho_0 \delta D S^\pm \left(\delta_{\vec{k},\vec{k}'} - l^\dagger_{\vec{k}',\mp} l_{\vec{k},\pm}\right) \left(E-D-\epsilon_{\vec{k}'}\right)^{-1},
\end{aligned} \tag{A.11}$$

respectively. Here the relations $S^z S^\pm = \pm S^\pm/2$ and $S^\pm S^z = \mp S^\pm$ were used. These terms can be collected and incorporated into the effective Hamiltonian by renormalizing the parameters $J_\pm$, see eq. (4.13).

A.2.3 List of contributions (Anderson model)

Evaluating the contributions resulting from the panels c) to h), one needs the contractions $X_{2:1,\sigma}X_{1,\sigma:2} = X_{2:2}$, $X_{0:1,\sigma}X_{1,\sigma:0} = X_{0:0}$ and $X_{1,\sigma:2}X_{2:1,\sigma} = X_{1,\sigma:1,\sigma}$. Furthermore one has to make use of $[\mathcal{H}_0, X_{1,\sigma:2}] = -U_c X_{1,\sigma:2}$. We then receive the following contributions resulting from panels c (d), e (f) and g (h),

$$
\begin{aligned}
\sum_{\vec{q},\vec{q}'} V_{\vec{q}} X_{2:1,\downarrow(\uparrow)} l_{\vec{q},\uparrow(\downarrow)} \left(E - \mathcal{H}_0\right)^{-1} V^*_{\vec{q}'} l^\dagger_{\vec{q}',\uparrow(\downarrow)} X_{1,\downarrow(\uparrow):2} &= -\frac{\rho_0 \delta D |V|^2}{D - \epsilon_c - U_c} X_{2:2}, \\
\sum_{\vec{q},\vec{q}'} V^*_{\vec{q}} l^\dagger_{\vec{q},\uparrow(\downarrow)} X_{0:1,\uparrow(\downarrow)} \left(E - \mathcal{H}_0\right)^{-1} V_{\vec{q}'} X_{1,\uparrow(\downarrow):0} l_{\vec{q}',\uparrow(\downarrow)} &= -\frac{\rho_0 \delta D |V|^2}{D + \epsilon_c} X_{0:0}, \\
\sum_{\vec{q},\vec{q}'} V^*_{\vec{q}} l^\dagger_{\vec{q},\uparrow(\downarrow)} X_{1,\downarrow(\uparrow):2} \left(E - \mathcal{H}_0\right)^{-1} V_{\vec{q}'} X_{2:1,\downarrow(\uparrow)} l_{\vec{q}',\uparrow(\downarrow)} &= -\frac{\rho_0 \delta D |V|^2}{D + \epsilon_c + U_c} X_{1,\downarrow(\uparrow):1,\downarrow(\uparrow)} \qquad \text{(A.12)}
\end{aligned}
$$

respectively, where the assumption $V_{\vec{q}} = V$ has been made.

Acknowledgements

Finally, I would like to thank everybody who helped making this thesis possible:

- Prof. Dr. Jan von Delft for giving me the opportunity to join his group at the LMU Munich and for many helpful discussions. I would also like to thank him for his support for several applications and his personal advice.
- A great thanks goes to my supervisors Michael Sindel and László Borda, who were always willing to help, in the true meaning of the word 'always'. However, they are not only good and helpful physicists, but also excellent company to chill out in a bar or restaurant after work.
- The group of Prof. Dr. Khaled Karrai at the LMU Munich for interesting discussions and their helpful experimental view of the work.
- Prof. Dr. Ignacio Cirac from the MPQ in Munich for his official support.
- Everybody else at the Chair for Theoretical Condensed Matter Physics at the LMU in Munich: Markus, Udo, Konstanze, Henryk, Frank, Corinna, Dominique, Robert and Stéphane. They all have been very helpful and also great company during the year. I especially would like to thank my singing roommate Andreas not only for his company but also for proofreading this thesis and giving good advice, which is both quite remarkable for a DMRG guy.
- Prof. Dr. Achim Rosch at the University Cologne for fruitful and helpful discussions, and suggesting to analyze the power law divergencies in our absorption spectra in analogy to the X-ray edge problem.
- Ralph Simmler for keeping the computers running.
- My parents Gerda and Hans-Peter Helmes for their support during the last years.

Bibliography

[1] L. Kouwenhoven and L. Glazman, Revival of the Kondo effect, Physics World (2001).

[2] A. C. Hewson, *The Kondo Problem to Heavy Fermions*, Cambridge University Press, 1993.

[3] P. W. Anderson, A poor man's derivation of scaling laws for the Kondo problem, J. Phys. C **3**, 2436 (1970).

[4] K. G. Wilson, The renormalization group: Critical phenomena and the Kondo problem, Rev. Mod. Phys. **47**, 773 (1975).

[5] L. P. Kouwenhoven and C. M. Marcus, Quantum dots, Physics World (1998).

[6] R. J. Warburton, C. Schäflein, D. Haft, F. Bickel, A. Lorke, K. Karrai, J. M. Garcia, W. Schoenfeld, and P. M. Petroff, Optical emission from a charge-tunable quantum ring, Nature **405**, 926 (2000).

[7] P. W. Anderson, Localized Magnetic States in Metals, Phys. Rev. **124**, 41 (1961).

[8] R. J. Warburton, B. T. Miller, C. S. Dürr, C. Bödefeld, K. Karrai, J. P. Kotthaus, G. Medeiros-Ribeiro, P. M. Petroff, and S. Huant, Coulomb interactions in small charge-tunable quantum dots: A simple model, Phys. Rev. B **58**, 16221 (1998).

[9] D. Birkedal, K. Leosson, and J. M. Hvam, Long Lived Coherence in Self-Assembled Quantum Dots, Phys. Rev. **87**, 227401 (2001).

[10] P. Borri, W. Langbein, S. Schneider, and U. Woggon, Ultralong Dephasing Time in InGaAs Quantum Dots, Phys. Rev. **87**, 157401 (2001).

[11] H. Htoon, D. Kulik, O. Baklenov, A. L. Holmes, T. Takagahara, and C. K. Shih, Carrier relaxation and quantum decoherence of excited states in self-assembled quantum dots, Phys. Rev. B **63**, 241303–1 (2001).

[12] S. Mackowski, T. A. Nguyen, H. E. Jackson, L. M. Smith, J. Kossut, and G. Karczewski, Exciton spin relaxation time in quantum dots measured by continuous-wave photoluminescence spectroscopy, Appl. Phys. Lett. **83**, 5524 (2003).

[13] T. H. Stievater, X. Li, T. Cubel, D. G. Steel, D. Gammon, D. S. Katzer, and D. Park, Measurement of relaxation between polarization eigenstates in single quantum dots, Appl. Phys. Rev. **81**, 4251 (2002).

[14] J. J. Sakurai, *Modern Quantum Mechanics*, Addison-Wesley, revised edition edition, 1995.

[15] A. O. Govorov, K. Karrai, and R. J. Warburton, Kondo excitons in self-assembled quantum dots, Phys. Rev. B. **67**, 241307 (2003).

[16] T. Fujii, A. Furusaki, N. Kawakami, and M. Sigrist, Edge Singularity for the Optically Induced Kondo Effect in a Quantum Dot, cond-mat , 0009320 (2003).

[17] F. D. M. Haldane, Scaling Theory of the Asymmetric Anderson Model, Phys. Rev. **40**, 416 (1978).

[18] H. R. Krishna-murthy, J. W. Wilkins, and K. G. Wilson, Renormalization-group approach to the Anderson model of dilute magnetic alloys, Phys. Rev. B **21**(3), 1003 (1980).

[19] T. A. Costi, A. C. Hewson, and V. Zlatic, Transport coefficients of the Anderson model via the numerical renormalization group, J. Phys. Condens. Matter **6**, 2519 (1994).

[20] R. Bulla, T. A. Costi, and D. Vollhardt, Finite-temperature numerical renormalization group study of the Mott transition, Phys. Rev. B **64**, 045103 (2001).

[21] K. D. Schotte and U. Schotte, Threshold Behavior of the X-Ray Spectra of Light Metals, Phys. Rev. **185**, 509 (1969).

[22] T. A. Costi, P. Schmitteckert, J. Kroha, and P. Wölfle, Numerical Renormalization Group Study of Pseudo-Fermion and Slave-Boson Spectral Functions in the Single Impurity Anderson Model, Phys. Rev. **73**, 1275 (1994).

[23] T. A. Costi, J. Kroha, and P. Wölfle, Spectral properties of the Anderson impurity model: Comparison of numerical-renormalization-group and noncrossing-approximation results, Phys. Rev. B **53**, 1850 (1996).

[24] G. Rickayzen, *Green's Functions and Condensed Matter*, Academic Press, 1980.